Hana Kristin Hampel, BSc.

Investigation of morphology and composition of Laser Induced Graphene from polymer precursors

Master's Thesis

to achieve the university degree of
Master of Science
Master's degree programme: Technical Physics

submitted to

Graz University of Technology

Supervisor
Dr. Dott. Francesco Greco

Institute for Solid State Physics
Head: Univ.-Prof. Ph.D. Peter Hadley

Graz, June 2020

Affidavit

I declare that I have authored this thesis independently, that I have not used other than the declared sources/resources, and that I have explicitly indicated all material which has been quoted either literally or by content from the sources used. The text document uploaded to TUGRAZ-online is identical to the present master‘s thesis.

Date	Signature

Eidesstattliche Erklärung

Ich erkläre an Eides statt, dass ich die vorliegende Arbeit selbstständig verfasst, andere als die angegebenen Quellen/Hilfsmittel nicht benutzt, und die den benutzten Quellen wörtlich und inhaltlich entnommenen Stellen als solche kenntlich gemacht habe. Das in TUGRAZ-online hochgeladene Textdokument ist mit der vorliegenden Masterarbeit identisch.

Datum	Unterschrift

Acknowledgments

At this point I want to thank all the people who helped and supported me to finish my master thesis.
I am really grateful to my supervisor, Francesco Greco, who gave me the opportunity to be a part of his research team. Also many thanks to my colleagues, new found friends, the Felmi institute and the ISOF for being interlocutors, providing me the needed measurement equipment and samples.
Further I would like to thank my family, Stefan, Jana and Nils as well as my mates Christian, Anna and Laura for their mental support.

Abstract

Laser Induced Graphene (LIG) was discovered by chance in 2014 and ever since it has been a far-reaching field of research. It is a porous and conductive carbon material produced by laser-induced pyrolysis of various polymer substrates, [1] . An infrared laser, as typically used in commercial CO_2 laser cutter in manufacturing, is used for this purpose. A dense forest of carbon fibres or a flat porous LIG can be obtained by a careful tuning of processing parameters, which also influences the formation of more crystalline or amorphous structure. This process allows fast and mask-free scribing of circuits onto insulating substrates in ambient condition.
Besides the interest in research, there is a huge potential for the usage of LIG in industry. Present application areas are stretchable and wearable electronics, actuators, sensors and energy (supercapacitors, batteries), just to name a few.

The main goal of this thesis is to get a better understanding of the laser-induced synthesis, the boundary conditions for the formation of LIG and the tuning of its morphology and properties. An in depth investigation of fundamentals about LIG production and properties has been carried out, in order to achieve a controlled and reproducible procedure. To this purpose, the crucial factor is to determine the laser fluence (i.e. optical energy per scribed area) which is controlled by the various laser scribing parameters, namely: the power, the speed, the resolution, the beam spot size/focusing distance. Based on the results of such investigation a software tool has been developed for the estimation and mapping of laser fluence for any given set of scribing parameters and pattern design.

Until now Polyimide (PI) was used as a precursor for the LIG production. Due to the increasing environmental concerns and in view of expanding the field of applications, a second objective is to investigate alternative polymer precursors. A preliminary investigation into the development of some biologically derived and biodegradable polymer precursors was made (e.g. starch-based biopolymers). The challenge here is to enable the laser pyrolysis conversion of the bio-precursor into LIG instead of being afflicted by melting/degradation and burning processes in ambient condition.

Composition, structure of the various LIG materials were characterized with optical microscopy, Raman spectroscopy, SEM, TEM, and correlated to their respective electrical properties.

Contents

List of Figures

List of Tables

Abbreviations

cw	continuous wave
fwhm	full width at half maximum
HPDFO	High Power Density Focusing Optics
ID	Image Density
IR	Infrared
ISOF	Institute of Organic Synthesis and Photoreactivity
LAMPSe	Laboratory of Applied Materials for Printed and Soft electronics
LIG	Laser Induced Graphene
LIGP	Standard porous and flat-LIG sample
LIGF	Standard LIG- fibre sample
MA	Medical Adhesive
PI	Polyimide
PLA	Poly(lactic acid)
PPC	Pulses Per Centimetre
PPI	Pulses Per Inch
PRF	Pulse Repetition Frequency
PVC	Passive Voltage Contrast
PVD	Physical Vapour Deposition
SEM	Scanning Electron Microscope
TEM	Transmission Electron Microscope
ULS	Universal Laser System

1. Introduction and Motivation

Laser Induced Graphene (LIG) is a 3D porous and conductive carbon material produced from a non conductive polymer sheet by treating it with radiation of an IR CO_2 laser. The photothermal and photochemical process transforming the insulating polymer into LIG is called Laser Induced Pyrolysis. [1]
There is a far reaching field of different applications, starting from stretchable and wearable electronics, sensors and actuators to supercapacitors. Hence a grand interest in research as well as industry exists demanding a controllable formation of LIG.[1]
Several previous studies evidenced that, by tuning the process parameters two different LIG types can be obtained, characterized by different morphology and composition, [2]. A first type is often called **flat**-LIG or LIG porous, owning a 3D porous structure. The second is called LIG-**fibres**, where a forest of ultrathin and long fibres emerges from the laser-treated surface of the polymer precursor. Schematics and SEM images of both types are displayed in figure 1.1.

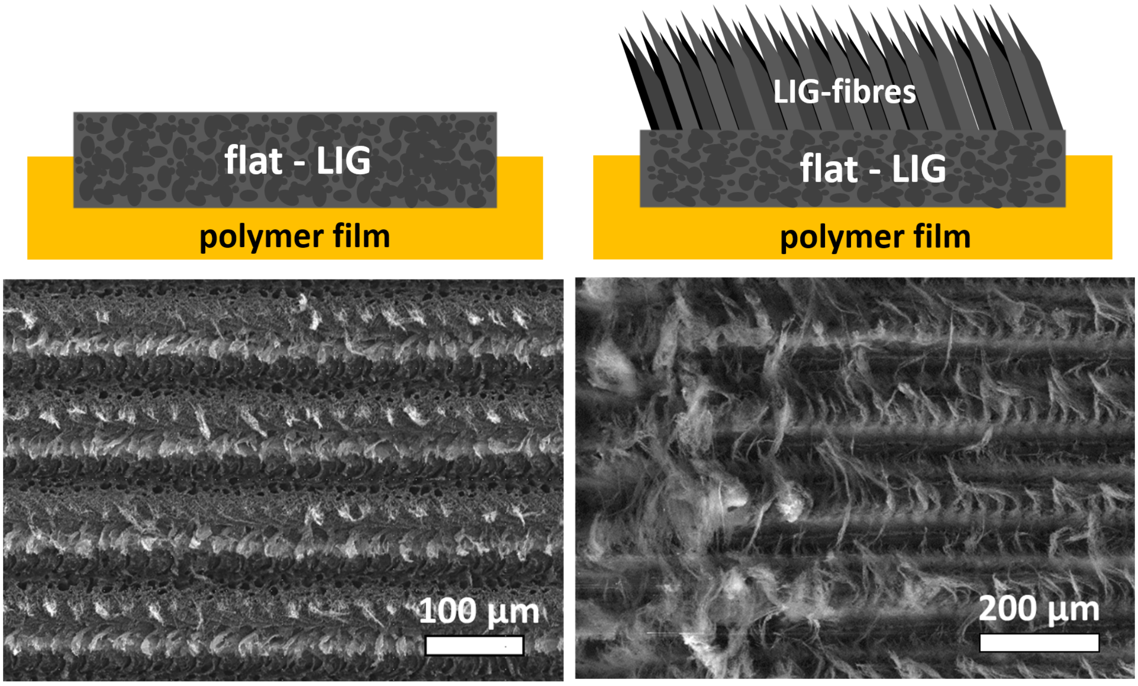

(a) Schematic cross section and SEM image in top view of flat-LIG

(b) Schematic cross section and SEM image in top view of LIG-fibres

Figure 1.1.: Observed LIG types

Former investigations (see [3]) on these LIG types were carried out at the *Laboratory of Applied Materials for Printed and Soft electronics* (LAMPSe) of Institute of Solid State Physics, TUGraz. A set of suitable laser processing parameters in order to get the desired LIG morphology on top of a commercially available *Polyimide* (PI) sheet were found after a preliminary empirical investigations. Among the various available laser processing parameters, just power and speed setting were varied. Therefore a map of different laser power and processing speed settings was produced, which can be seen in figure 1.2.

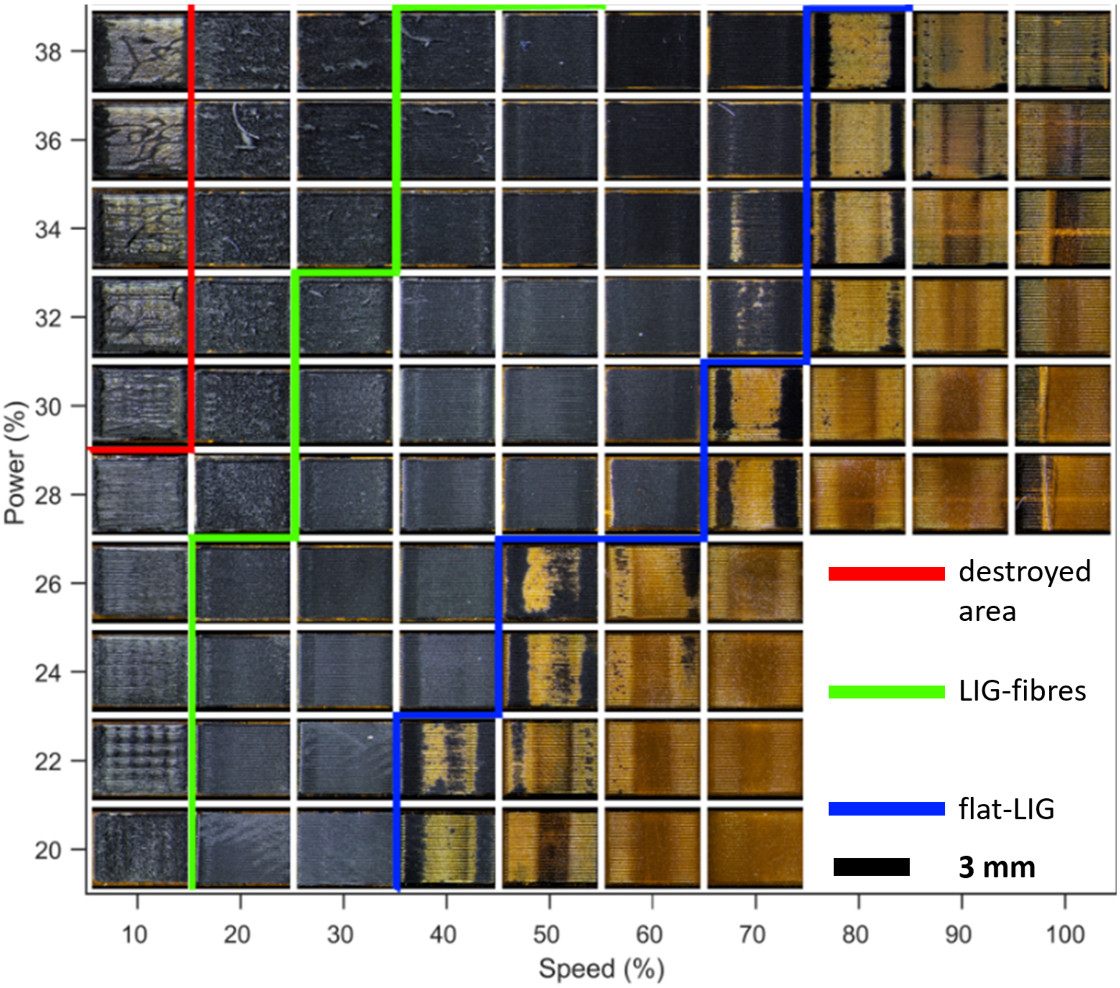

Figure 1.2.: Mapping of different LIG morphologies obtained on a commercially available PI sheet by a change of process parameters, adapted from [3]

The area masked in red in the map refers to a destruction of the material as a result of high laser fluence (i.e. high power and low speed). In the green region LIG-fibres and in the blue one flat-LIG were found. For all the other chosen settings no homogeneous formation of LIG was obtained as a result of insufficient laser fluence (i.e. low power and high speed).

One main motivation for this thesis was to find a physical description regarding the influence of process parameters on the LIG morphology and its composition. Indeed, while the previous investigation permitted to optimise some operative processing sets, a real and in depth understanding of the process was missing. First and foremost, a precise correlation between each set and laser fluence is mandatory. Little or nothing was known about LIG composition and how this varies within the 3D structure or with varying processing conditions. In particular, including all the laser processing parameters is needed to achieve the possibility to fine tune the morphology, composition and -in turn- the properties of LIG.
For the production of LIG a synthetic PI film was used as a precursor. Due to the rise in environmental awareness and in order to reduce the CO_2 footprint of these laser scribed conductive materials, a second main motivation for this thesis was to find a biologically-derived polymer as alternative LIG precursor.

1.1. Objective

The objective of this thesis was to get a better understanding of production, morphology and composition of LIG and to investigate biological precursors as an alternative to synthetic polymers.
Therefore the thesis splits into two main parts:

1. Investigation of effects on LIG morphology and composition caused by different laser processing parameters

2. Preliminary development of a biological polymer precursor for the production of LIG

2. Background Information

2.1. Laser Induced Graphene

In 2014 a research team from the Rice University, under the guidance of Prof. James M. Tour, discovered the formation of *Laser Induced Graphene* (LIG) by an accidental CO_2 infrared laser treatment of a *Polyimide* (PI) sheet, [4]. In general LIG can be seen as a porous 3D graphene, which is producible in a cost-effective and fast way, [1]. The emphasised characteristics of LIG are a high surface area, thermal stability and good electrical conductivity. Hence, it is used for different purposes like medical use, sensing, actuation and energy, [2]. In the following, the terms Graphene and Graphite, the state of arts regarding requirements for a suitable LIG precursor, formation, composition and morphology of LIG will be introduced.

2.1.1. Graphene and Graphite

Graphene is a 2D material with a honeycomb crystal lattice made up of carbon atoms, seen in figure 2.1, known for its thinness and strength. [5]

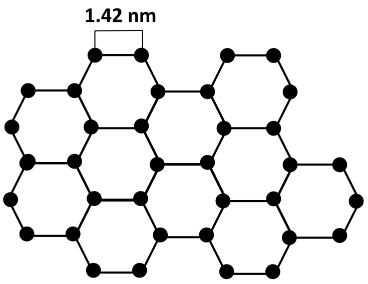

Figure 2.1.: Honeycomb structure of carbon atoms

A stacking of such 2D layers is known as a 3D material, called Graphite. The stacking of Graphite usually is characterized by a 60 ° shift between the single layers, called Bernal stacking. Lattice defects and deviations of the stacking angle can lead to a reduction of electrical conductivity. [5]

2.1.2. Laser Induced Pyrolysis and precursor requirements

The process transforming a nonconductive polymer sheet into a conductive and carbonic material with laser radiation is called Laser Induced Pyrolysis. It is a photothermal and photochemical transformation taking place at temperatures higher than 900 °C in an ambient or inert environment. The ambient environment can lead to a burning and degradation processes of the precursor instead of transferring it into LIG. Hence, a right choice of precursors has to be made. The requirements for a suitable LIG precursor are a strong absorption in the optical range of interest (i.e. at IR laser emission wavelength), it should be carbonaceous and also stable at high temperatures. Since most biological materials do contain carbon but lack fire-retardant properties most research groups pass over the difficulty of finding a proper biological derived LIG precursor by performing experiments inside an inert gas chamber.

As laser radiation gets absorbed by the precursor, it was found that for different used laser wavelengths the produced LIG and its pyrolysis mechanism were varying because of a changing in precursors transmission behaviour. Most research groups, including LAMPSe, where this thesis project was carried out, adopt CO_2 lasers in the long-wavelength infrared regime, working in an ambient environment with *Polyimide* (PI) as a precursor. [1], [6], [7]

2.1.3. Laser Induced Pyrolysis on biological materials

In order to form LIG on top of inexpensive, naturally occurring and biodegradable materials, to decreases the CO_2 emission an effort was made to find suitable lasering conditions.
As mentioned before, most biological materials are not very flame-retardant on their own. Hence, there are three existing ways to produce a conductive layer on top of biological materials (e.g. wood, cloth, food...):
I) usage of an inert environment during the laser process, [1]
II) performance of a multiple lasing process, [30]
III) usage of flame-retardant additives, [7]

An aim of this thesis would be to investigate a biological derived precursor able to be pyrolised into a conductive material in an ambient lasering environment.

2.1.4. Formation and morphology of LIG derived from PI

Since lasers are used to produce LIG, it is a very fast process, which leads to a rapid heating of a precursor. Thus, the laser induced pyrolysis takes place at very high temperatures. To control the outcome, in terms of conductivity, morphology, e.t.c., a quantity called laser fluence (i.e. optical energy per scribed area), see section 2.4, is used. [8], [2]
The Tour group found that, regardless to the maximum power of the used laser, the PI precursor was transformed into conductive carbonaceous material after lasering it with a laser fluence of around $5\,\mathrm{J}\cdot\mathrm{cm}^{-2}$. The arisen LIG morphology is porous and called flat-LIG. By increasing the laser fluence a morphology named LIG-fibres, owning a fibrous structure containing a myriad of ultrathin carbonaceous fibres joining together in bundles, was found for fluence values higher than $40\,\mathrm{J}\cdot\mathrm{cm}^{-2}$. Hence, a way to control the LIG morphology is to change the laser fluence. [9]

2.1.5. Composition and properties of LIG derived from PI

A non-destructive way to determine the LIG composition and to confirm the production of Graphene or Graphite is to use Raman spectra. More details regarding the characteristics of Graphene spectra can be found in section 2.5. Majority of research groups were using this tool to confirm the production of a Graphene material and to find structural differences between the two main obtained structures, flat-LIG and LIG-fibres. [1], [9], [2].
Although one group detected a structural change along the LIG growth, no in-depth research about this behaviour has been performed. [6]
In general it was found that LIG has a high conductivity, high surface area and is stable at high temperatures. The possibility of creating any imaginable and conductive shape

as well as the easy handling and further processing led to an extremely broad spectrum of applications, e.g. sensors, supercapacitors, actuators. Since every application needs a specific set of properties, like high conductivity, wettability or high surface area, which for example is referred to a high porosity of the LIG surface, a controlled adjustment of LIG morphology is crucial. Hence, a connection between laser fluence, LIG morphology and properties is in demand. [1], [2].

2.2. Pulsed Laser

Since a pulsed CO_2 laser engraver in the IR regime was used for the LIG production, the general concept regarding the working principle of such a laser was introduced.
Lasers can operate in a continuous wave (cw) or a pulsed way. An ideal cw-laser provides an uninterrupted and energy stable beam, characterized with a power P_{max}, see figure 2.2.

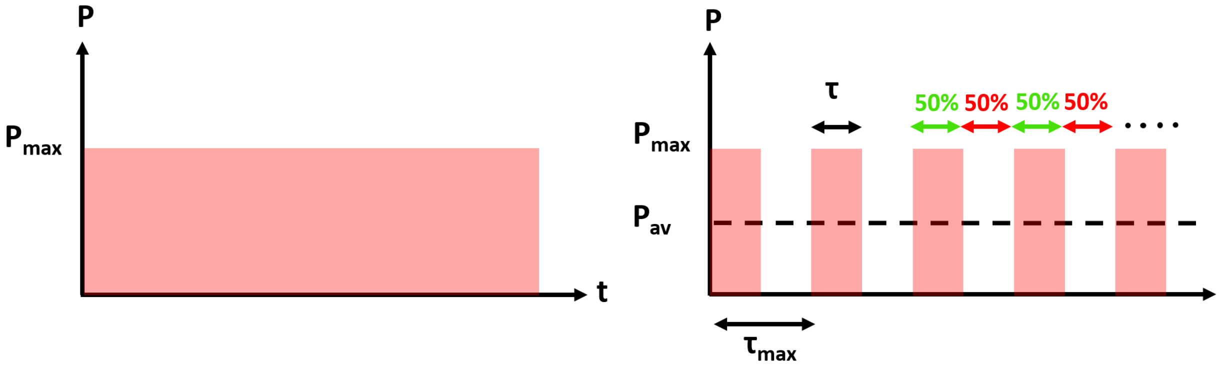

Figure 2.2.: Duty cycle of a cw-laser and a pulsed laser with an duty cycle of 50%

A pulsed laser on the other hand produces light pulses with a certain maximal pulse power P_{max}, a duration τ and a time from pulse to pulse τ_{max}. Another way to describe the number of pulses generated in a specific time is by using the Pulse Repetition Frequency (PRF) f_{rep}, which is defined as the reciprocal of τ_{max}. The so called duty cycle describes the ratio between the time the laser is on and the time it is off, and it is often expressed in %. Thus, a cw-laser has a duty cycle of 100 % and a pulsed-laser a lower one. With these quantities the average power (P_{av}) of a pulsed laser can be defined as:

$$P_{av} = \frac{P_{max} \cdot \tau}{\tau_{max}} \tag{2.1}$$

For a better understanding of the working principle of a pulsed laser see figure 2.2, exemplary with a duty cycle of 50 %.

2.3. Gaussian beam theory

The transverse intensity profile of almost all lasers, including the one used at LAMPSe, can be described with a Gaussian function. To understand the effect of single laser pulses to the polymer precursor, combined with the possibility of defocusing the laser regarding to the surface of a precursor, concepts of the Gaussian beam theory are introduced.
For a propagation of the laser beam in forward direction Z the beam radius r(Z) and the curvature radius R(Z) are changing, see
figure 2.3.

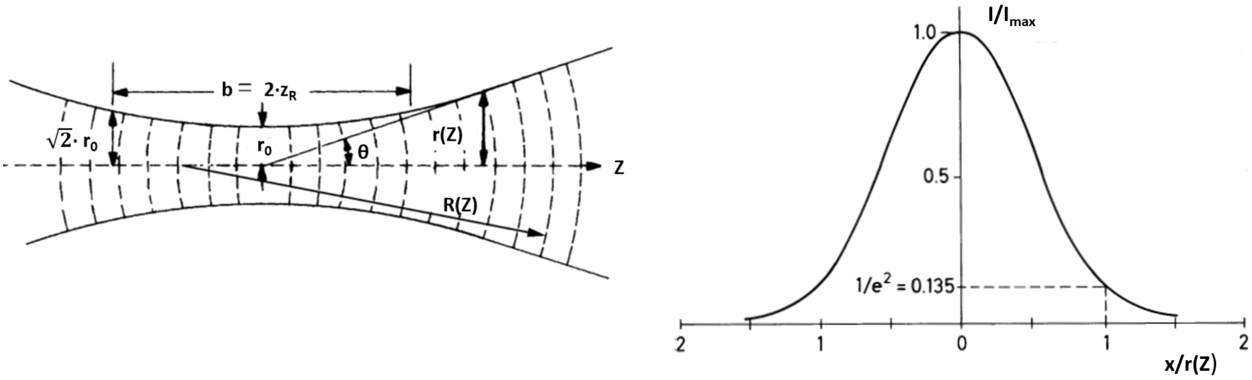

Figure 2.3.: Gaussian beam propagation, adapted from [10]

The Rayleigh length z_R defines the distance in Z-direction where the beam radius decreases to $\sqrt{2}$ times the focused radius r_0. To calculate the theoretical spotsize s_{theo}, needed for the fluence calculation in equation (2.9), two different regimes are used depending on z_R, [10]:

$$r(Z) \ = \ r_0 \cdot \sqrt{1 \ + \ \frac{Z^2}{z_R}} \qquad for \ Z \backsim z_R \tag{2.2}$$

$$r(Z) \ = \ r_0 \cdot \frac{Z}{z_R} \qquad for \ Z \gg z_R \tag{2.3}$$

Following the laser spotsize s_{theo} can be defined as,:

$$s_{theo} \ = \ \pi \cdot r(Z)^2 \ = \ \pi \cdot \left(\frac{d(Z)}{2}\right)^2 \tag{2.4}$$

where d is defined as the spot diameter. The transverse laser intensity profile has a Gaussian shape and depends on the radial distance from the center (x) and the beam radius (r(Z)):

$$I(x) \ = \ I_0 \cdot exp\left(-\frac{2 \cdot x^2}{r(Z)}\right) \tag{2.5}$$

Knowing the total power, the intensity at the middle of the laser beam (I_0) can be calculated with:

$$I_0 \ = \ \frac{P}{r(Z) \cdot \pi} \ = \ \frac{P}{s_{theo}} \tag{2.6}$$

For discussing the laser heat (Q) absorbed by the precursor during laser scribing, two factors were taking into account:

I) absorption of optical (IR) radiation and II) specific heat.
Beer-Lambert's law, described the absorbance of optical radiation dependent on the absorption coefficient (δ) and the thickness of the material (d). The specific heat (c), describes the amount of heat that has to be absorbed (ΔQ) by a material with a mass (m) to cause a temperature rise (ΔT). Both factors were taken into account, [11]:

$$Q = I_0 \cdot \delta \cdot exp(-\delta \cdot d) \tag{2.7}$$

$$c = \frac{\Delta Q}{m \cdot \Delta T} \tag{2.8}$$

2.4. Laser fluence

The laser fluence (H) is defined as the optical energy per scribed area. It is a powerful tool to make experiments controllable and reproducible. Moreover, calculating the laser fluence for each scribing condition make it possible to compare results obtained by different research groups, which typically adopt laser systems with different P_{max}, speed, etc..
In order to calculate the fluence the following equation was used,:

$$H = \frac{P_{av}}{s_{theo} \cdot v \cdot PPC} \left[\frac{J}{cm^2}\right] \tag{2.9}$$

where P_{av} is the average laser power (calculated after equation (2.1)), s_{theo} is the theoretical laser spotsize (see equation (2.4)), v is the measured processing speed and *Pulses Per Centimetre* (PPC) is the amount of laser spots per cm. Since the number of spots per unit length is given as *Pulses Per Inch* (PPI) (see section 3.3) one has to convert it to PPC to make further calculations, [12]:

$$PPC = \frac{PPI}{2.54} \tag{2.10}$$

2.5. Raman Spectroscopy

To investigate the composition of the produced LIG in a non-invasive way a *Raman*-spectrometer was used.
In general Raman bands are caused by inelastic scattering processes of incoming probing photons by matter.
The incoming photon can get scattered by the molecules, which can get excited into a virtual energy state, see figure 2.4. When the excited state relaxes back into ground state, a photon with the same energy as the incident one is emitted, called Rayleigh scattering process. In case the excited state relaxes into another virtual state, with a change in rotational and vibrational energy, a process called Raman scattering takes place.

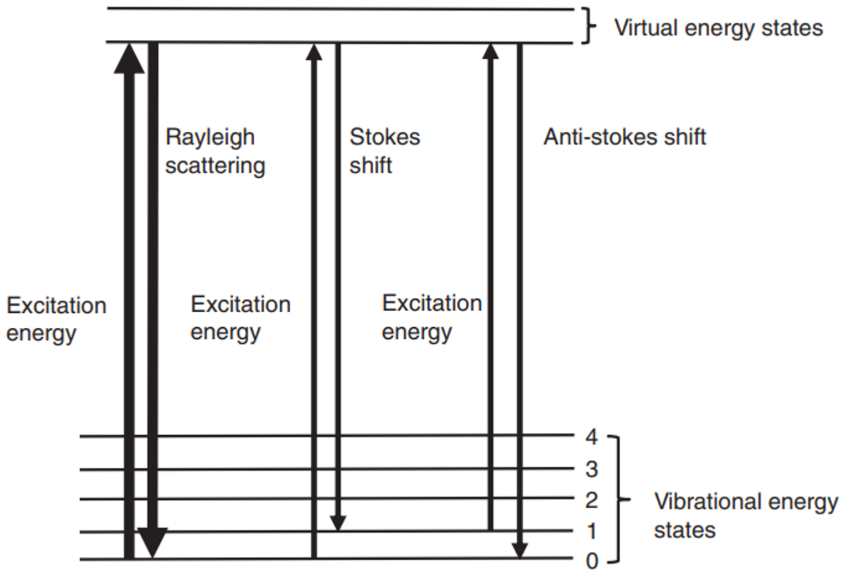

Figure 2.4.: Energy-level diagram of Raman scattering, adapted from [13]

If the energy of the final state is higher compared to the initial state, the energy of the emitted photon is smaller compared to the Rayleigh photon and Raman bands are shifting to shorter wavelengths, called Stokes-lines. For final states with a lower energy it is the other way around and they are called anti-Stokes lines. Since the intensity of Stokes lines is higher than for anti-Stokes lines (initial state energy of Stokes-line is lower, leading to a higher population and thus, the probability for this process is higher), the Raman spectra show the intensity of the Stoke lines against the Raman shift (cm^{-1}). Each Raman band is referred to a vibration of either a chemical bond or to a functional group of the probed molecule. [13]

To guaranty a monochromatic beam of photons probing the sample, a laser, typically in a wavelength range of (800-500) nm is used, which further ensures high Stokes-intensities, since it is proportional to the intensity of the incoming light. [13]

2.5.1. Raman analysis of carbonic samples

Typical Raman spectra of carbonaceous samples show characteristic bands, which can differ in width, intensity and also in band position, see figure 2.5. This allows for discriminating between amorphous and crystalline structures.

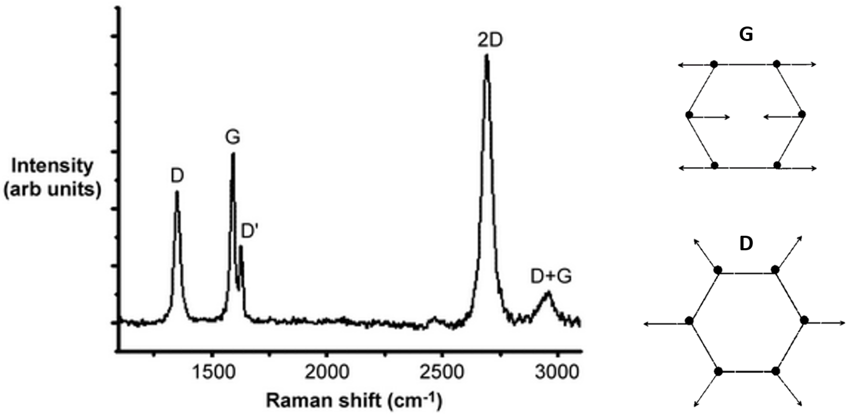

Figure 2.5.: Typical Raman spectrum for a carbonaceous sample and stretching modes associated with G- and D-band, adapted from [14]

The G band (1580 cm^{-1}) arises due to the stretching of C-C bonds and is representative for the presence of sp_2 carbons. The D band (1350 cm^{-1}) is a breathing mode and can be observed in case of defects or disorder in the sample, see figure 2.5. Unlike the G mode the D band intensity varies with the photon excitation energy (dispersive).

Both peaks are characteristic for an amorphous or a nanocrystalline carbon structure. In order to distinguish between those two, following features should be investigated:

The width of a Raman peak refers to the order in structure:
A narrow band is a sign for a more ordered structure, while broad bands indicates a disordered one.

Further, the 2D peak (2700 cm^{-1}), which is an overtone of the D band, is a good indicator for the nature of the sample:
A narrow and strong 2D peak can be found for structures with a high 3D order and it disappears for samples with an increasing amount of defects and disorder.

To describe a compositional change, starting from tetrahedral amorphous carbon (ta-C) to amorphous carbon (a-C) to nanocrystalline grahite (NC-Graphite) and finally to Graphite, a phenomenological schematic trend of the G band position and the intensity ratio (I_D/I_G) seen in figure 2.6 were used, [14].

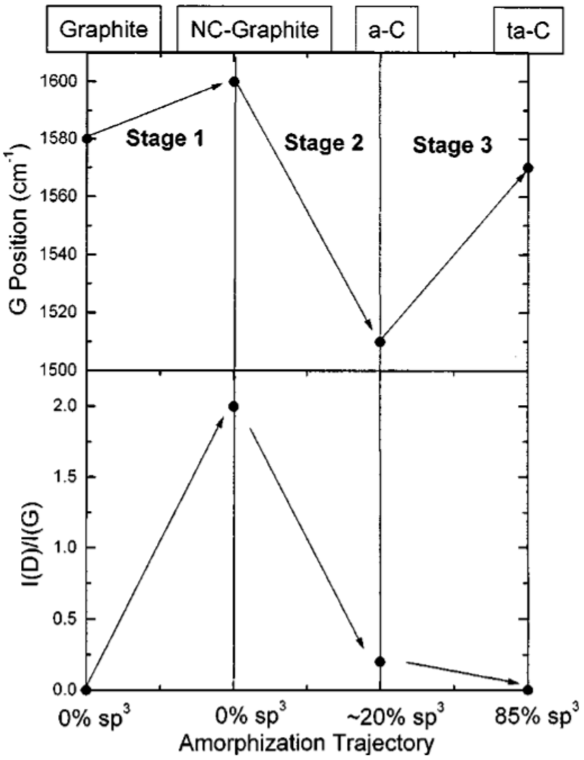

Figure 2.6.: Schematic trend for G band position and I_D/I_G versus change in composition and phase (i.e. sp3 carbon content, crystalline/amorphous), [14]

In stage 1 the G band position increases from $1580\,\mathrm{cm}^{-1}$ to $1600\,\mathrm{cm}^{-1}$ and also the D band starts to emerge. The grain size (L_a) can be estimated with the intensity ratio and a wavelength dependent constant C(λ), see equation (2.12):

$$L_a = C(\lambda) \cdot \frac{I_G}{I_D} \tag{2.11}$$

It was observed that the intensity ratio changes for different values of excitation energy and therefore for varying laser wavelengths λ. Hence the factor C(λ) was introduced to obtain same results for I_D/I_G, independent of the used excitation energy . For calculating C(λ), the following equation was used, [15]:

$$C(\lambda) = C_0 + C_1 \cdot \lambda \tag{2.12}$$

After [16] the values for C_0 and C_1 turned out to be: $C_0 = -126\,\text{Å}$ and $C_1 = 0.033$.

When changing from NC-Graphite to a-C, seen in stage 2, the amount of defects increases and the G band position starts to decrease again to around $1510\,\mathrm{cm}^{-1}$. Also the intensity ratio approaches zero. To calculate the crystalline size in this stage, equation (2.13) was used, [14], [15]:

$$L_a = \sqrt{\frac{I_D}{I_G} \cdot \frac{1}{C_1}} \tag{2.13}$$

2.5.2. Mechanical properties

One possible application of MA/LIG composites are stretchable conductors. To characterize the mechanical properties a device called Stretcher, for tensile testing, was developed by LAMPSe, connecting an applied strain (ϵ) with change in normalized resistance (R/R_0) and an energy loss (C) due to plastic deformation of the material.
At a plastic deformation the material does not return to its original shape, recognisable in the stress-strain curve, see figure 2.7 - marked with a green arrow. Viscoelasticity is characterized by a hysteresis in the stress-strain curve, where the stretching of the sample takes more energy than the relaxing process - explainable by an energy loss through heat.
While R/R_0 can be read off the R/R_0-strain plot, the energy loss (C) was calculated by comparing the energy applied to the material (E_S: area under the stress-strain curve while stretching the sample) and the one released during the relaxing process (E_R: area under the stress-strain curve while relaxing the sample), see equation (2.14) and figure 2.7.

$$C = \frac{E_S - E_R}{E_S} \tag{2.14}$$

Schematic measurements and the mentioned quantities can be found in figure 2.7, where the normalized resistance at maximal applied strain (R_s/R_0) and at relaxed state (R_r/R_0) can be seen on the left side and a stress-strain curve, the energy loss C - visualized as the blue marked area between the two curves, and the plastic deformation as the green arrow, on the right side. [2], [3].

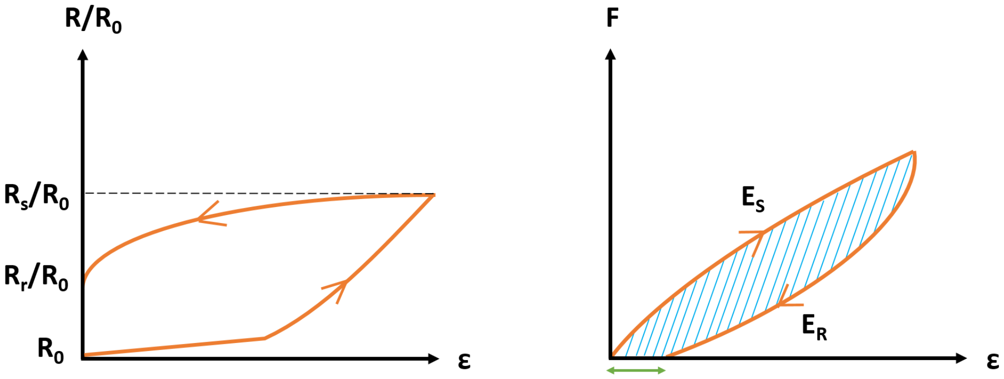

Figure 2.7.: Schematic trend for Stretcher measurements showing the normalized resistance on the left side and the stress-strain curve with a plastic deformation on the right side

For a more detailed explanation of the working principle of the stretcher see section 3.5.2 and [3].

3. Experimental

3.1. Polymer precursors

During the Laser Induced Pyrolysis a non-conductive polymer precursors gets transformed into a conductive carbon material. The requirements for a suitable LIG precursor are: strong absorption in the IR range (i.e. at same wavelength of the laser scribing equipment used), it should contain carbon and have a stability at high temperature (i.e in Laser Induced Pyrolysis a local temperature of around 1000 °C is estimated). [17]

3.1.1. Polyimide film

One appropriate precursor is *Polyimide* (PI). The chemical structure can be found in figure 3.1.

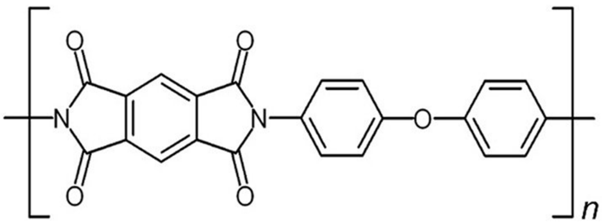

Figure 3.1.: Chemical structure of Polyimide, [18]

For experiments performed in this thesis commercially available PI sheets (Kapton® HN,*DuPont*) with a thickness of 50 µm were used, without further treatments before processing.

3.1.2. Biological precursors

The formation of LIG on top of two different bio-polymer precursors was tested, one of them was based on corn starch and the other one on keratin.

Corn starch matrix - Star-0

A corn starch based polymer precursor for LIG, called Star-0, was produced as follows.
Corn starch (Maisstärke, *Maizena*) was mixed with deionized water, vinegar ((4 - 8)%, 45731, *Fluka*) and glycerol (99.5 %, *Sigma-Aldrich*) in a beaker with a magnetic stirrer, see table 3.1 for quantities. The mixture was stirred at T = 200 °C until it started to boil (∼(5 - 10)min). Once the mixture became viscous it was manually spread on top of Al foil, to let the produced film set and dry in an oven over night at T = 40 °C. [19]

Star-X

The Star-X precursor was produced like Star-0, with the difference that X wt%, see table 3.1, of Fe(NO_3) (Fe$(NO_3)_3 \cdot 9H_20$, *Merck*), was added right before the heating process started.

Table 3.1.: Recipe for Star-X

Star-0	
corn starch	9.5 g
deionized water	60.0 g
vinegar	5.0 g
gycerol	5.0 g

	$Fe(NO_3)$ / wt%
Star-0	0
Star-1	1
Star-2	2
Star-3	3
Star-4	4
Star-5	5

Keratin based precursor

Two keratin-*Poly(lactic acid)* (PLA) based sheets, with different manufacturing processes, were provided by Dr. A. Aluigi from the *Institute of Organic Synthesis and Photoreactivity* (ISOF).

Production of Keratin-PLA mixture: The used keratin(Keratin, *Kerline srl*) was derived from wool of dairy sheep and has an alpha-structure, and PLA (IngeoTM Biopolymer 4060D, *NatureWorks LLC*) is a totally amorphous biopolymer. The keratin and the PLA were separately dissolved overnight in Hexafluoroisopropanol (HFIP) at a concentration of 10 % and then mixed together in a (50/50) ratio.

Electrospun film: To generate an electrospun film out of the keratin-PLA mixture, a electric field of 18 kV was applied between two 15 cm separated electrodes. The flow rate of the liquid mixture was $0.03\,\frac{\mathrm{mL}}{\mathrm{min}}$ and about 4 mL were deposited on an Al-substrate during the electrospinning process.

Cast film: The same liquid keratin-PLA mixture, which was used for the electrospun film, was spread on the Al-substrate by using a threaded rod.

Both keratin based films were directly deposited on the substrate and remain attached due to adhesive properties of keratin.

3.2. Medical Adhesive

For the production of stretchable conductors a commercially available, transparent and adhesive tape, namely Fixomull (*BSN medical GmbH*) , short *Medical Adhesive* (MA), was used. It is composed of a polyacrylate adhesive and a polyurethane layer having a total thickness of (54 ± 6) µm. [3], [2]

3.3. Laser cutter

For the production of LIG a commercial IR CO_2 laser cutter/engraver from *Universal Laser System* (ULS), VLS 2.30, equipped with an additional High Power Density Focusing Optics (HPDFO), was used, see figure 3.2. The laser specifications can be found in table 3.2.

Figure 3.2.: Laser cutter of Universal System, Model VLS 2.30

Table 3.2.: Laser specifications, [20],[21],[22]

Model		VLS 2.30
Rated Power	P_{max}	30 W
Power stability		5 %
Wavelength	λ	10.6 µm
Pulse repetition frequency	f_{rep}	5 kHz
Depth of focus	z_R	0.005 inch
HPDFO spot-diameter	$2 \cdot r_0$	0.001 inch

During operation a well-filtered environment was suggested to prevent a contamination of the laser optics with smoke and other byproducts generated during the laser operation. Thus an air filtration unit from *TBH GmbH* was installed. To prevent the user from eye damages caused by the IR-laser, it is only on while the protective cap of the engraver is closed. Otherwise the laser carriage does move after starting a printing job, visualized by a red diode pointer, but the actual IR-laser is turned off. This can help during alignment of precursors on top of the engraving table.

For calculating the average laser power the maximal duration of one pulse (τ_{max}) was received by generating the reciprocal of the repetition frequency.
Since the laser beam diameter was necessary for further calculations the specifications concerning the depth of focus (z_R) and the spot-diameter in focal position ($2 \cdot r_0$) were converted into SI units:
$z_R = 12.7\,\mu m$; $2 \cdot r_0 = 25.4\,\mu m$
by multiplying it with a factor of 2.54. [20],[21],[22]

3.3.1. Laser modes

The laser cutter provides two operating modes, namely the raster mode, used for engraving of filled areas - and the vector mode, used for cutting single as well as complex shaped laser lines .
In both modes the laser cutter operates by scribing on the sample a pattern made out of single dots. The number of dots per unit length and therefore the distance between those dots is determined by the PPI setting. A schematic illustration of the engraving process can be seen in figure 3.3.

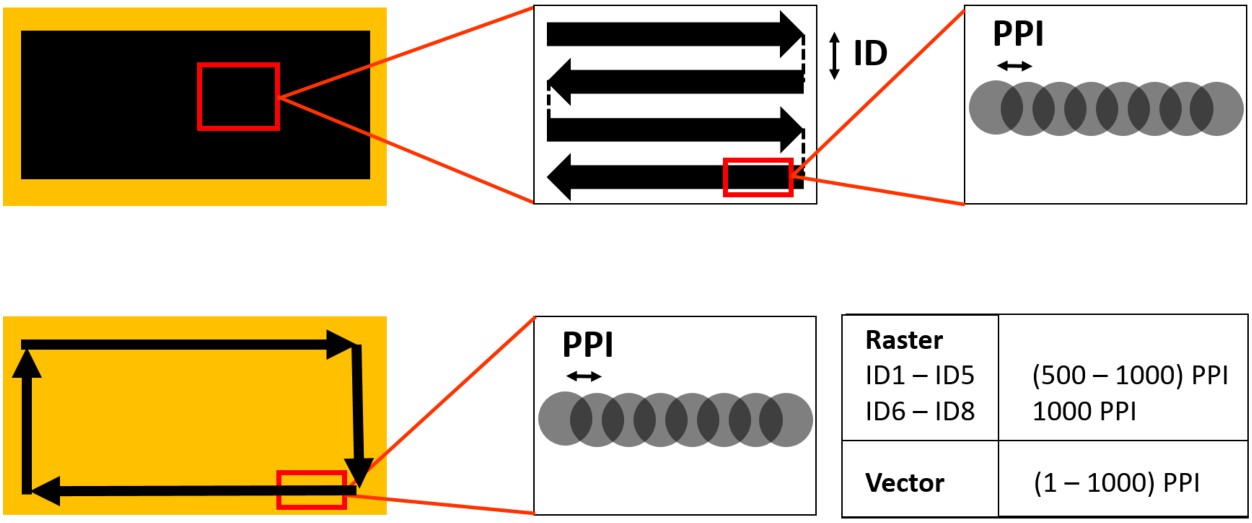

Raster	
ID1 – ID5	(500 – 1000) PPI
ID6 – ID8	1000 PPI
Vector	(1 – 1000) PPI

Figure 3.3.: Top: engraving process in raster mode
Bottom: engraving process in vector mode

Raster mode

In order to produce filled engraved areas the laser beam is scanned in a bidirectional way over the sample (see figure 3.3-top) . To describe the density of laser lines in vertical direction a parameter, called *Image Density* (ID), was introduced. A high distance between two neighbouring lines is connected to a low ID value and vice versa. An optical microscope was used to measure the distances between the laser lines for different ID settings and to count the number of lines engraved per cm, see section 3.6.
In raster mode the laser beam is on only engraving while the laser carriage is moving along the horizontal direction (x- axis). Further the number of laser spots per unit length is controlled by the ID setting: for ID1 - ID5 the minimum PPI value is prescripted to 500 PPI and for ID6 - ID8 to at least 1000 PPI (see figure 3.3).

Vector mode

The vector mode is used for engraving and cutting single lines (see figure 3.3-bottom). Unlike to the raster mode the laser beam is operating while the carriage is moving in y-direction. Therefore the main difference between those two modes is the processing speed. Moreover the PPI value can be set between (1 - 1000) PPI. [20]

3.3.2. Processing parameters of the laser cutter

In the adopted laser system five processing parameters can be tuned by the manual printer driver interface, which can be found in table 3.3. These were used to influence the LIG morphology and its composition in this study.

Table 3.3.: Laser cutter parameters,[20]

P%	Power	Laser power in percentage
S%	Speed	Laser processing speed in percentage
PPI	Pulses Per Inch	Pulses per inch in horizontal direction
ID	Image Density	Laser line distance in vertical direction
Z	Z-Axis	Setting of Laser focus on sample

The power setting (P%) is adjustable from (0.1 - 100)% of the maximal laser power ($P_{max} = 30\,\mathrm{W}$) and correspond to the duty cycle mentioned in section 2.2. This means, by setting P% = 50 %, the laser will generate an output like the one displayed in figure 2.2. S% can also be set between (0.1 - 100)% of a maximal processing speed. It is important to remark that the carriage moving velocity in raster and vector mode is not the same and therefore the speed setting S% refers to different processing speeds. As described in section 3.3.1, the PPI value can be set from (1 - 1000) PPI in vector mode and has some limitation in raster mode. To change the focal position of the laser spot on top of the sample, the engraving table can be moved in 0.1 mm steps along the z (vertical) direction. For this purpose the Z-setting is used. In doing so Z = 0 mm specifies the state where the engraving table (without a sample on top of it) is in focused position. [20]

3.3.3. Processing parameters for LIGP and LIGF

The standard settings used to produce a porous and flat LIG called LIGP, and a LIG-fibre sample with a dense forest of ultrathin fibres, called LIGF, can be found in table 3.4.

Table 3.4.: Standard laser settings for LIGP and LIGF

	LIGP	**LIGF**
P% / %	10	20
S% / %	10	10
PPI	500	500
ID	5	5
Z / mm	0.9	0.9
scribing mode	raster	raster

In general the PI sheet was attached to a supporting Al-plate (thickness 1 mm) with a double-sided adhesive tape (*Scotch*). Next, the PI sheet was placed on top of the engraving table to start the desired laser scribing job, with settings found e.g. in table 3.4.

3.4. Influence of process parameters on LIG morphology

To describe the effect of different laser settings the laser fluence (equation (2.9)) was used. It combines the influence of all the different process parameters that can be adjusted. Thus the average laser power, the processing speed, the laser spotsize and the number of laser pulses per centimetre had to be obtained.

3.4.1. Measurement of average laser power

For measuring the average laser power (P_{av}) two different detectors were used, see table 3.5.

Table 3.5.: detectors for laser power measurements,[23], [24]

Item	**Model**	**Producer**	**wavelength range**	**further information**
Thermopile sensor	PM30	Coherent	150-1100 nm	response time: 2s
Si-Photodetector	PDA10A2	THORLABS	200-1100 nm	bandwidth: 150 MHz

Thermopile sensor

The Thermopile sensor was placed on the engraving table and in attempt to prevent damaging of the detector caused by the laser, the engraving table was moved into a defocused position (Z = 40 mm), corresponding to a spotsize of around 13 mm. Several combinations of different laser processing parameters were tested in order to learn more about the working principle of the laser. For example, (5x5) mm^2 squares were engraved in raster mode with a maximum power of P = 30 %, a speed setting of S = 8 %, PPI = 500 and ID = 5. The data were read out with a FieldMaxII-TO Laser power meter from *Coherent*.

Si-Photodetector

This detector had no sensitivity to the used laser wavelength of $\lambda = 10.6\,\mu m$. However, it was possible to detect the plasma light which was emitted during the lasering process, when the laser beam hit the supporting Al-plate, placed on the engraving table, instead of the detector itself. Therefore, the detector was placed as close as possible to the Al-plate. Again, a similar set of laser processing parameters as listed for measurements with the Thermopile sensor was used.

3.4.2. Measurement of processing speed

To find the dependencies of the processing speed (v) on the speed setting (S%), pattern length (l), placement of the sample on top of the engraving table and the chosen laser mode, different measurements were taken:

In general the processing time (t_p) and the laser carriage movement (x) were recorded for different sets of pattern legths (l) with a pattern width (w) and speed settings. Those measurements were done in raster and vector mode as well as in the upper left corner and the centre of the engraving table. Due to the fact that the raster mode is used for laser treating filled areas, a rectangle with a length of l and w = 10 mm was chosen.

The processing time was recorded with a stop watch and the movement of the laser carriage was measured after the following procedure:

1. open the cap of the laser cutter
2. start desired engraving job
3. measure the movement of the laser carriage (x) by observing the red diode pointer
4. stop the engraving time

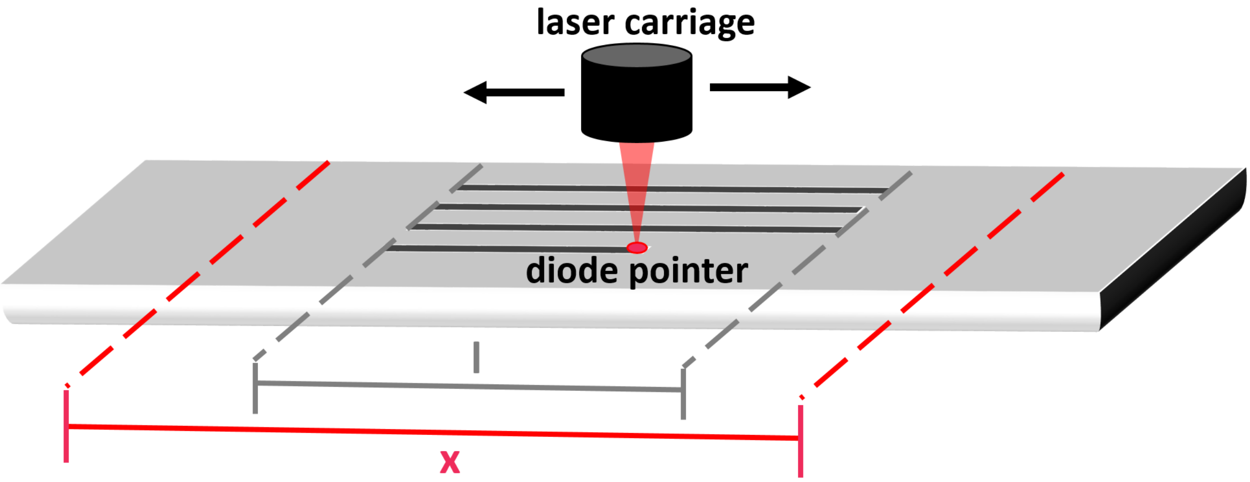

Figure 3.4.: Schematic setup for laser processing speed measurements

3.4.3. Measurement of laser spot diameter

For a precise determination of the laser spot size (s: see equation (2.4)), as well as to describe the influence of defocusing, a PI sheet sample was laser scribed in vector mode with the settings found in section 3.4.3, in order to measure the laser spot diameter (d).

Table 3.6.: Settings for spot diameter determination

mode	vector
P% / %	0.2
S% / %	8
PPI	40
l / mm	4

Single lines were engraved with different Z-settings, starting from Z = −2 mm to Z = 2 mm with 0.1 mm incremental steps.

As mentioned before, the polymer precursor itself was non-conductive. Hence, to avoid charging effect during an observation with the SEM a Ag-coating with a thickness of ∼40 nm was made by a PVD.

PVD:

The used PVD-setup at the Solid State Institute of TU Graz is displayed in figure 3.5.

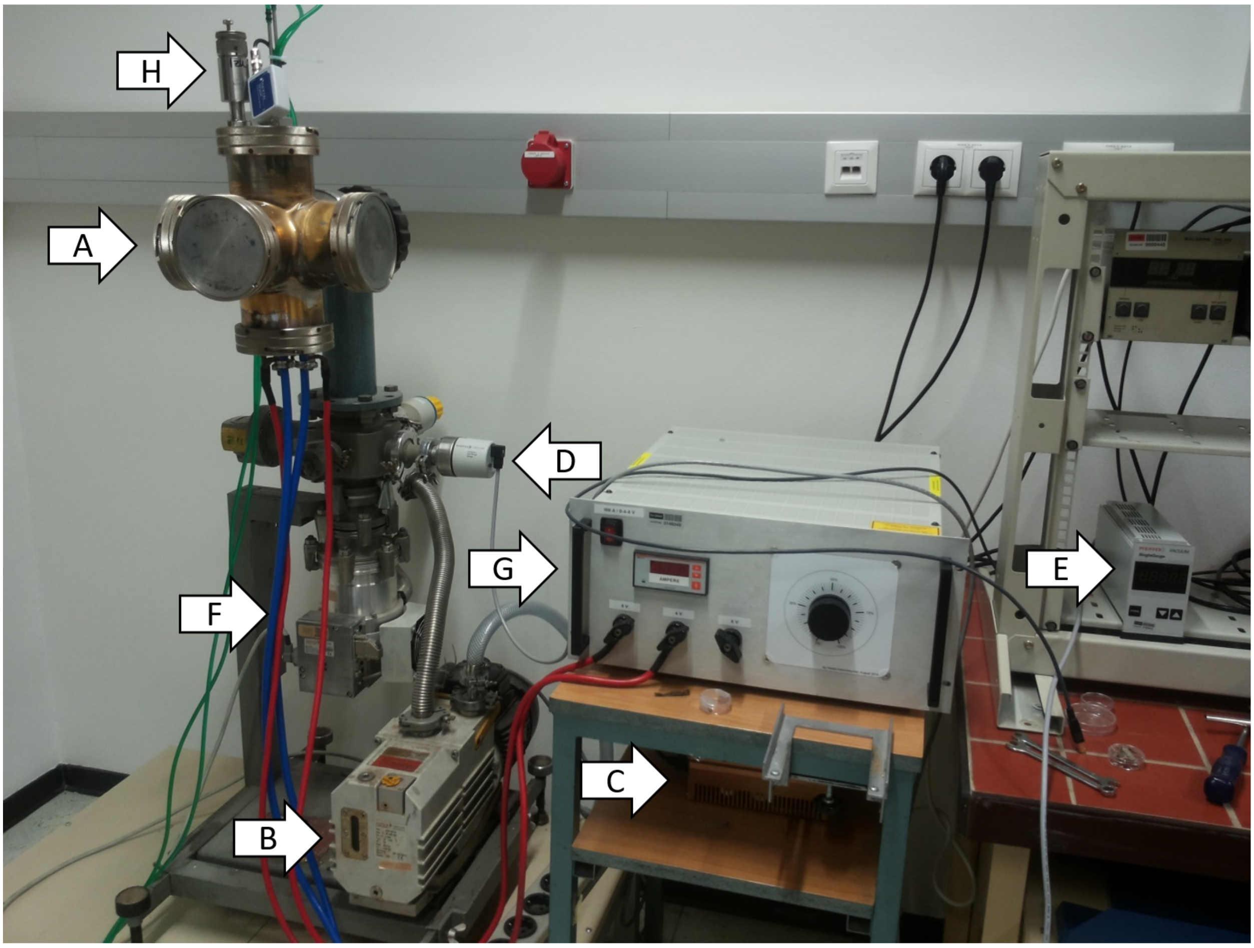

Figure 3.5.: Setup for the PVD process

The PVD chamber (A) was opened and the sample was placed on the holder underneath the top plate and a tungsten boat filled with a silver grain (99.9 %, *Sigma Aldrich*) was fixed at the bottom plate. After closing the chamber a rotary vane pump (B: DUO 010M PKD62705, *Pfeiffer*) and a turbo molecular pump (C: D-35614 ASSLAR TMH 261 PMPO2820G, *Pfeiffer*), which was activated after reaching a pressure of $p \sim 4 \cdot 10^{-1}$ mbar, were switched on to create a pressure of $p < 8 \cdot 10^{-5}$ mbar. The pressure inside the chamber was measured by (D: Vakuum Fullrange Gauge, *Pfeiffer*) and monitored by (E: Single Gauge, *Pfeiffer*). Next the cooling water (F) was turned on, the power supply (G: TMK01R1, *Lovato*) switched on and the power was adjusted in a way to see a constant and slow silver evaporation rate of ∼0.5 Å/s. After reaching this conditions the shutter (H), separating the sample from the silver vapor, was removed and the program (custom LabViev program) responsible for the thickness monitoring of the deposited silver layer was switched on. After reaching the desired silver layer thickness of ∼40 nm, the shutter was closed.

To measure the spot diameter (d), in order to calculate s for the different Z-settings, a SEM (JSM-6490LV) was used. By changing the table position out of focal position (Z = 0 mm) an increasing laser spot diameter was expected on top of the sample, see figure 3.6.

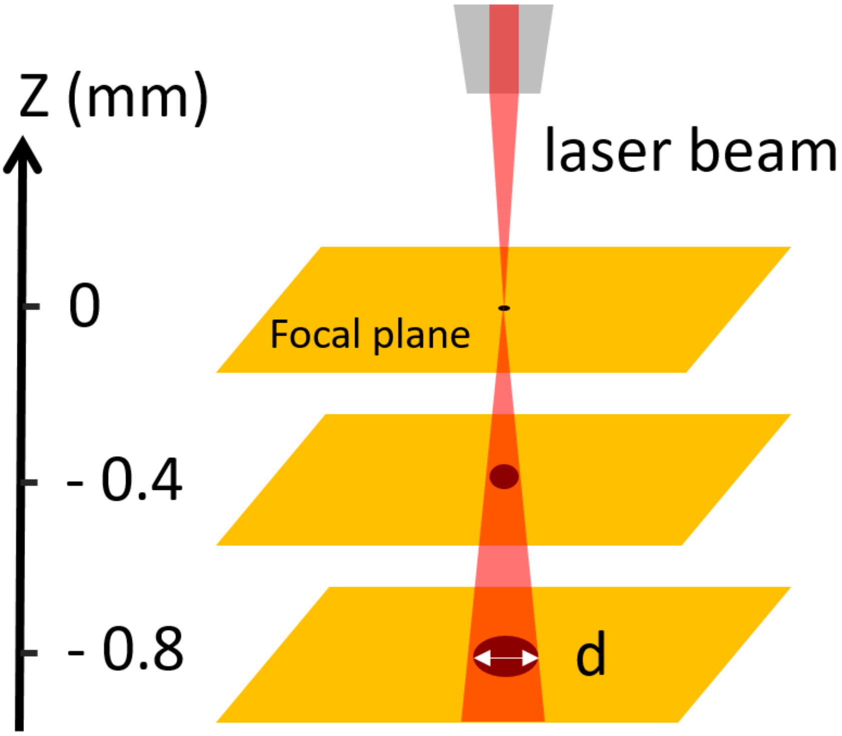

Figure 3.6.: Sketch for the theoretical laser beam spot diameter on top of a sample with different defocus Z

3.5. Influence of Image Density in raster mode on LIGF resistance

To test the influence of ID setting on resistance (R_s) of LIGF samples, laser scibred with the settings found in table 3.4, samples with ID1 to ID4 were produced with a pattern size of $l = 30\,\text{mm}$ and $w = 6\,\text{mm}$, see figure 3.8. In the following, those samples will be called LIGF-IDX, where X indicates the value for the ID-setting.

3.5.1. Resistance measurement on PI

The resistance on PI was measured with a *Fluke* multimetre. To guarantee a reproducible and comparable resistance measurement at same distances $d_R = 27.1\,\text{mm}$, a provisional frame out of wood was built, see figure 3.7. At the ends of the frame an adhesive copper band was mounted to connect with a multimetre.

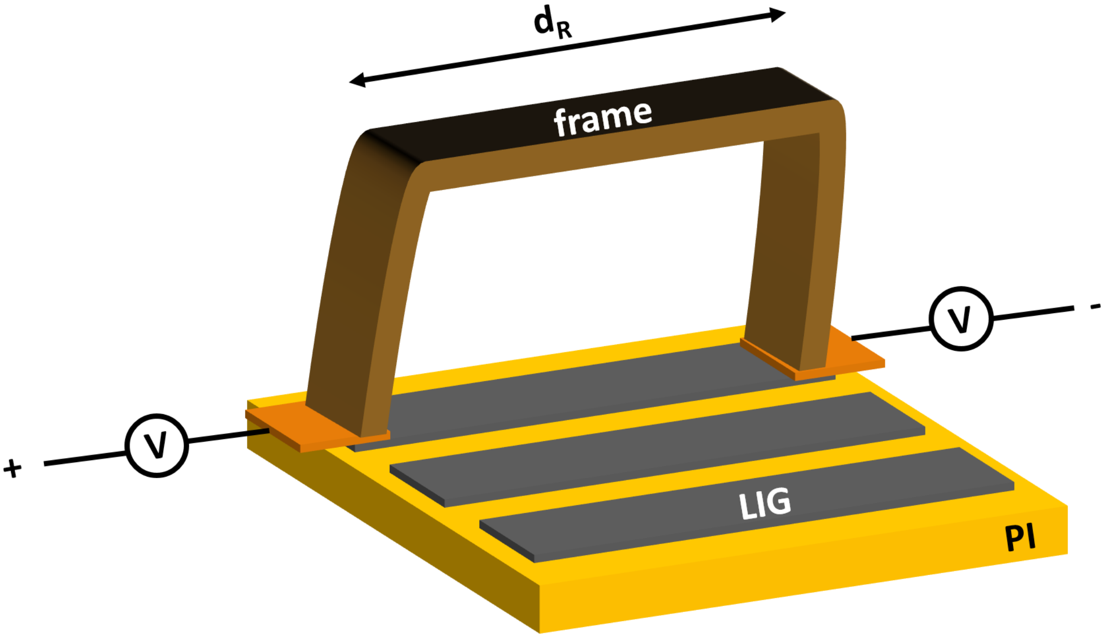

Figure 3.7.: Experimental setup for LIG sheet resistance measurements on top of PI

3.5.2. Resistance measurement on MA - Stretcher

For measuring the influence of the ID setting on stretchable conductors, the LIGF-IDX samples, described in section 3.5, were transferred from the rigid PI sheet to a flexible *Medical Adhesive* (MA). In figure 3.8 the cross section (top) and the top view (bottom) of the transfer procedure can be seen. The MA was gently placed on top of the produced LIG and than pulled off, which preferably removed the LIG-fibres from the sample, now being attached to the MA, [2].

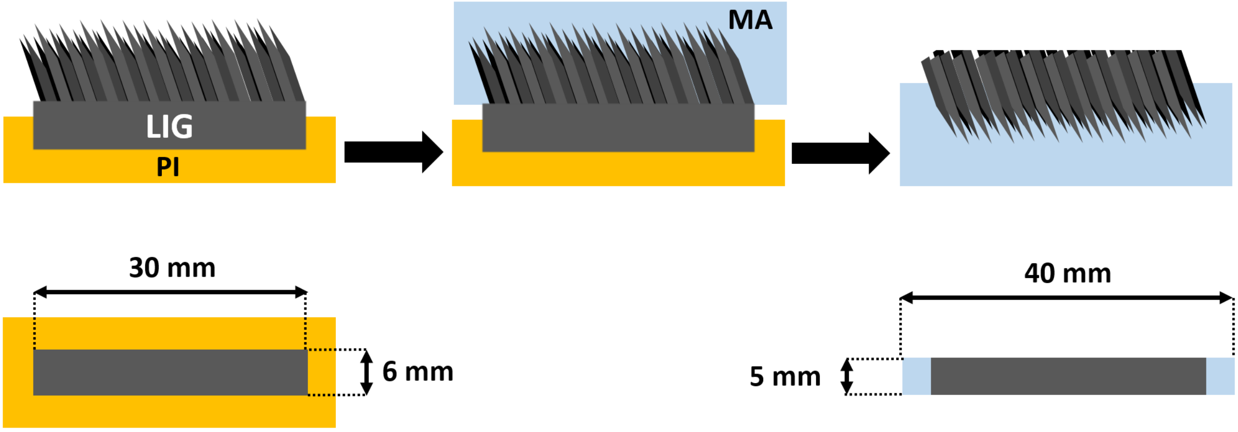

Figure 3.8.: Transfer of LIG to a medical adhesive

An experimental setup for electromechanical tensile testing, called Stretcher, developed by a former master student, was used to determine the sheet resistance under mechanical stress, see figure 3.9. [3], [2]

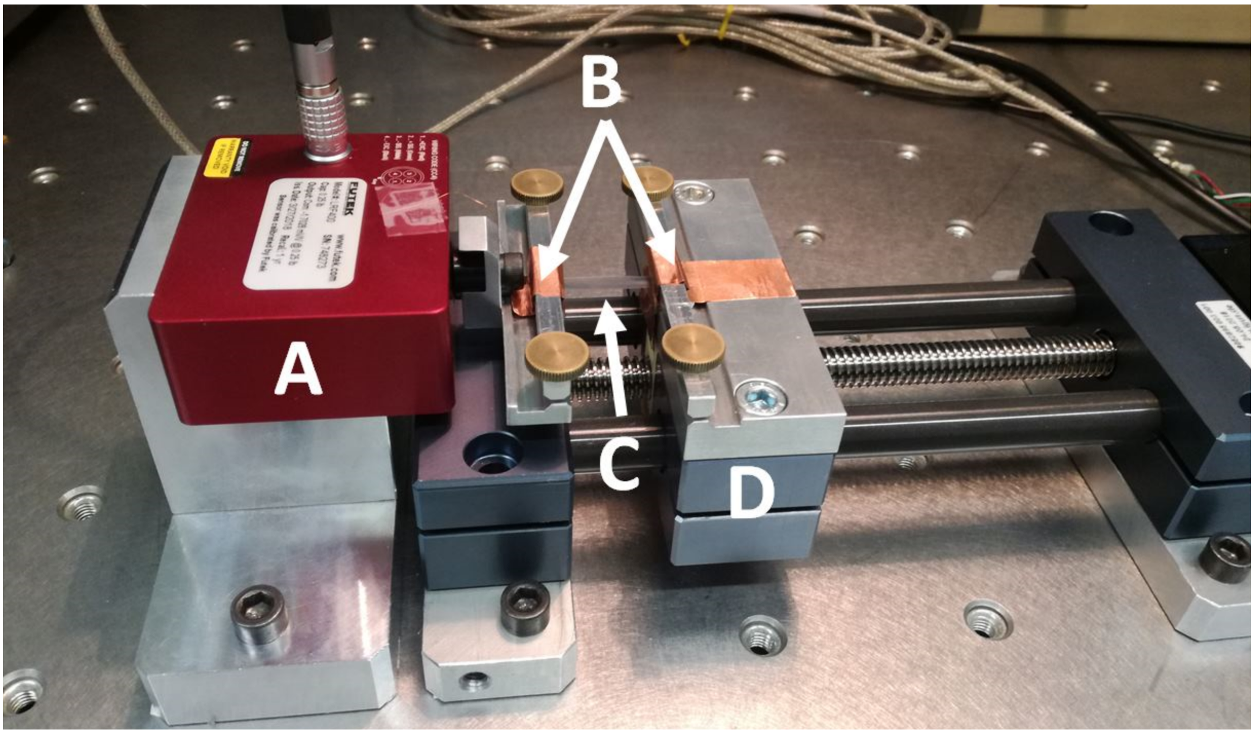

Figure 3.9.: Experimental Stretcher setup, [3], [2]

The sample (C) was mounted between the electrical contacts (B), responsible for the resistance measurements with a source meter (Source Meter 2601B, *Keithley*). Next, different Stretcher cycles were started, testing the sheet resistance in dependence to an applied mechanical stress in form of a strain (ϵ) generated by the stepper motor (NEMA 17 Stepper Motor). The load cell (Load Cell LRF400, *Futek*) (A) measured the force acting on the sample. By imposing a strain the stretchable MA with the attached LIG was pulled apart with a speed v_S. Following Stretcher settings were chosen:

Table 3.7.: Stretcher settings

ϵ / %	v_S / a.u	v_S / mm$\cdot$s^{-1}	Cycles
5	1000	53 ± 1	5
10	1000	53 ± 1	5
20	1000	53 ± 1	5
30	1000	53 ± 1	5
100	1000	53 ± 1	1

For more information see [3].

3.6. Morphology of LIGF samples

In this section the methods as well as the probe preparations for the single methods are introduced.

3.6.1. Production of LIGF samples for observations with an optical microscope

For a first observations of LIGF-IDX sample morphology, depending on different ID settings, an optical microscope (Wild M3B, *Leica*) was used. Distances between single laser lines, their width and the morphology of the LIGF samples, introduced in section 3.5, were evaluated with the optical microscope.

3.6.2. Production of a LIGF cross section for observation with a SEM

To observe the morphology of a LIGF-ID5 sample across their growth direction a cross section had to be produced. For this purpose the PI sheet was attached with the double sided adhesive Scotch-tape to a transparent polymer sheet. Next, a glass substrate was placed on top of the precursor, preventing the laser cutter to transform the subjacent PI into LIG, see figure 3.10.

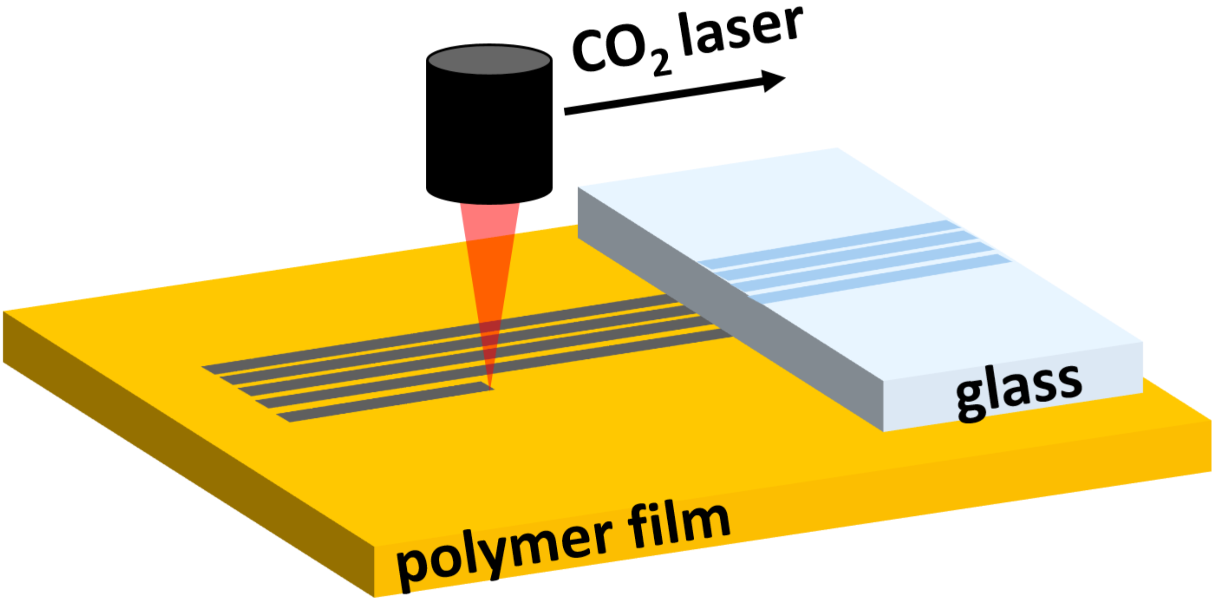

Figure 3.10.: Schematic procedure to create a cross section of a LIGF sample

An engraving process for a LIGF-ID5 sample was started, for settings see table 3.4, and afterwards the glass substrate was removed. The additional PI was cut away with a pair of scissors leaving a cross section of the sample.
The cross section was observed with a SEM (Sigma 300 VP, *Zeiss*), with an acceleration voltage of 5 kV.

3.6.3. Production of a LIG-fibre cross section for observation with a TEM

A (13x12) mm^2 LIGF-ID2 sample, laser settings are found in table 3.4, was produced. Again, the fabrication took place with a PI sheet attached to an additional polymer sheet, as described above. To create the required ultra-thin cuts, needed for an observation with the TEM (Tecnai T12, *ThermoFisher Scientific*), the adhesive Scotch-tape was separated from the sample with a diamond trimmer. Afterward the thin cuts were produced using a 35° ultra-thin diamond knife (hist from *Diatome*) and an ultramicrotome (Leica UC6 from *Leica Microsystems*). As a result to the adhesive residuals only cuts with a thickness around 120 nm were manageable and attached to a formvar coated Cu/Pd grid (75 mesh from *Agar*) for observation.
The TEM acceleration voltage was 120 kV.

3.7. Composition of LIGF samples

LIGF composition was investigated through Raman spectroscopy at FELMI ZFE lab, Graz.

3.7.1. Production of LIGF cross sections for correlative Raman-SEM technique and Raman mapping

Identical to the sample described in section 3.6.3, two different LIGF samples (LIGF-ID2 and LIGF-ID5), were prepared on top of the transparent polymer. After the engraving process the samples were embedded in epoxy resin (SpeziFix 40 from *Struers*) and cut with an ultramicrotome (Leica UC6, *Leica Microsystems*) with a diamond knife (hist, *Diatome*), to create a cross section.

3.7.2. Correlative Raman-SEM technique

For the correlative Raman-SEM technique a Sigma 300 VP from *Zeiss* equipped witch a Raman spectrometer (RISE, *WITec*) was used. The Raman wavelength was 532.26 nm and the SEM acceleration voltage was 1 kV. All the spectra were evaluated with the programs Project FIVE 5.0 and LabSpec 6.
Single Raman spectra, measurement positions were chosen manually - visualized as the red crosses in figure 3.11, were made across the LIG-fibre growth.

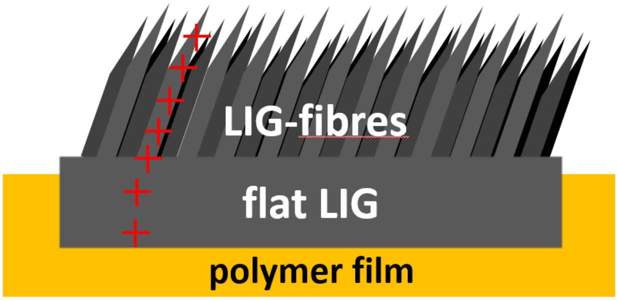

Figure 3.11.: Schematic measurement points for Raman spectra across the LIGF cross section

3.7.3. Raman mapping

A Raman mapping for the LIGF-ID5 sample, for preperation details see section 3.7.1, was made with a Raman spectrometer (LabRAM HR 800, *Horiba Jobin Yvon*), with a wavelength of 532.16 nm. Raman spectra were made with a mapping resolution of 1 µm.

4. Results and Discussion

In this section the laser working principle, the determination of the desired laser processing parameters - to calculate the laser fluence, the LIGF morphology and composition, and the production of conductive material on top of biological precursors are described.

4.1. Influence of process parameters on LIG morphology

4.1.1. Measurement of average laser power

In this section the results of the laser power measurements, made with two different detectors, are discussed and compared. Typical measured trends for the laser power signals can be found in figure 4.1.

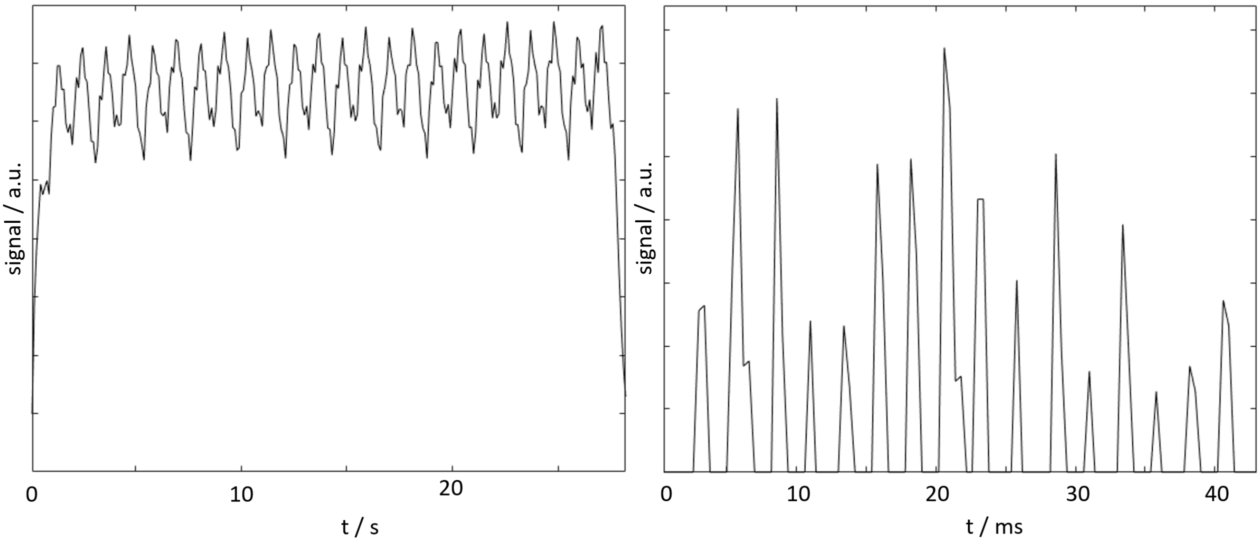

(a) Thermopile sensor (b) Si-Photodetector

Figure 4.1.: Laser power measurements with PPI = 500 and S% = 8 %

Thermopile sensor

By observing the measured data (see figure 4.1 (a)) it soon became clear, that the thermopile sensor was unsuitable to describe the trend of average laser power. The maximal duration of one laser pulse was 0.2 ms, given by the producer (see table 3.2). Thus , the received data did not represent the real laser output, since the detected peaks seen in figure 4.1 (a) are at a total different time scale (s instead of ms).
As described in section 3.4.1, a laser scribing process of e.g. a (5x5) mm^2 square with ID5 and PPI = 500 was detected. In table 4.3 the number of laser lines per cm for different ID settings are listed. Hence, it is impossible that the number of peaks seen in figure 4.1 (a) correspond to the number of laser linese, which should be around 100 lines for the (5x5) mm^2 square.
For this reasons, a prediction of the development of P$_{av}$ with different laser processing parameters was impossible, since it is not straight forward what the detected signal represents.

Neither the number of laser pulses nor the number of laser lines were assignable to the observed detector signal.

Si-Photodetector

This detector was incapable of directly detecting the laser light. Therefore it was used to detect the plasma generated by lasering over an Al-plate. Thus, an indirect measurement procedure was applied and again, no statement about P_{av} was possible.
Nevertheless, the Si-Photodetector was used to obtain single laser spots, since it is capable to resolve signals in the ms-timescale. A measurement, with settings described in section 3.4.1, made with the Si-Photodetector can be seen in figure 4.1(b). Unfortunately, the given pulse duration (after producer) of maximal 0.2 ms was not detectable. This was traced back to the fact that an indirect measurement was made. The peaks seen in figure 4.1(b) are equally spaced, at around 2.8 ms, and were referred to single laser spots.
The time distance between the single laser spots was referred to a combination of PPI and S% setting. An increase in PPI at constant S% leads to smaller time differences between the laser spots, since the laser beam has to produce more spots in the same time. If the PPI setting is held constant but S% increases, the laser beam can spend less time per laser spot. Moreover, this realization led to the assumption that the PPI-setting sets a number of laser spots, with a duration time prescribed by a combination of PPI and S% setting, which can consist of one ore more laser pulses, with a time duration prescribed by the P% setting. Hence, the idea of two different duty cycles describing the working principle of the laser cutter was introduced. For a better understanding a schematic image of the two duty cycles can be seen in figure 4.2 (given values of PPI and S% are exemplary).

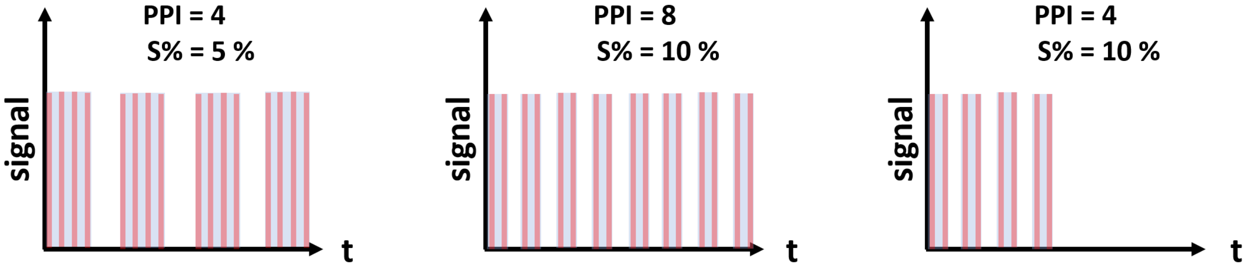

Figure 4.2.: Schematics of the two laser duty cycles, red for the power-dc and blue for the PPI/S-dc

One of the duty cycles is set by choosing a power setting P% (see section 2.2) and describes the duration of single laser pulses during the time the laser is on, with a maximal pulse duration of 0.2 ms. This duty cycle was called power-dc and is visualized with the red areas seen in figure 4.2, referred to the time the laser is on (duration of one laser pulse, here with P% = 50 %).
The other one determines the moments the laser starts and stops working by a combination of PPI and S% settings, since the laser engraver has to produce a prescribed number of points per inch (given by the PPI-setting) in a specific time (given by S%). This duty cycle was called PPI/S-dc and is visualized with the blue areas seen in figure 4.2, referred to the time the laser is activated (duration of one laser spot).

Unfortunately no suitable detector for measuring the real average laser power was available. Thus the average power used to get the laser fluence was calculated by means of the producers specifications found in table 3.2 and equation (2.1).

4.1.2. Measurement of laser line distance in raster mode

For the calculation of processing speed as well as to describe the influence of the Image Density (ID) setting on the resistance in raster mode the number of scribed lines per cm (in vertical direction) were needed. Therefore, different samples scribed with increasing ID-setting from ID1 to ID5 were produced and investigated with an optical microscope.

On PI

It was found that the spacing between neighbouring scribed lines (S_{AB} and S_{BA}) were not equidistant, as seen in figure 4.3. The spacing between two consecutive lines scribed from right to left (S_A) and between the corresponding ones scribed from left to right (S_B) were equidistant: $S_A = S_B$ for each ID value.

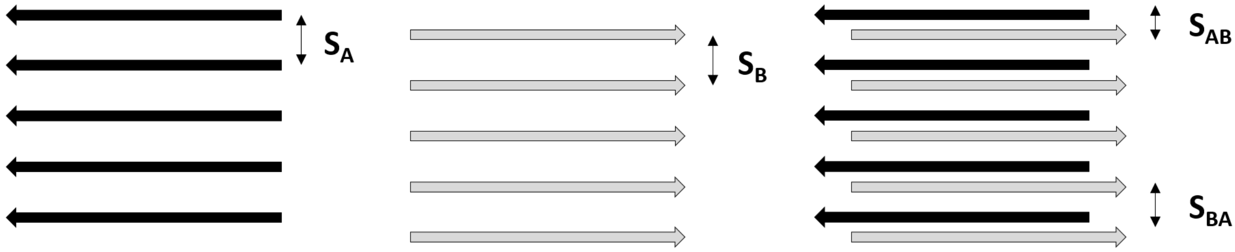

Figure 4.3.: Schematic figure of distances among scribed lines: S_A and S_B for distances between lines scribed in the samen direction, S_{AB} and S_{BA} for distances between neighboured lines

The actual values of S_A and S_B varied with the ID-setting, see table 4.1.

Table 4.1.: Distance measurements on PI between scribed lines for ID1 to ID4

	ID1	**ID2**	**ID3**	**ID4**
$\mathbf{S}_A$ / µm	610 ± 13	243 ± 9	203 ± 8	155 ± 12
$\mathbf{S}_B$ / µm	609 ± 14	250 ± 7	203 ± 7	155 ± 4
$\mathbf{S}_{AB}$ / µm	290 ± 6	123 ± 7	93 ± 11	67 ± 6
$\mathbf{S}_{BA}$ / µm	322 ± 9	126 ± 10	102 ± 6	85 ± 6

Nevertheless, the two grids, created by S_A and S_B, were shifted against each other in vertical direction which led to an alternation of smaller (S_{AB}) and bigger distances (S_{BA}) between two neighbouring lines scribed in raster mode. Further, a shift not only in vertical direction but also in horizontal direction between the two grids appeared (visible in section 4.1.2 on the left side).
Indeed, in raster mode the ID is a setting referred to different numbers of scribed lines per vertical inch area. Hence, low ID values have a bad vertical resolution (small number of scribed lines per vertical inch area) and high ID settings show an increase of scribed lines per inch, leading to a smaller distances between neigbouring scribed lines, compared to low

ID setting. For a better understanding a sample prepared in rater mode with ID1 can be seen in on the left side of section 4.1.2 and one with ID4 on the right side.

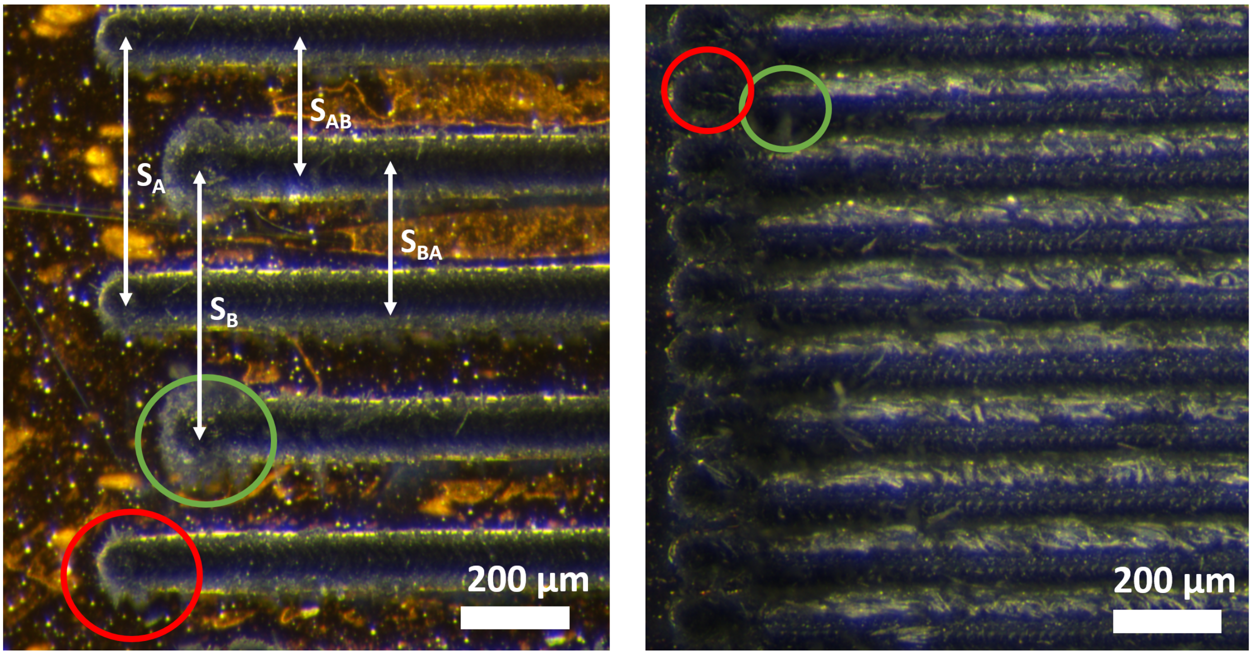

Figure 4.4.: ID1 (left) and ID4 (right) samples - optical microscopy: green circles mark the beginning, and re circles the end of a scribed line

The scribed lines with ID1, seen in section 4.1.2 on the left side, can be clearly distinguished. The starting (marked with a green circle) and the ending (marked with a red circle) of each single line can be differentiated by their unequal shape. The starting looked like a globule while the ending had an identical shape to the rest of the lines. Further, the horizontal shift between the two grids (S$_A$ and S$_B$) is nicely recognizable (horizontal distance between starting and ending of neighbouring lines).
By increasing the ID setting the laser lines were approaching each other and also started to overlap, which can be seen on the right side of section 4.1.2 with ID4. The overlap of the neighbouring scribed lines led to an aggravation in line distance measurements, since it was not possible to clearly distinguish between them.

On MA

After the transfer of the LIGF-IDX samples, from the PI to the MA, the distances between the scribed lines were measured again, found in table 4.2.

Table 4.2.: Distance measurements on MA between scribed lines for ID1 to ID4

	ID1	**ID2**	**ID3**	**ID4**
S$_A$ / µm	610 ± 12	253 ± 6	198 ± 13	153 ± 7
S$_B$ / µm	611 ± 11	254 ± 5	197 ± 7	151 ± 6
S$_{AB}$ / µm	300 ± 8	125 ± 5	98 ± 9	67 ± 3
S$_{BA}$ / µm	305 ± 8	130 ± 10	128 ± 8	90 ± 8

Due to the fact that the overlap of laser lines increases with the ID setting, the accurate distances for ID $\geq$ ID4 were not measurable. Nevertheless the results for the distance measurements on PI and MA were corresponding, as expected. Indeed, the vertical transfer process is not affecting much the in-plane arrangement of scribed patterns.
In table 4.3 the number of scribed lines per cm and their calculated average distance d_{av} (i.e. averaged among S_A, S_B, S_{AB}, S_{BA}) for ID1 to ID5 compared to the specifications of the equipment.

Table 4.3.: Comparison of scribed line distance and number of scribed lines per vertical cm area in raster mode

	VLS 2.30 manual		**Experimental**	
	lines per cm	d_{av} / µm	lines per cm	d_{av} / µm
ID1	-	-	33 ± 1	306 ± 4
ID2	14	706	79 ± 1	125 ± 2
ID3	18	564	99 ± 4	102 ± 5
ID4	24	423	132 ± 5	76 ± 2
ID5	36	282	197 ± 5	51 ± 2

One can see that the specifications given by the producer and the observed number of laser lines per cm were not alike. Hence, for further calculations (e.g. see section 4.1.3) the measured data were used.

4.1.3. Measurement of processing speed

For different pairs of pattern lengths (l) and speed settings (S%) the processing time (t_p) and the laser carriage movement (x) were measured. All the measurements can be found in appendix A.1.

Raster mode

As mentioned before the width of the pattern in raster was w = 10 mm and ID5 was chosen. For speed calculations the number of scribed lines was needed, taken from table 4.3, which turned out to be 197 ± 5.
With this information the processing speed was calculated for samples located in the upper left corner and in the centre of the engraving table, illustrated in figure 4.5.

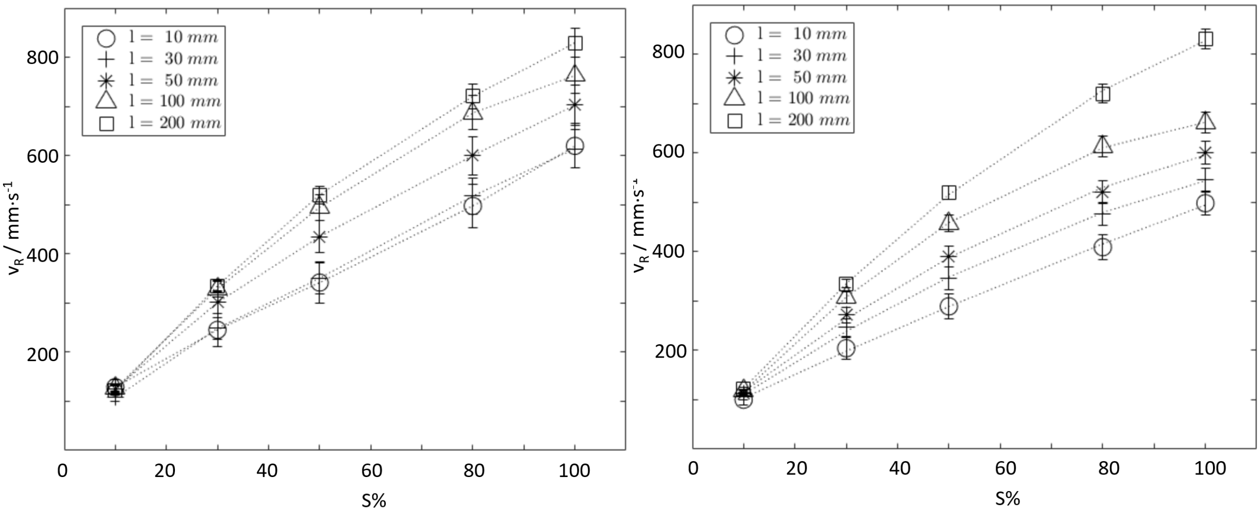

(a) Upper left corner of engraving table

(b) Centre of engraving table

Figure 4.5.: Processing speed in raster mode v_R

Although a linear increase of processing speed v_R with S% was expected, the measured data revealed a deviation from the linearity, see figure 4.5 (b). A possible explanation for the non-linear trend of v_R is the fact, that with increasing S%-setting the acceleration and deceleration process for every single scribed laser line caused an increase in laser carriage movement x, see figure 3.4 and table A.5. It was assumed, that the interplay between S% and x was not perfectly tuned for the laser carriage movement, leading to a deviation of the linear increase of processing speed with S%. This effect was also observed for processing speed measurements made in the upper left corner of the engraving table (see figure 4.5 (a)). A comparison between the v_R-trends for patterns located in the upper left corner of the engraving table (figure 4.5 (a)) and in the middle (figure 4.5 (b)) showed, that the v_R-development for different pattern lengths l was more consistent in the middle of the engraving table. Since the laser carriage has no or less space for acceleration and deceleration processes on the left side of the pattern, in case the engraving takes place in the upper left corner, the v_R-development appeared not as regular as the one observed in the centre of the engraving table. Hence, it was recommended to scribe patterns in the middle of the engraving table. Results for samples located in the centre of the engraving table can be found in table 4.4.

Table 4.4.: Processing speed in raster mode v_R (estimation for patterns located in the centre of the engraving table)

	v_R / mm·s^{-1}				
l / mm	**S% = 10**	**S% = 30**	**S% = 50**	**S% = 80**	**S% = 100**
10	100 ± 10	204 ± 8	289 ± 9	409 ± 9	500 ± 10
30	110 ± 10	247 ± 9	345 ± 9	476 ± 9	550 ± 10
50	110 ± 14	270 ± 12	390 ± 12	520 ± 12	600 ± 14
100	118 ± 3	308 ± 3	457 ± 3	613 ± 3	661 ± 3
200	122 ± 8	335 ± 7	520 ± 7	720 ± 7	830 ± 8

For further calculations, see section 4.2, the trend from figure 4.5 (b) was used, see also table 4.4. To get the processing speed for an arbitrary set of l and S% parameters, the v_R- trends were fitted with a square function (see figure 4.5 (b) and table A.7). Hence, a

calculation of v_R for every S% setting was possible. Since only 5 different trends for various l were made, the rule of three was used to calculate v for random l values. The same principle was used for error calculations.
The v_R approximation of pattern sizes $l \leq 10\,\text{mm}$ was not explicitly tested. Hence, the v_R values received by the fitted v_R-trend are to be used with caution.

Vector mode

In vector mode the processing time t_p for only one single laser line with length l was recorded, found in table A.1 - for a sample located in the left upper corner, and in table A.2 - located in the centre of the engraving table.
The results for the processing speed v_V were plotted in figure 4.6.

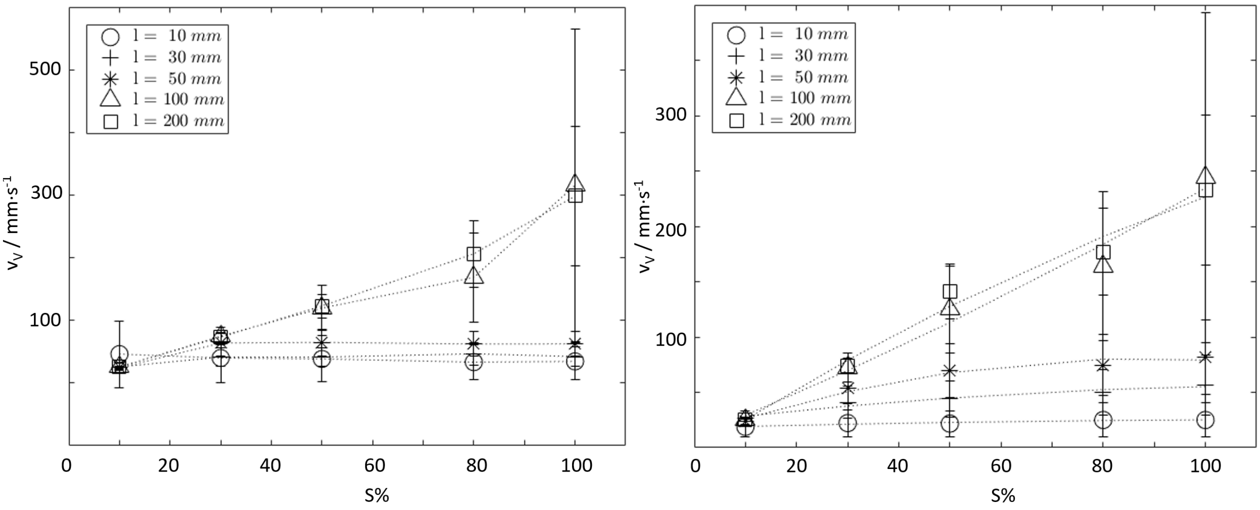

(a) Upper left corner of engraving table

(b) Centre of engraving table

Figure 4.6.: Processing speed in vector mode v_V

Again, as discussed above, no linear increase of v_V with S% was found. Also the statement made according to the different placements of the pattern on the engraving table were observed: v_V-trends for different pattern lengths l located in the middle of the engraving table were more consistent compared to the one in the upper left corner. Hence, for further calculations the results for patterns located in the middle of the engraving table, see table 4.5, were used, as similarly described for the raster mode. Results for the quadratic fit parameters can be found in table A.6.

Table 4.5.: Processing speed in vector mode v_V (estimation for patterns located in the centre of the engraving table)

	v_V / mm·s^{-1}				
l / mm	**S% = 10**	**S% = 30**	**S% = 50**	**S% = 80**	**S% = 100**
10	19 ± 9	22 ± 12	22 ± 12	25 ± 15	25 ± 15
30	27 ± 6	41 ± 14	44 ± 16	50 ± 20	57 ± 27
50	24 ± 3	54 ± 14	69 ± 24	75 ± 28	82 ± 34
100	25 ± 2	70 ± 13	130 ± 40	160 ± 70	245 ± 150
200	25 ± 1	75 ± 10	140 ± 25	180 ± 40	230 ± 70

Since the processing time t_p of only one scribed line was measured in vector mode an accurate determination of t_p was impeded. In particular, the measurements of t_p for a combination of small pattern sizes l with a high S% setting were challenging (very small t_p). Hence, the error bars seen in figure 4.6 are very high compared to the corresponding v_V-values, because t_p and Δt_p, which was the error estimated for the time measurement, were in the same range (see table A.1 and table A.2).

By comparing the processing speed results for raster v_R and vector mode v_V the predetermined difference of around $v_R = 2 \cdot v_V$, given by the producer, turned out to be even higher. [21]
At maximum speed a difference of approximately $v_R = 3 \cdot v_V$ was found. This significant difference in processing speed between the two scribing modes had to be taken into account for the fluence calculations since same S%-settings result to differing v values, in general $v_R > v_V$, causing a difference in fluence values and LIG morphologies.

4.1.4. Measurement of laser spot size

In figure 4.7 one can see single laser-scribed spots created in vector mode. Every row of points was scribed with a different defocus Z.

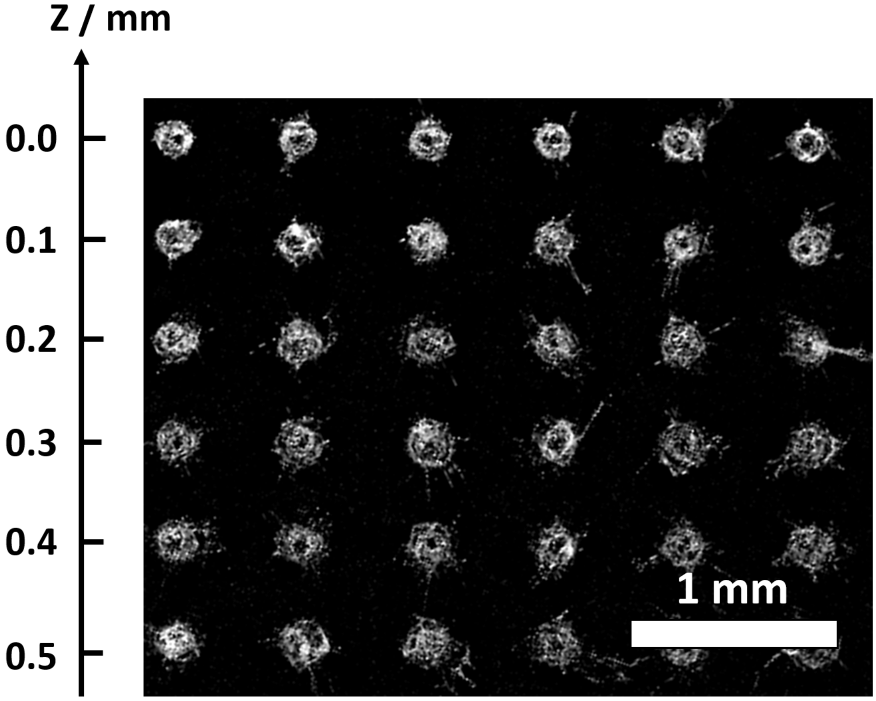

Figure 4.7.: SEM imaging and overview of sample used for spot size measurements at varying Z (defocus)

For each Z-setting at least three different laser spots were investigated. A circular shape was assumed, therefore the diameter (i.e. circle inscribed in a square with sides X and Y, see figure 4.8) were obtained and the mean value was used for further calculations, see figure 4.8.

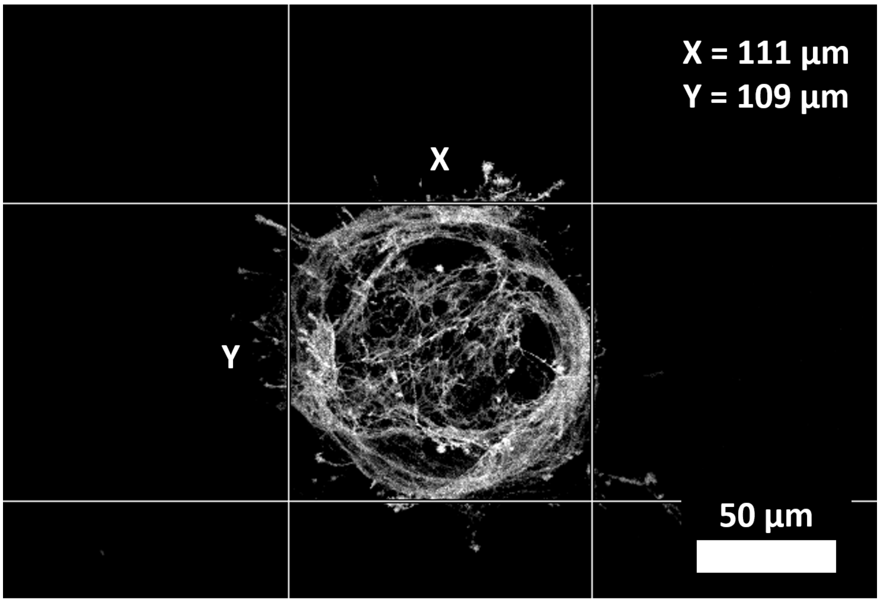

Figure 4.8.: Laser spot diameter measurement procedure with Z = $-0.5\,\mathrm{mm}$

Since the laser induced pyrolysis is a phototermal and photochemical transformation, there is a difference between the theoretical laser spot diamter d_{theo}, calculated after Gaussian beam theory (see section 2.3), and the scribed (or damaged) spot diameter d_{SEM}, which was observed with a SEM, see figure 4.9.

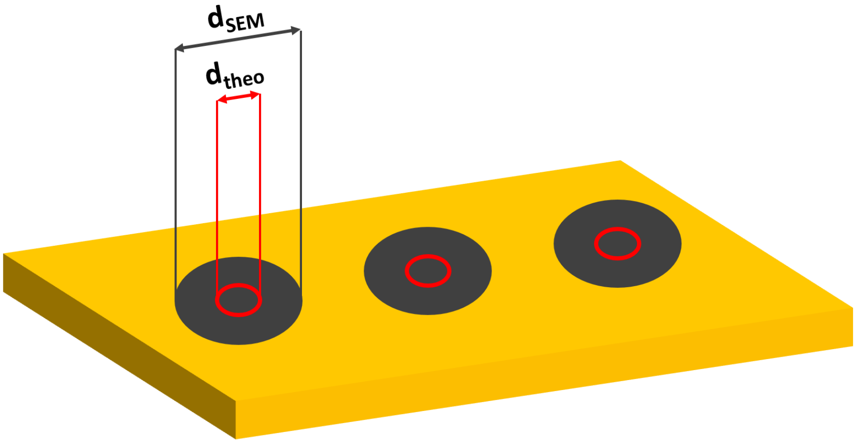

Figure 4.9.: Comparison between the theoretical spot diamter d_{theo}, visualized as the red circle, and the scribed spot diameter d_{SEM}, visualized as the grey area.

For the fluence calculation the spot size is needed, calculated after equation (2.4), with the radii (r_{theo}) or diameter (d_{theo}) of the theoretical laser beam size. Results for d_{theo} compared to the scribed spot diameter (d_{SEM}), observed with a SEM, can be found in table 4.6, with their standard deviation. A trend for the according radii r_{SEM} at different Z-settings are displayed in figure 4.10 (a).

Table 4.6.: Diameter of theoretical d_{theo} and scribed spot d_{SEM} size

Z / mm	$\mathbf{d}_{theo}$ / µm	$\mathbf{d}_{SEM}$ / µm
-1.1	73 ± 3	29 ± 7
-1.0	67 ± 3	55 ± 3
-0.9	60 ± 3	79 ± 1
-0.8	53 ± 3	85 ± 2
-0.7	47 ± 3	99 ± 4
-0.6	40 ± 3	114 ± 3
-0.6	40 ± 3	109 ± 1
-0.5	33 ± 3	113 ± 4
-0.4	30 ± 2	126 ± 2
-0.3	28 ± 1	138 ± 4
-0.2	27 ± 1	154 ± 8
-0.1	26 ± 0	145 ± 2
0.0	25 ± 0	141 ± 8
0.1	26 ± 0	153 ± 14
0.2	27 ± 1	153 ± 6
0.3	28 ± 1	145 ± 3
0.4	30 ± 2	136 ± 6
0.5	33 ± 3	117 ± 2
0.6	40 ± 3	108 ± 7
0.7	47 ± 3	90 ± 1
0.8	53 ± 3	80 ± 3
0.9	60 ± 3	57 ± 6

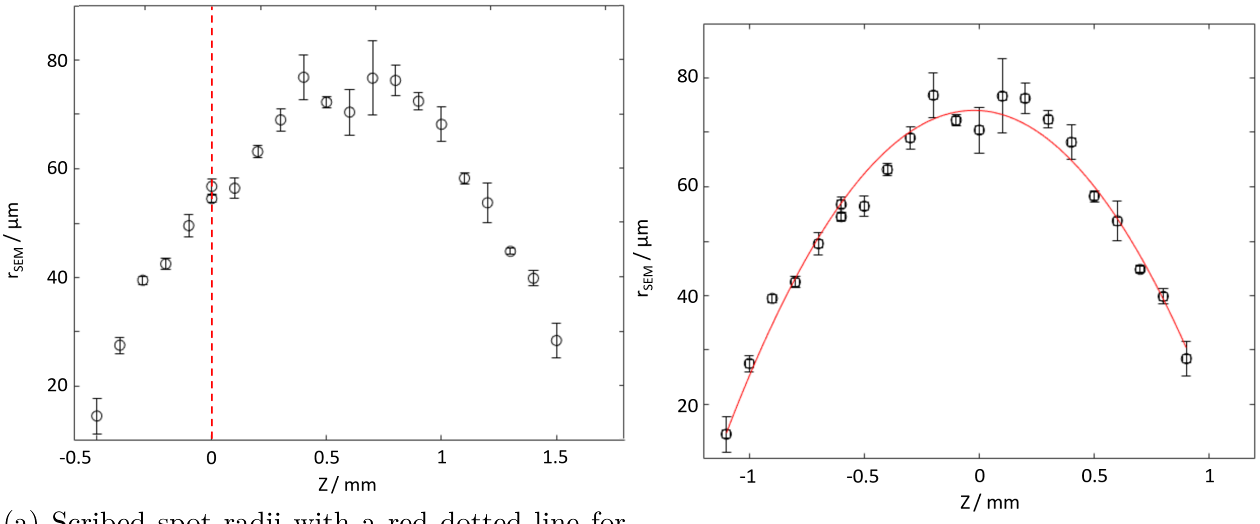

(a) Scribed spot radii with a red dotted line for Z = 0 mm

(b) Gaussian fit for the shifted scribed spot radii

Figure 4.10.: Measurement results for the scribed spot radii

Assuming a symmetrical change for the laser spot size around the focal position (Z = 0 mm) it turned out that the engraving table was 0.6 mm out of focus - visualized by a red dotted line representing the focal position in figure 4.10 (a). Therefore the results were shifted, which can be seen in figure 4.10 (b). Hence, all the following information regarding the defocus Z already contains the mentioned shift: former position Z $= -0.6$ mm was set equal to Z $= 0$ mm. Further, the change in spot radii r_{SEM} with table height Z followed a Gaussian fit, for the fit parameters see appendix A.3.

In contrast to the theoretical course the scribed spot size seemed to decrease with increasing defocus. Further, in focal position a laser spot diameter of $d_{theo} = 25$ µm was given by the producer (see table 3.2). As it can be seen in table 4.6 the scribed spot diameter at Z $= 0$ mm was $d_{SEM} = 141$ µm.
This behaviour can be explained by assuming that the d_{SEM} is nothing else than the impact area of the laser and therefore it is a area of damage and not comparable to the the real laser spot diameter d_{theo}, see figure 4.9. By moving the sample out of focus, the energy per area (laser fluence) decreases which leads to a development of a smaller impact area.

As mentioned before, the laser spot size was needed to calculate the laser fluence. In literature ([12]) the scribed spot size (damaged area) is often used to this purpose. However, the use of this assumption is criticized, since it causes an overestimation of the (actual) laser beam spot size in focal position; in turn, this cause a corresponding underestimation in further calculations of the fluence H. Vice versa, at (much) defocused conditions the beam spot size is underestimated and fluence H is overestimated. Moreover, this assumption relies on the estimate of damaged area on top of a single, selected material: PI. The observed damaged area can vary much depending on the material used. Therefore, in order to avoid this possible source of errors and avoid confusion, it is more reasonable to use the theoretical laser spot size instead of the scribed damaged area to calculate the fluence, since the impact area further depends on the material.

The theoretical laser spot size was calculated with equation (2.2), equation (2.3) and equation (2.4), see table A.8.

Despite an estimation of the actual damaged area, it was not used in fluence calculation. However, it is anyway a very relevant parameter and provides important information about the scribed LIG. Indeed, it allows for tuning and interpreting LIG-overlapping over neighbouring scribed lines, crucial in establishing continuous conductive pathways in these conductive materials.

4.2. Fluence Calculator

The laser fluence H is defined as the laser optical energy delivered per unit area. Therefore H derives from all the laser cutter parameters. This physical quantity is used to compare experiments and results among research groups using different equipments and settings. Further, the laser fluence can help in comparing the two laser modes (raster and vector). Hence, a Matlab script called the Fluence Calculator was written to enable the calculation of fluence for any given set of scribing parameters for the equipment in use at LAMPSe laboratory.

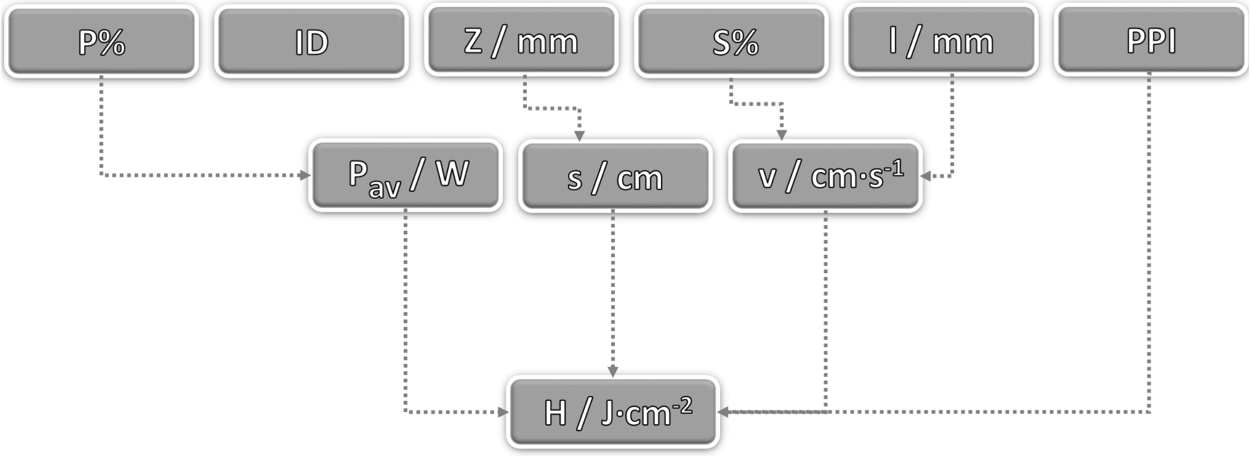

Figure 4.11.: Overview for working principle of the Fluence Calculator

In figure 4.11 the adjustable laser cutter parameters are summarized and how they were used to calculate the required average laser power (P_{av}), the processing speed (v), the theoretical laser spot size (s) and laser fluence (H). The actual equations used for each quantity in Fluence Calculator are equation (2.1) for the average power, the equations found in appendix A.2 for processing speed in raster and vector mode, and equation (2.4) for the theoretical laser spot size.

To predict the impact area of the laser cutter with a specific set of parameters, the fluence values and the observed spot sizes found in table A.8 were compared. A schematic development of impact area, defocus and fluence can be seen in figure 4.12. The plotted red circles refer to the diameter of the expected damaged area (d_{SEM}) of the laser on top of the PI. With this information a fit was made to forecast the impact area generated by the laser cutter, seen in figure A.1.

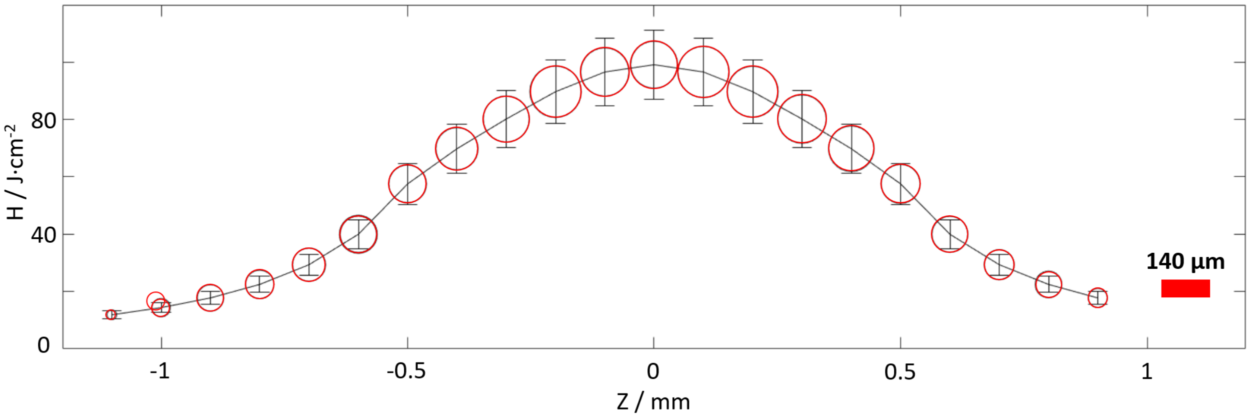

Figure 4.12.: Schematic change of observed spot diameter, visualized as red circles, with defocus (Z) and laser fluence (H)

4.2.1. Testing of the Fluence Calculator

As mentioned in chapter 1 a mapping of LIG-morphologies caused by different laser settings was preliminary made, see figure 1.2. For each single P%-S% configurations the laser fluence H was calculated with the Fluence Calculator, see table A.9 and the results were layered on top of the mapping with a colour code, see figure 4.13. For the calculations the following parameters were chosen:
$Z = 1\,\mathrm{mm}$; $PPI = 500$; $ID = 5$; $l = 10\,\mathrm{mm}$; mode: raster mode, as used in the preliminary experimental observations.

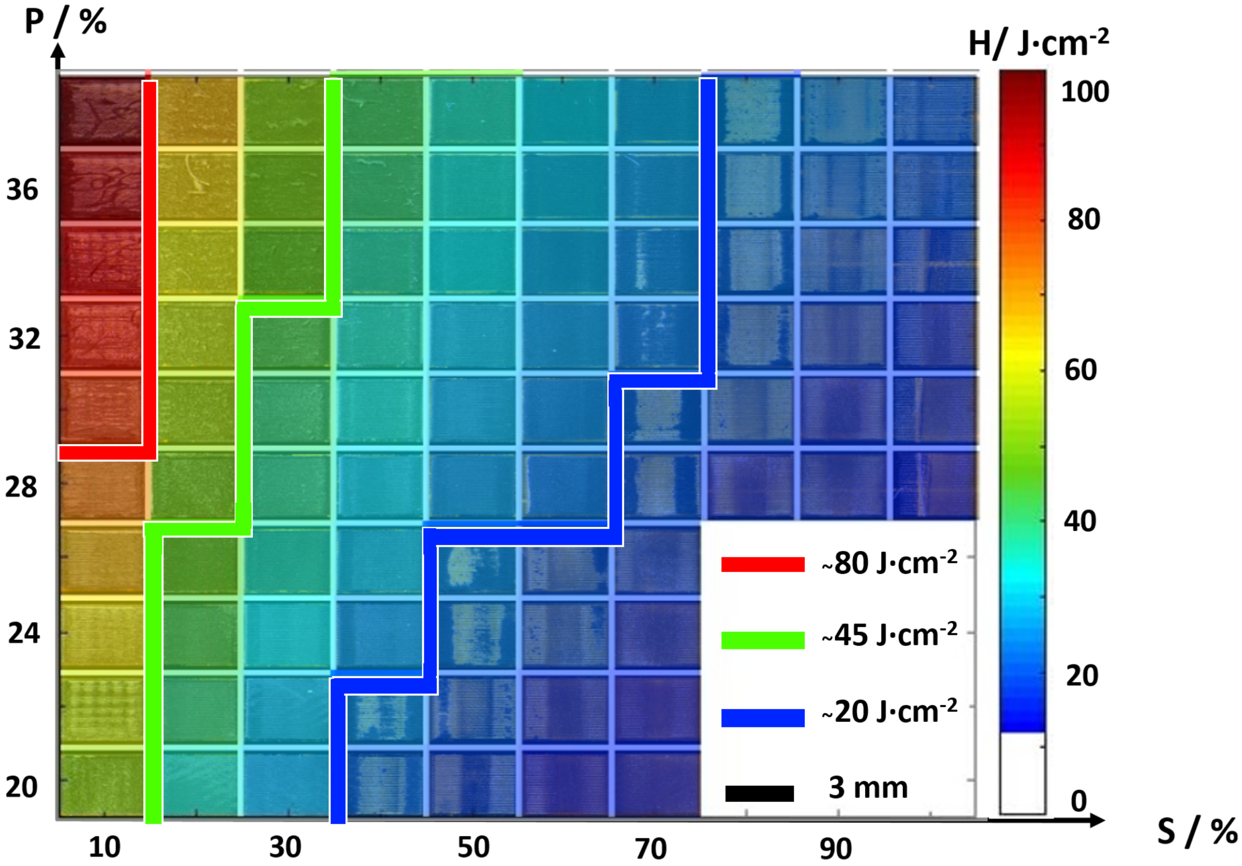

Figure 4.13.: Calculated laser fluence H for the LIG-morphology mapping

The H-trend corresponded very well to the obtained morphology, see figure 4.13. For laser fluence values $H < (20 \pm 2)\ \mathrm{J \cdot cm^{-2}}$ (blue area) no homogeneous LIG formation was found. Flat-LIG was obtained in the range $(20 \pm 2) < H < (45 \pm 5)\ \mathrm{J \cdot cm^{-2}}$ and LIG-fibres for $(45 \pm 5) < H < (80 \pm 8)\ \mathrm{J \cdot cm^{-2}}$ (green area). The red area, referred to the destroyed polymer sheet, lied in the range $H > (80 \pm 8)\ \mathrm{J \cdot cm^{-2}}$.

In order to investigate the influence of the laser fluence to the LIG morphology in more detail, SEM images of scribed spots at varying dafocusing conditions were taken (figure 4.14).

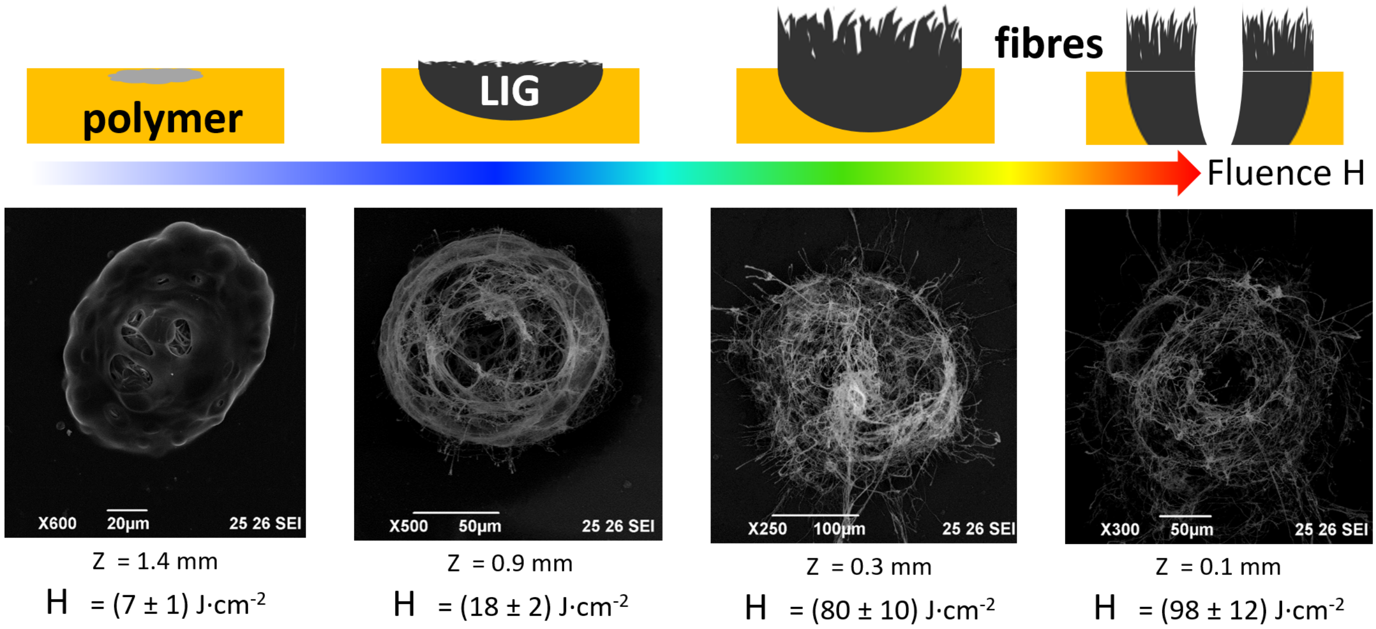

Z = 1.4 mm
H = (7 ± 1) J·cm^{-2}

Z = 0.9 mm
H = (18 ± 2) J·cm^{-2}

Z = 0.3 mm
H = (80 ± 10) J·cm^{-2}

Z = 0.1 mm
H = (98 ± 12) J·cm^{-2}

Figure 4.14.: Relation between laser fluence and LIG morphology

Starting with a low laser fluence the polymer precursor showed a very small impact, mostly melting and probably no or only little carbonisation. By increasing the fluence a nice circular impact area was obtained around $H = 20\ \mathrm{J} \cdot \mathrm{cm}^{-2}$. Here no formation of fibres was observed, thus this morphology was called flat-LIG. According to the mapping seen in figure 4.13 at around $H = 45\ \mathrm{J} \cdot \mathrm{cm}^{-2}$ fibres should start to emerge from the polymer sheet. Such samples had a fibrous morphology like the one seen in figure 4.14 for $H = 80\ \mathrm{J} \cdot \mathrm{cm}^{-2}$. Further increasing of H led to destruction of the precursor leaving behind a burned hole in the middle of the laser spot surrounded by LIG-fibres.

4.2.2. Comparison of the Fluence Calculator with the state of art: Tour group

The combined results of Fluence Calculator and observed morphology of LIG were compared with results available in literature by one of the leading groups in LIG research: Tour group at Rice University (USA). The laser engraver used by the Tour group came from the same provider, namely the ULS, though lasers with different maximum power (10 W, 50 W and 75 W) were used. Apart from power, laser wavelength, pulsed frequency, processing and carriage speed are the same as in our VLS 2.30 system (30 W laser source). Nevertheless they claimed that regardless of the used maximal power the same fluence thresholds for carbonisation were obtained. [1], [12]

Table 4.7.: Comparison between Tour group and Fluence Calculator

	H / J·cm^{-2}	
	Tour group	**Fluence Calculator**
flat-LIG	$\sim$ 5	$\sim$ 20
LIG-fibres	> 40	> 45

In table 4.7 a comparison for the laser fluence values, needed to obtain flat-LIG and LIG-fibres, between the Tour group and the developed Fluence Calculator can be found. In general the Fluence Calculator returns higher H values compared to the ones given by the Tour group. In the following the reasons for this differences will be discussed.

Differences in average laser power determination

Due to the fact that no suitable detector for laser power measurements was available, in this study the average laser power was calculated by equation (2.1) and considering the laser specifications given by the provider (see table 3.2). Tours' group on the other hand used measured trends to determine the average laser power. Hence, in that respect the Fluence Calculator owns a shortcoming in contrast to the fluence calculation of Tour.

Differences in processing speed determination

In literature the processing speed was calculated by assuming a linear trend originating from a maximum laser carriage speed.

However, the speed measurements carried out in this study, for different speed settings and pattern lengths, evidenced that neither a linear decrease nor a uniform maximal processing speed existed. Therefore the Fluence Calculator used a polynomial fit (2nd degree), for different speed setting to pattern length trends, to give more reasonable values for the laser carriage movement. In this respect the estimation of speed and, in turn, of fluence can be regarded as more realistic.

Differences in laser spot size determination

As discussed before the theoretical laser spot size should be used to calculate the fluence instead of the observed impact area of the laser, as done by the Tour group. Thus the Gaussian beam theory, (see section 2.3), was used to this purpose, in combination with the laser specifications given by the provider (see table 3.2). Since the theoretical trend for the laser spot size was used, the calculations were based on the information about the laser spot size in focal position and the focal length provided by the producer.

For this reason the laser spot size- as well as the average power calculation, which were both based on provider information, can be seen as the main source of discrepancy for the Fluence Calculator.

4.3. Morphology of LIGF

In this section the morphology of LIGF-IDX samples are discussed. To investigate the morphology optical and electron (SEM) microscopy were used.

4.3.1. Optical microscopy

LIGF samples on PI

LIGF-IDX samples were prepared in raster mode with different ID-settings (ID1 to ID5). The resulting top view images obtained with an optical microscope can be seen in figure 4.15. The measured scribed line distances can be found in table 4.1. The LIG-fibres were recognizable at the sides of the single scribed lines and LIGF-ID5 samples showed the most dense wood of fibres. No assumptions about fibre length were possible since the images were only made in a top view. A possible explanation for the difference in shape of the ending and the starting of a single laser line (see section 4.1.2) could be, that the laser carriage was moving slower at the beginning of a line compared to the rest of it, which caused a locally higher laser fluence and therefore a bigger impact area of the laser.

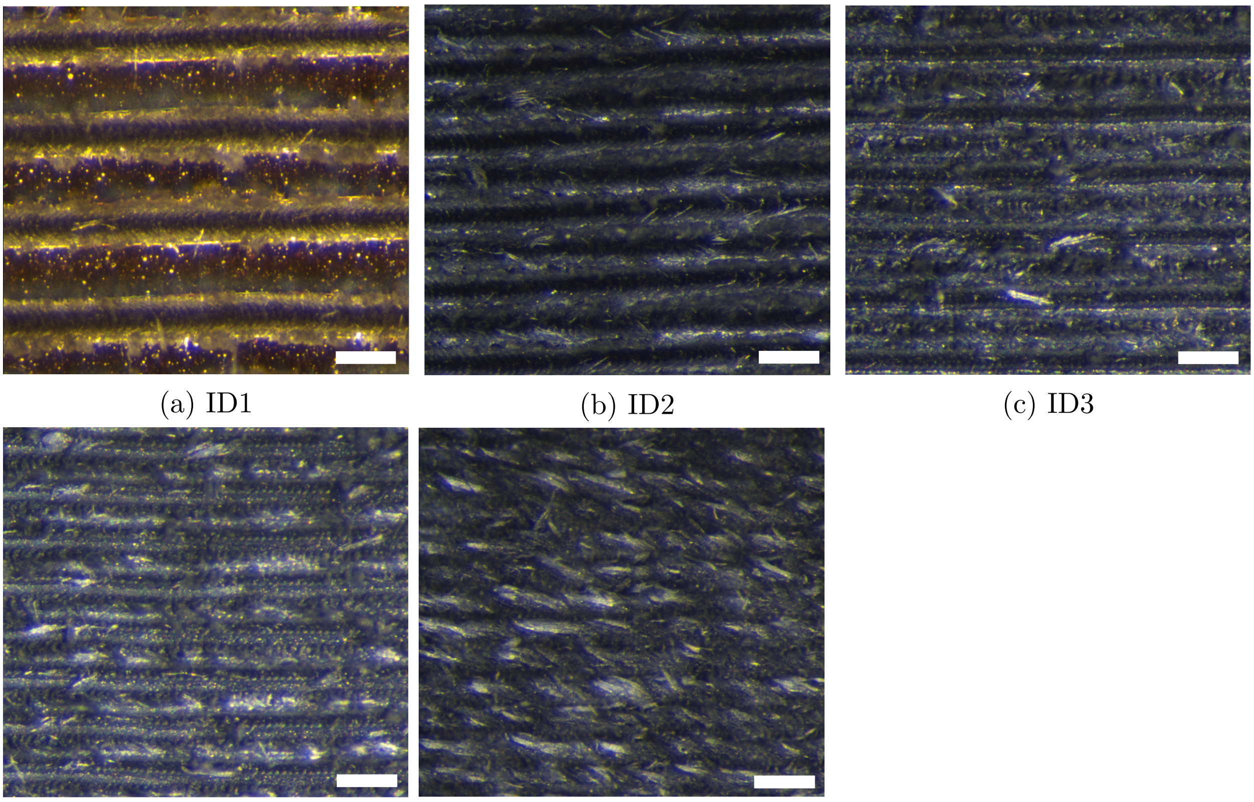

(a) ID1 (b) ID2 (c) ID3

(d) ID4 (e) ID5

Figure 4.15.: Optical microscope images of LIGF-IDX samples on PI; scalebar: 200 µm

LIG-fibres on MA

After the transfer of the produced LIGF-IDX samples on to the MA, the stretchable composite stripes were observed with the optical microscope (figure 4.16). The distance measurements between laser lines can be found in table 4.2 and corresponded with the results of table 4.1 obtained on PI.

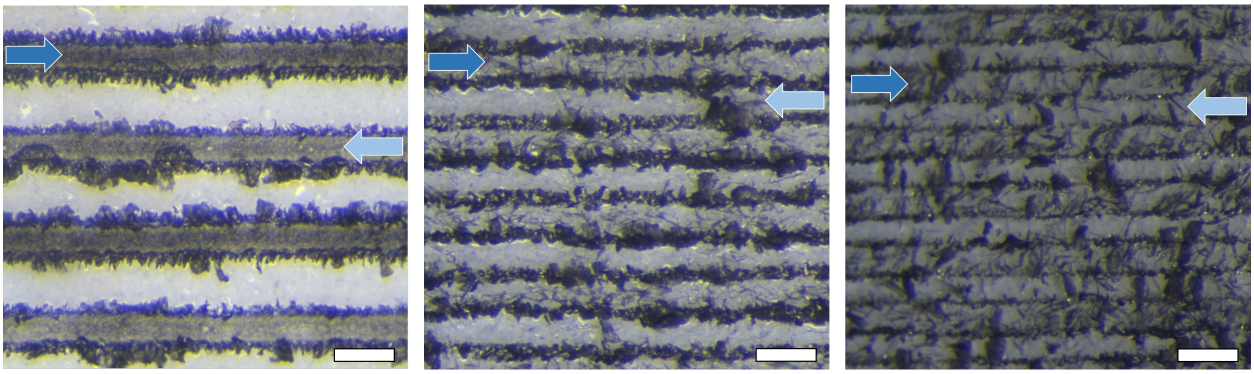

(a) ID1 (b) ID2 (c) ID3

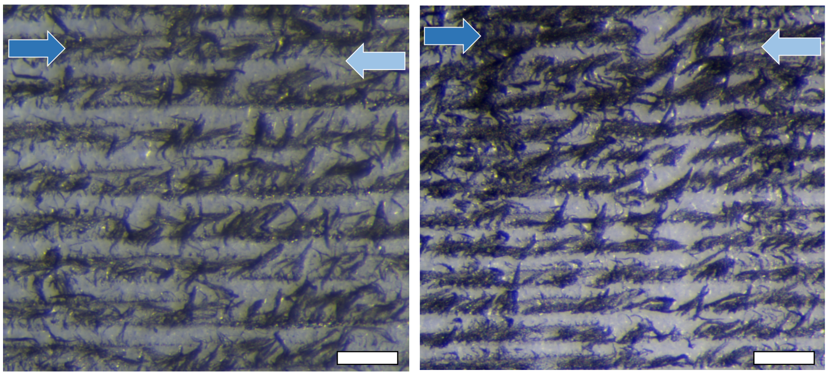

(d) ID4 (e) ID5

Figure 4.16.: Optical microscope images of LIGF-IDX samples on MA; scalebar: 200 µm; Arrows are indicating single scribed lines: dark blue is referred to a scribed line going from left to right and the bright blue one for a line scribed from right to left

In general, the fibres obtained on the MA were found on the sides of laser lines. For a better understanding, the path of scribed lines was highlighted with blue arrows on the sides of figure 4.16. Further, the LIG-fibres grown on top of LIGF-ID1, LIGF-ID2 and LIGF-ID5 samples looked denser compared to the other ones. Hence, the edges of the scribed lines, where the fibres were emerging, looked more densely populated.

In figure 4.17 (a) the scribed lines obtained by an LIGF-ID1 sample on MA can be seen. The observed morphology showed some peculiar features, depending on the direction of laser scribing. An alternation of longer (L , green rectangle) and shorter (S, red rectangle) fibers at opposite sides of each scribed line was observed. This pattern was however inverted at every consecutive line, depending on scribing orientation: lines going from right to left (R-L, bright blue arrow) had longer fibres in upper direction and laser lines going from left to right (L-R, dark blue arrow) in bottom direction. A schematics of these features is displayed in figure 4.17 (b). As a result a pattern of repeating L-S-S-L sequences is produced. Furthermore, this pattern is made more complex by the sequence of different interline distances (described in section 4.1.2).

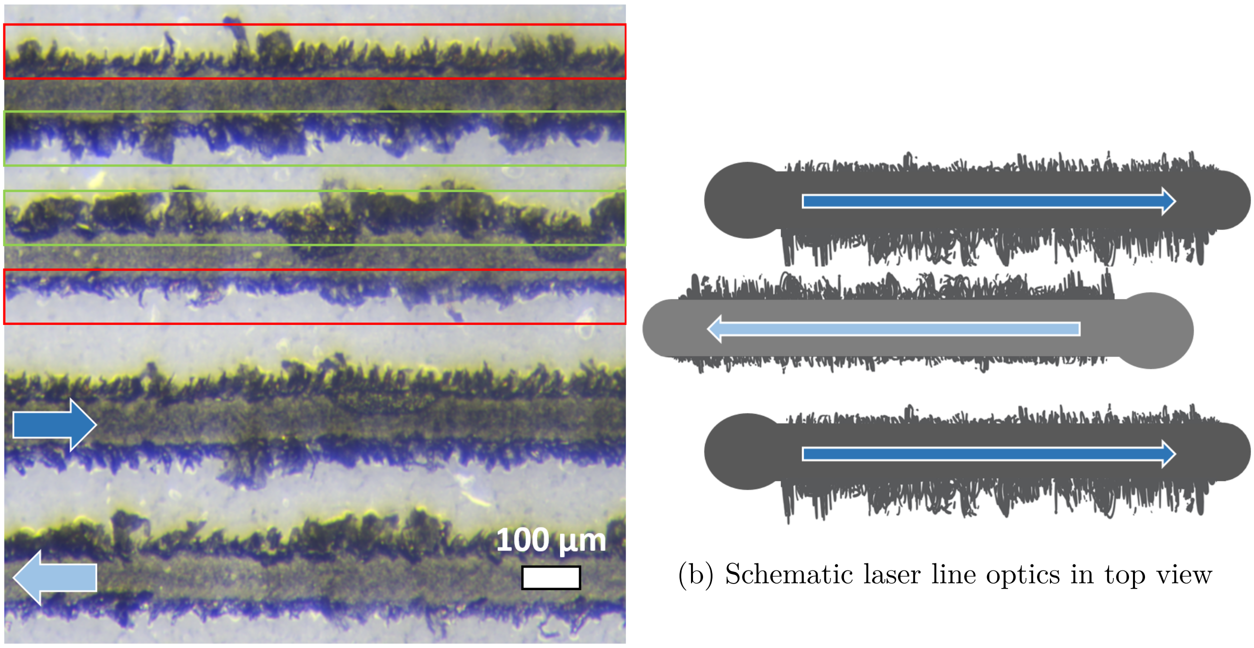

(a) Optical microscope images of an LIGF-ID1 sample on MA

(b) Schematic laser line optics in top view

Figure 4.17.: Morphology of a LIGF-ID1 sample on MA obtained with an optical microscope and schematics; arrow are indicating the single scribed lines and their corresponding laser carriage driving direction; the red and green box are showing the alternating change of LIG fibre lengths on the sides of a single scribed line: red boxes indicate short and green boxes long fibres

Also, a difference in brightness between the laser lines can be seen. As a result the R-L-lines appeared brighter compared to the L-R ones. Again a difference in laser carriage movement was hypothesised as a reasonable explanation. To verify this hypothesis the line width, which is equal to the diametre of the laser impact area (d_{SEM}), should vary due to a difference in laser fluence caused by the unequal processing speed. Hence, measurements of line widths for R-L- and L-R lines were made but no dissimilarities in laser line width was found. Therefore, a second hypothesis was done: the difference in brightness might be caused by the transfer process of LIG onto the MA. Since the stretchable adhesive tape got removed from the sample by peeling off (i.e. unidirectional stress was applied), this procedure could have possibly favoured the removal of grown fibres in one direction than in the other.

4.3.2. SEM

Morphologies of LIGF-IDX samples and the single spots prepared in vector mode with different Z-settings were investigated. The attention was focused on the LIGF-IDX samples, since they were used to produce stretchable conductors. In vector mode the morphology of single laser spots with different laser fluence values were studied (as imaged in figure 4.14) to see a transition of flat-LIG to LIG-fibre morphology.

Raster mode

Two SEM-images, of a LIGF-ID2 sample can be seen in figure 4.18.

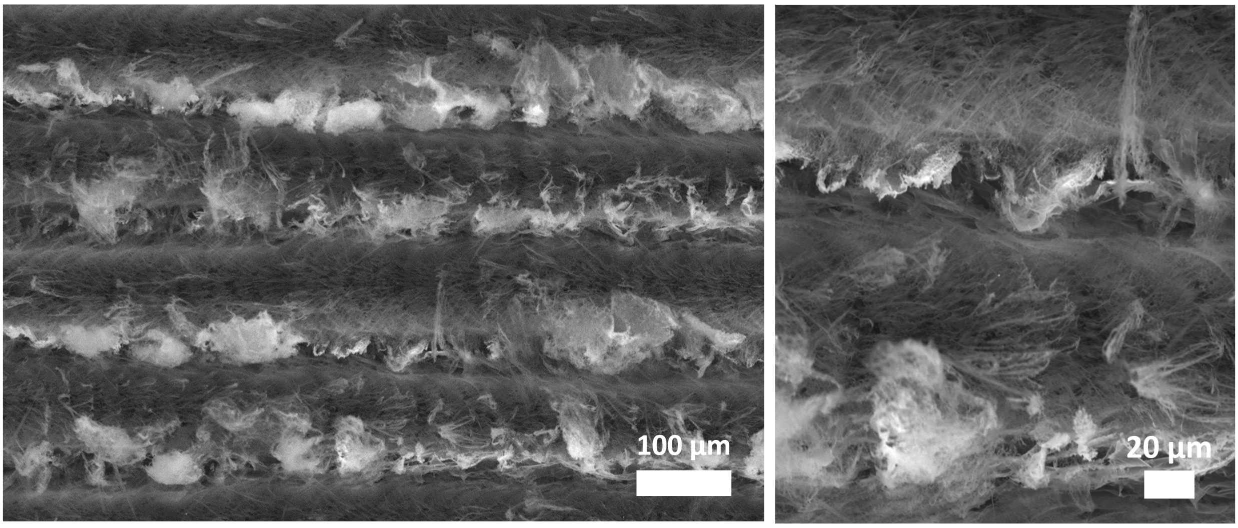

Figure 4.18.: SEM images of a LIGF-ID2 sample in top view

SEM imaging permitted to appreciate that LIG-fibres emerged not only from the sides of the laser lines but also from their middle part. Still, longer fibres grew out at the outside edges. Fibres are arranged radially from the centre of laser spots, which were overlapping each other (see figure 4.19).

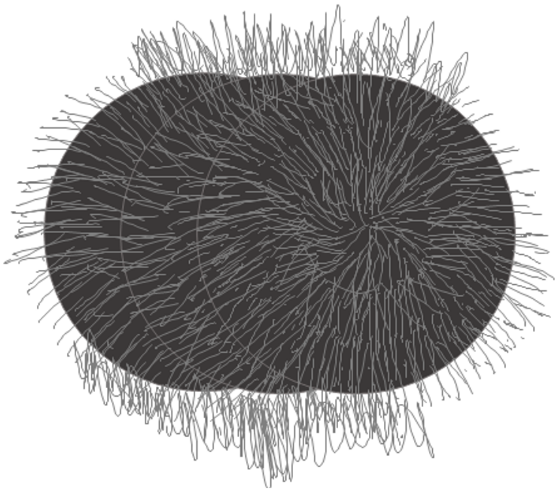

Figure 4.19.: Schematic growth of LIG-fibres

Because of overlapping (and the resulting partial destruction/modification of previously scribed fibers) the favoured fibre growth direction appeared to be the one going in opposite way to the laser carriage movement.

Fibers formed in dense bundles emerging from laser scribed lines, as evidenced a high resolution SEM micrograph (figure 4.20).

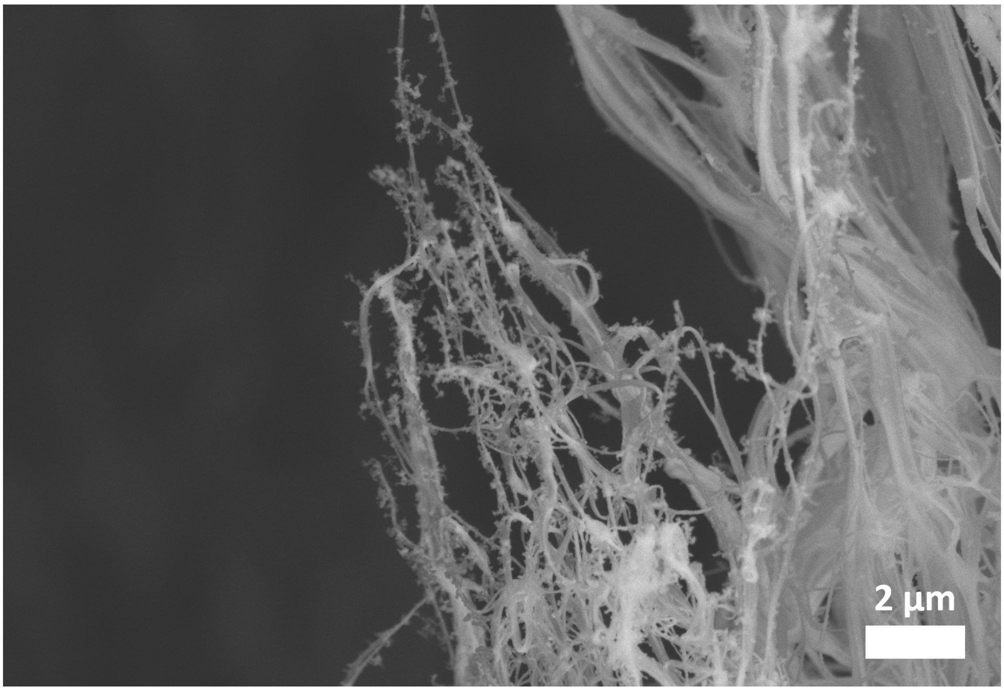

Figure 4.20.: SEM images of LIGF-ID2 sample in top view

Differences in fibre width, shape and length were recognizable. They started to grew out as thick fibres with sharp defined edges and transformed into very thin and branching ones.

In figure 4.21 a top view picture of an LIGF-ID4 sample can be seen. The single laser lines were overlapping and therefore no clear distinction between them was possible. Considering the difference in neighbouring laser line distances (see figure 4.3) and the fact that fibres tend to grow out in opposite direction to laser carriage movement, the longer LIG-fibres seen in figure 4.21 were emerging from lines starting at the left side of this image. Combining this information with the one gathered from figure 4.17, namely that the lines had short fibres emerging from one side and longer ones on the other side, the pattern seen in figure 4.21 could be explained.

Figure 4.22 shows the same sample with a higher magnification. The bundles of fibre were growing out in a straight way starting from a more porous underground and at a specific height they begun to bend over in the contrary engraving direction. Additionally the smaller fibres seen before in the LIGF-ID2 samples, emerging from the centre of the laser line, were missing. This might be caused by the overlap of laser lines or due to perspective reasons.

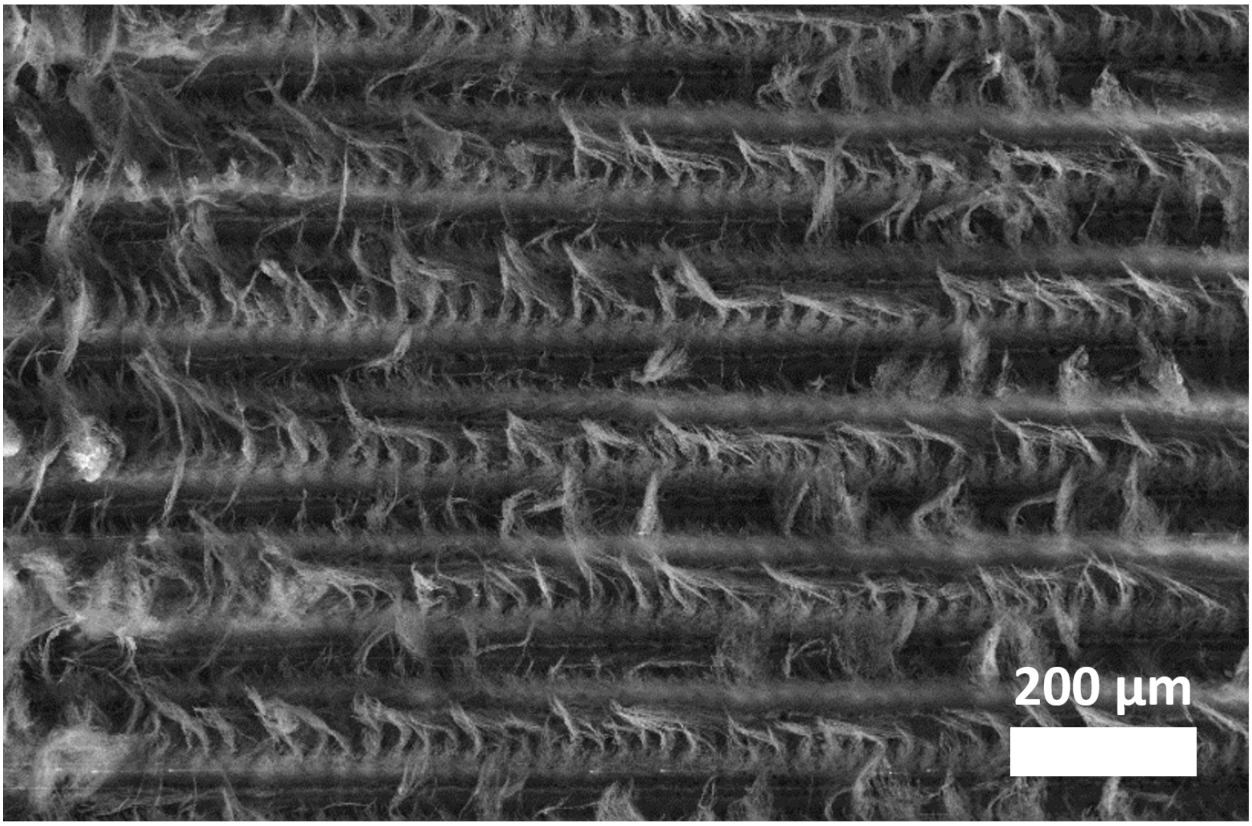

Figure 4.21.: SEM images of an LIGF-ID4 sample in top view

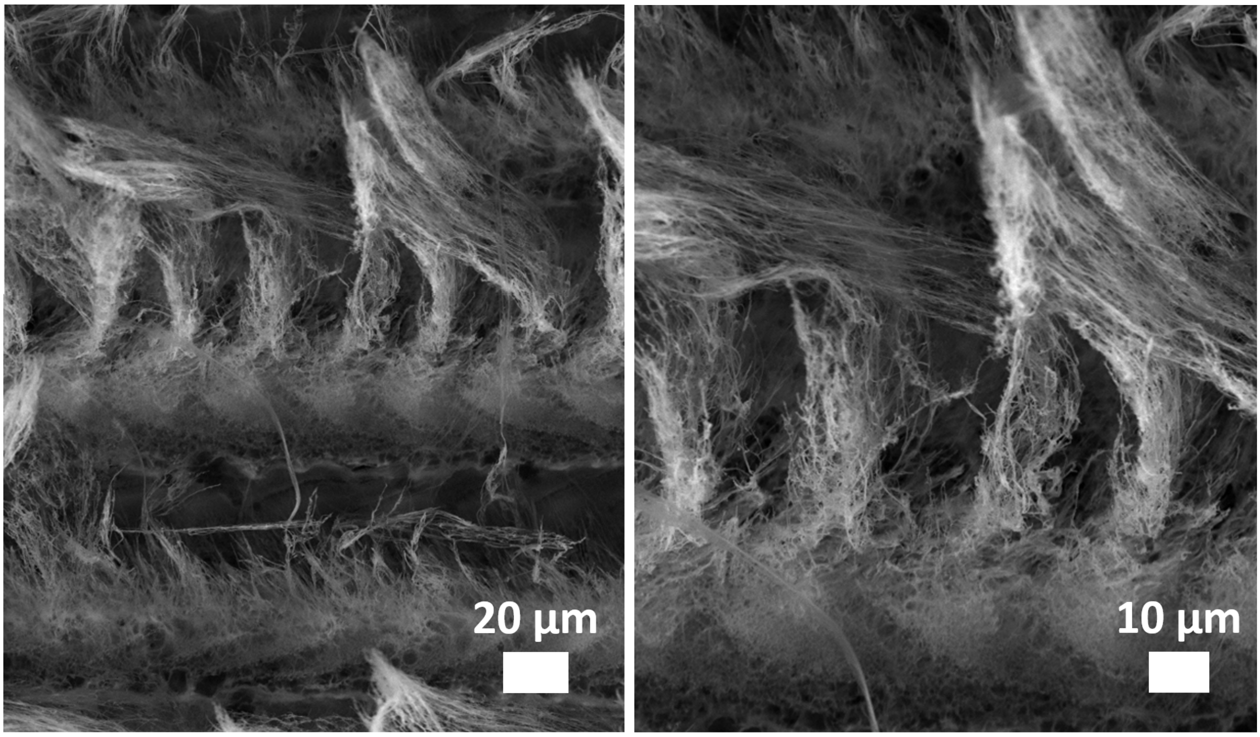

Figure 4.22.: SEM images of LIGF-ID4 fibres in top view

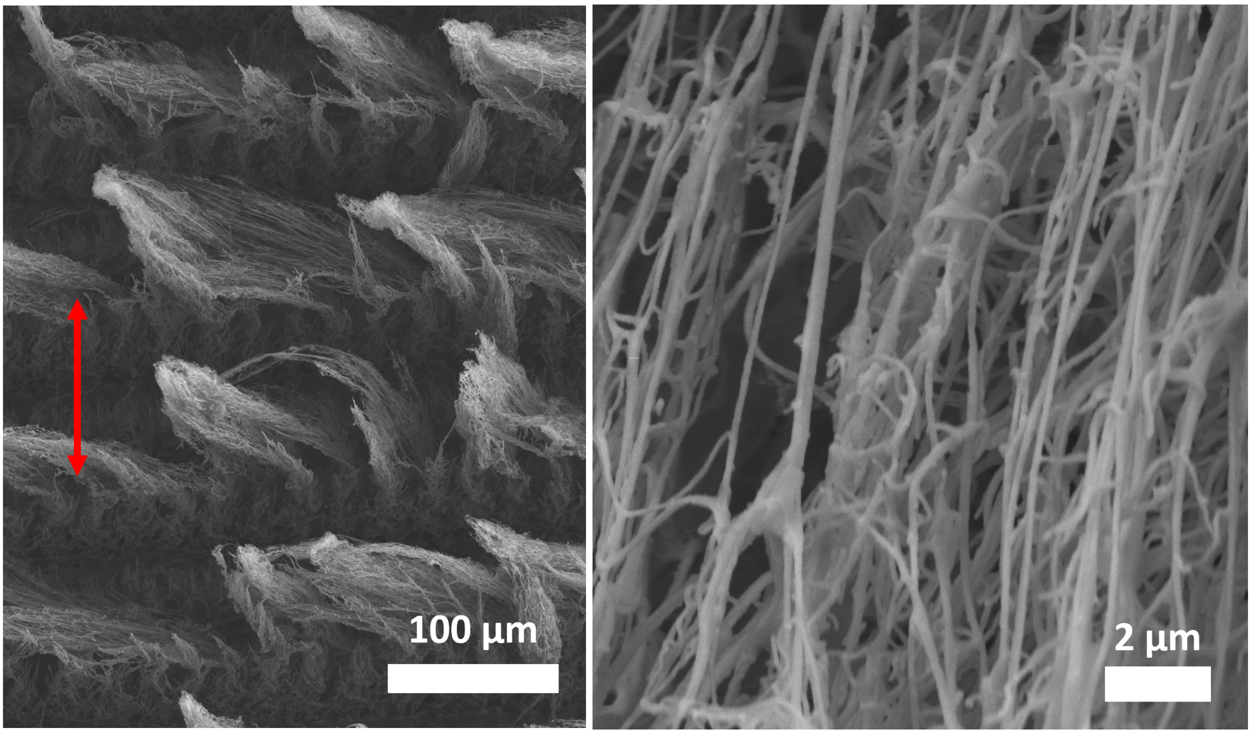

Figure 4.23.: SEM images of LIGF-ID5 fibres in top view; red arrow indicates the distance between to scribed lines in the same laser carriage driving direction

At the left side of figure 4.23 a top view image of an LIGF-ID5 sample can be seen. The average distance between two consecutive scribed lines, at ID5, should be around 50 µm (see table 4.3). Nevertheless, the distance between the long fibres (marked as red arrow) is around 100 µm. Hence, it was assumed that a combination of line overlapping and the in section 4.3.1 observed iteration of long (L) and short (S) fibres of the scribed lines led to this effect. This means that the long fibre trenches seen in figure 4.23 belonged to lines engraved in the same laser carriage driving direction, showing the L-side. Between the L trenches a line scribed in the opposite direction should be located with the S-side, which is covered by the L-sides and therefore not recognizable.
In the right part of figure 4.23 a close up image of the fibres was made. Unlike to the sample produced with an ID2 setting no branching was found and moreover, the fibres appeared denser.

All the SEM imaging described so far was carried out in top view mode. However, cross sectional views of samples were needed for a complete description of their morphology. To permit a reliable observation of thickness and length of single fibres a cross section of an LIG-ID5 sample was prepared, after the procedure sketched in figure 3.10, and can be seen in figure 4.24.

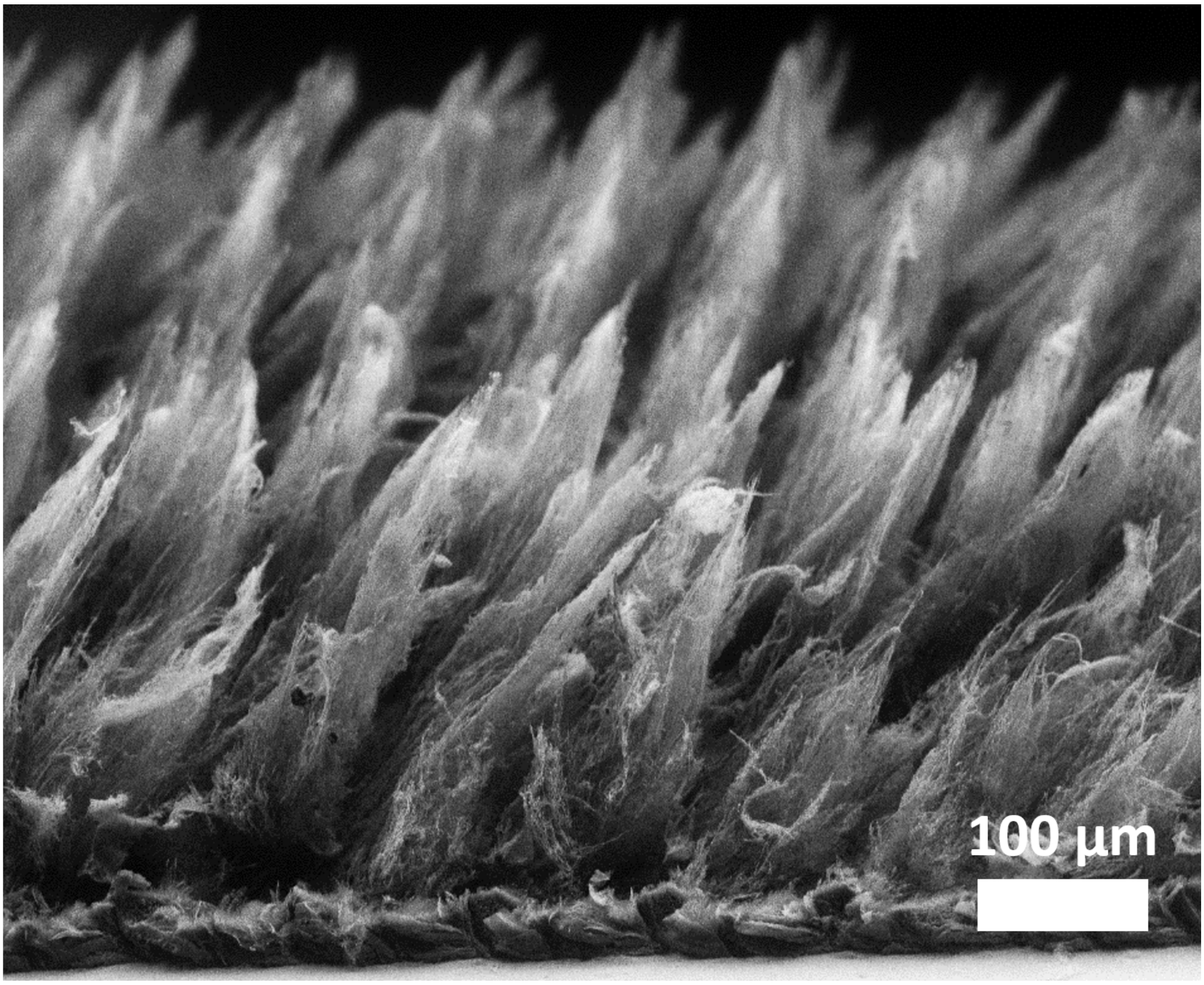

Figure 4.24.: SEM images of an LIGF-ID5 cross section

First it was recognized that the grown fibres were all bending in the same direction. Since the laser lines had a width around 120 µm and the average distance between two neighbouring lines in ID5 was approximately 50 µm (see table 4.3), the single rows made of those fibre-bundles referred to alternating laser line directions because they were separated by around 100 µm . The one-sided bending in cross sectional view might be caused by the laser itself, since the fibres observed in top view images also tended to grew away from the laser impact centre. Hence it was assumed that in the case of LIG of figure 4.24 the laser was rastering over the polymer sheet starting at the right side of this image.

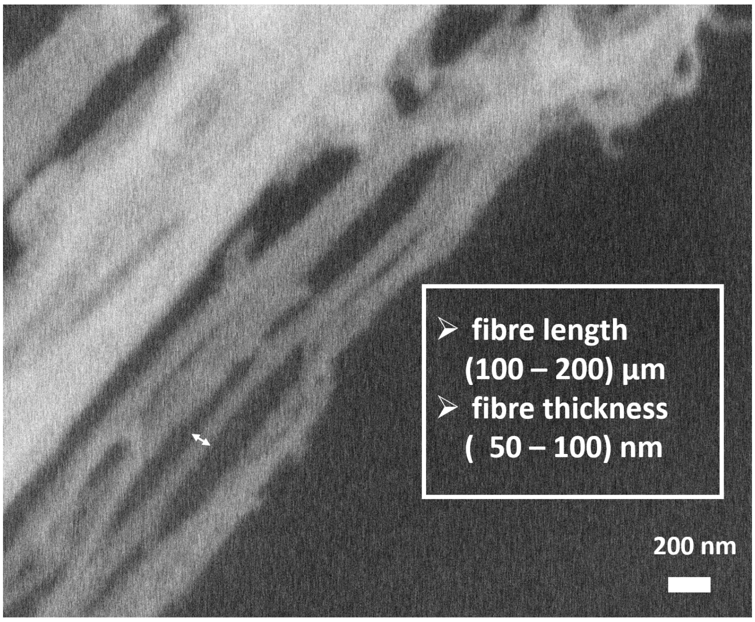

Figure 4.25.: SEM images of a LIGF-ID5 sample

The approximate length of LIG-fibres was estimated by the sample seen in figure 4.24 and the thickness of one single fibre was evaluated with help of the high magnification SEM image seen in figure 4.25. Both figures show the same sample which was produced with the standard settings for LIG-fibres samples found in table 3.4) . The qualitative assessments for fibre length was about 200 µm and for the fibre width about 100 nm, summarized in figure 4.25.

Vector mode

In vector mode scribing of single laser spots with different Z-setting were made. Left side of figure 4.26 shows a typical laser impact area referred to the flat-LIG morphology obtained at $Z = -0.9\,\mathrm{mm}$. A circular laser spot with sharp edges and almost no fibres sticking out of the sides was seen. Further a morphology difference just in this single laser spot was found. While the edges looked more even and flat, the centre appeared more diffuse and rough. Since the laser cutter provided Gaussian shaped laser spots, this change in structure was ascribed to the fluence development within one laser spot.
A complicated candyfloss shaped interplay of LIG-branches in the middle of the impact area is evidenced at increasing magnification (figure 4.26, right).

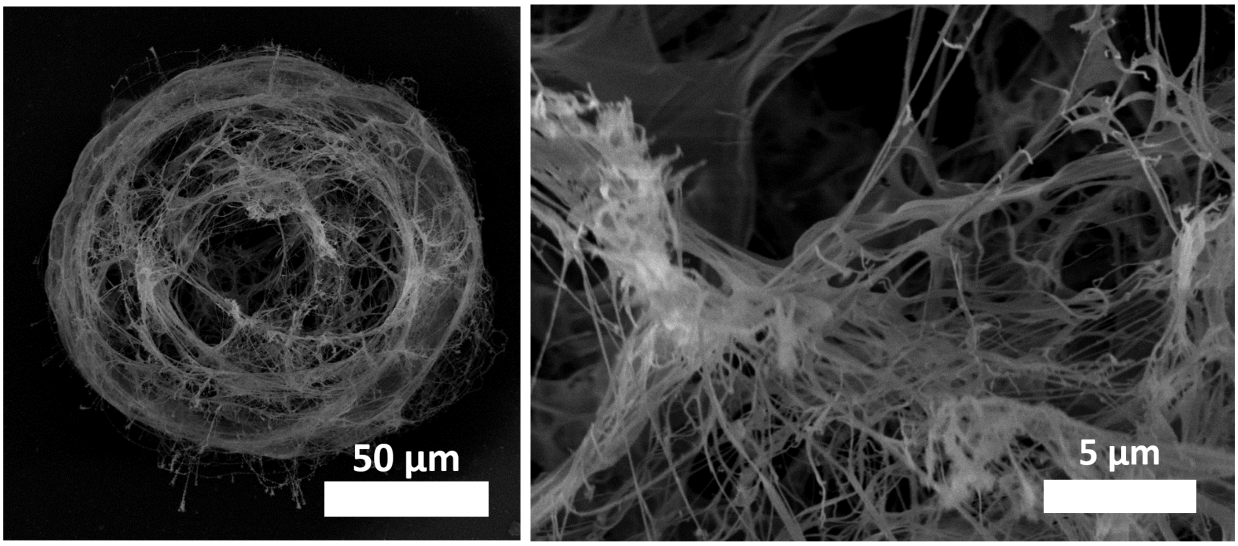

Figure 4.26.: SEM images of a single flat-LIG laser spot obtained at Z = −0.9 mm

By reducing Z from Z = −0.9 mm to Z = −0.6 mm the laser fluence correspondingly increased and a different LIG morphology was obtained (figure 4.27). Contrary to the flat-LIG morphology, seen in figure 4.26, the sample showed a LIG-fibre morphology with lot of fibres emerging in a radial way from the centre. In the right side of figure 4.27 a zoom of the middle part of the laser spot can be seen. Despite the general similitude with LIG obtained at Z = −0.9 mm (figure 4.26) few of the fibres in figure 4.27 showed some branching.

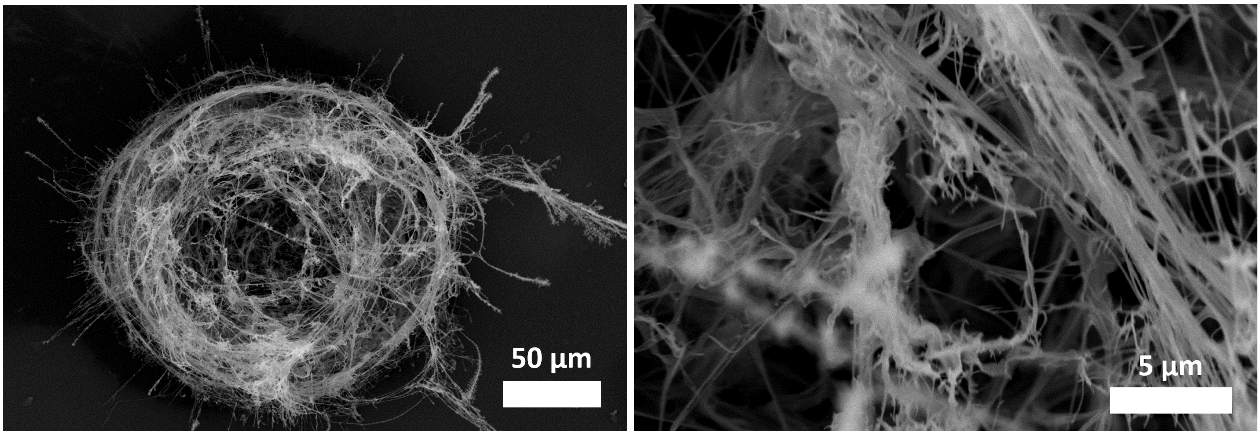

Figure 4.27.: SEM images of a single LIG-fibre laser spot at Z = −0.6 mm

At the ends of the fibres which were sticking out of the laser impact area in figure 4.27 a LIG morphology like seen in figure 4.28 was obtained. This kind of behaviour was found for laser spots produced with high fluence values and therefore was called LIG-branching. The branching was found at the tip of fibres and unfortunately the origin for this morphology remained unexplained, since this also could be a caused by the Ag-layer on top. This Ag-layer was made with a PVD process (see section 3.4.3) to prevent charging effects during the SEM observation and was around 40 nm thick.

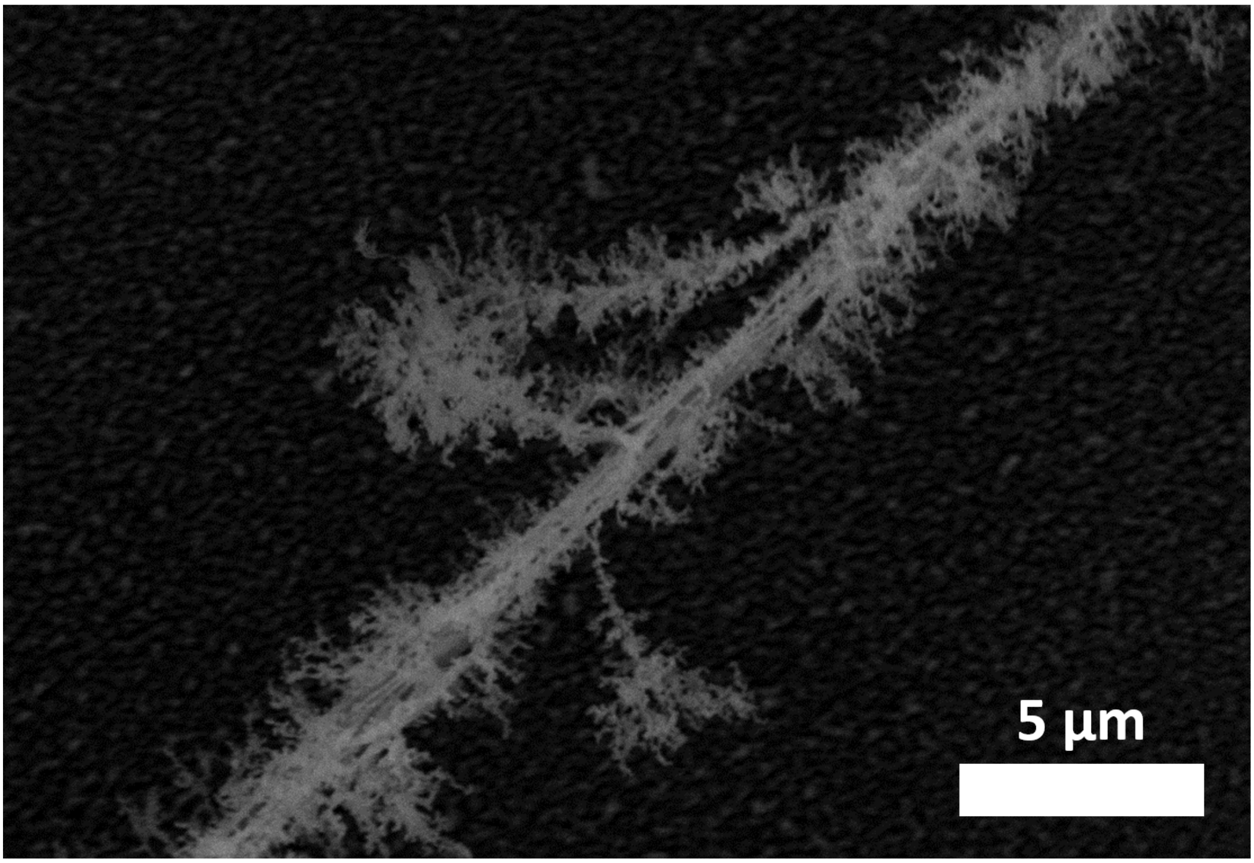

Figure 4.28.: SEM images of a branching fibre

4.3.3. TEM

TEM micrographs of a LIGF-ID2 cross-section are shown in figure 4.29 and figure 4.30.

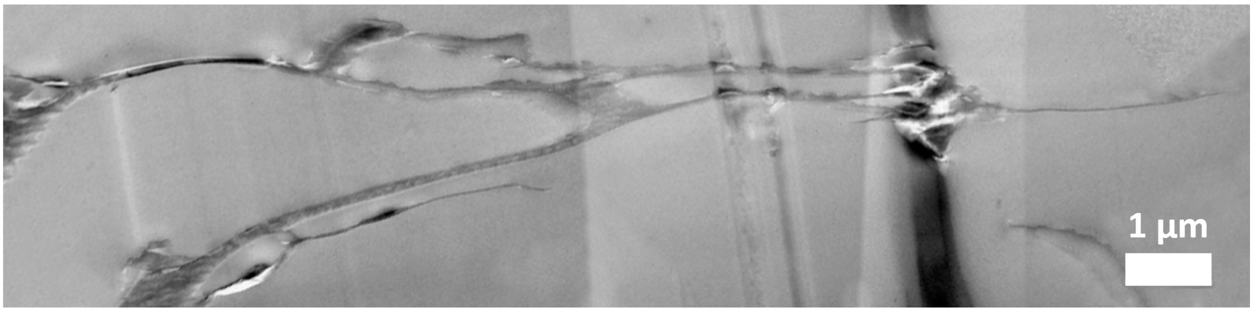

Figure 4.29.: TEM images of a fibre from a LIGF-ID2 cross section

The vertical scoring was due to dragging of sample pieces during the cutting process. Nevertheless a LIG fibre was observed and a TEM image of its tip can be seen in figure 4.30 (a).

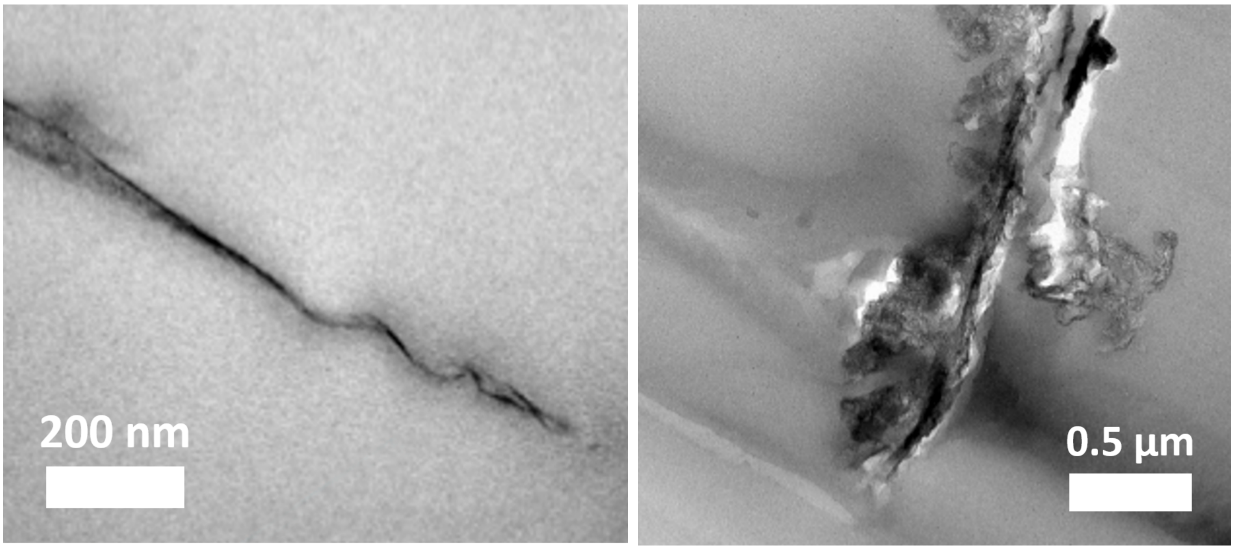

(a) tip of a fibre (b) branching

Figure 4.30.: TEM images of a single LIG-fibre

A qualitative assessment for the width of a fibre was made and it was observed that it changed from around 100 nm at the beginning to a few nm at the tip of a fibre. Another eye catching artefact can be seen in figure 4.30 (b) showing a blurred fibre tip, possibly caused due to the formation of scoring during the cutting process. Perhaps, this also can be referred to the fibre branching observed with the SEM, see figure 4.28, indicating that this is an artifact not induced by the Ag-layer made for the SEM observation but a further LIG-morphology, owning a high specific surface area. Since LAMPSe started to investigate the usage of LIG as electrodes for supercapacitors, their specific surface area (A_{BET}), which is proportional to the capacity, should be as high as possible. Past performances of Gas Adsorption Measurements (BET) for powder LIG, performed with a Micromeritics 3Flex equipment at the Institute of Physical and Theoretical Chemistry at TU Graz, showed that LIGP had around $A_{BET} = 200\,\frac{\mathrm{m}^2}{\mathrm{g}}$ and LIGF approximately $A_{BET} = 300\,\frac{\mathrm{m}^2}{\mathrm{g}}$. Hence, if the branching is a new discovered LIG morphology, a measurement of A_{BET} would be interesting to determine its suitability as a supercapacitor electrode. [25]

4.4. LIG-fibre composition

The composition of a LIGF-ID2 and a LIGF-ID5 sample, was investigated with a correlative Raman SEM-technique and a Raman spectrometer in collaboration with FELMI-ZFE, TUGraz (Dr. H. Fitzek). In particular, this study permitted to elucidate the structural and composition change along a cross section.

4.4.1. Raman spectra of single fibres

In figure 4.31 the used cross section of the LIGF-ID2 and LIGF-ID5 samples and the corresponding measurement positions, illustrated as black crosses, can be seen.

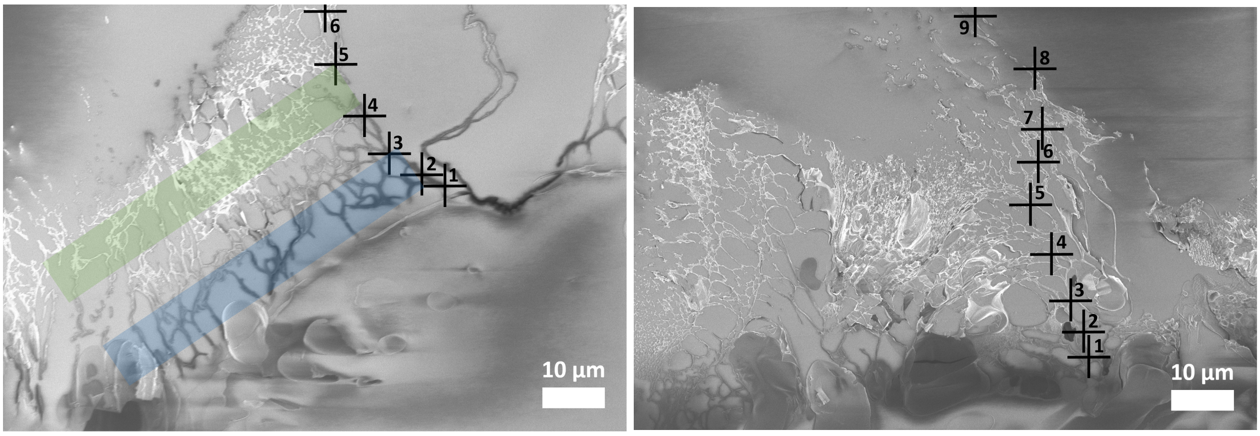

(a) LIGF-ID2

(b) LIGF-ID5

Figure 4.31.: Positions of Raman measurements on cross sections of LIGF samples

For a better understanding of the taken SEM images (figure 4.31) and the approximate trend of the taken Raman spectra (illustrated by the red crosses) a sketch of the sample can be seen in figure 4.32.

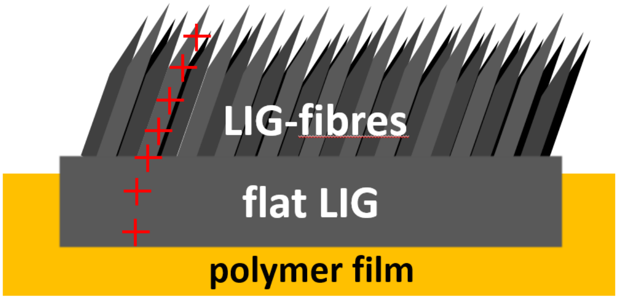

Figure 4.32.: Orientation and direction of Raman measurements on a LIG-fibre cross section

In figure 4.33 all spectra taken along the measurement points marked in figure 4.31 (b) can be seen. Since a correlative Raman-SEM technique was used the desired measurement spots were selectable via the SEM image. Only 9 measurement spots are visible in figure 4.31 (b), but 11 spectra were overall taken (see figure 4.33). Although the SEM image was used as an orientation, the whole working range could not be taken in the same field of view. The spectra 10 and 11 were made even closer to the fibre tip.

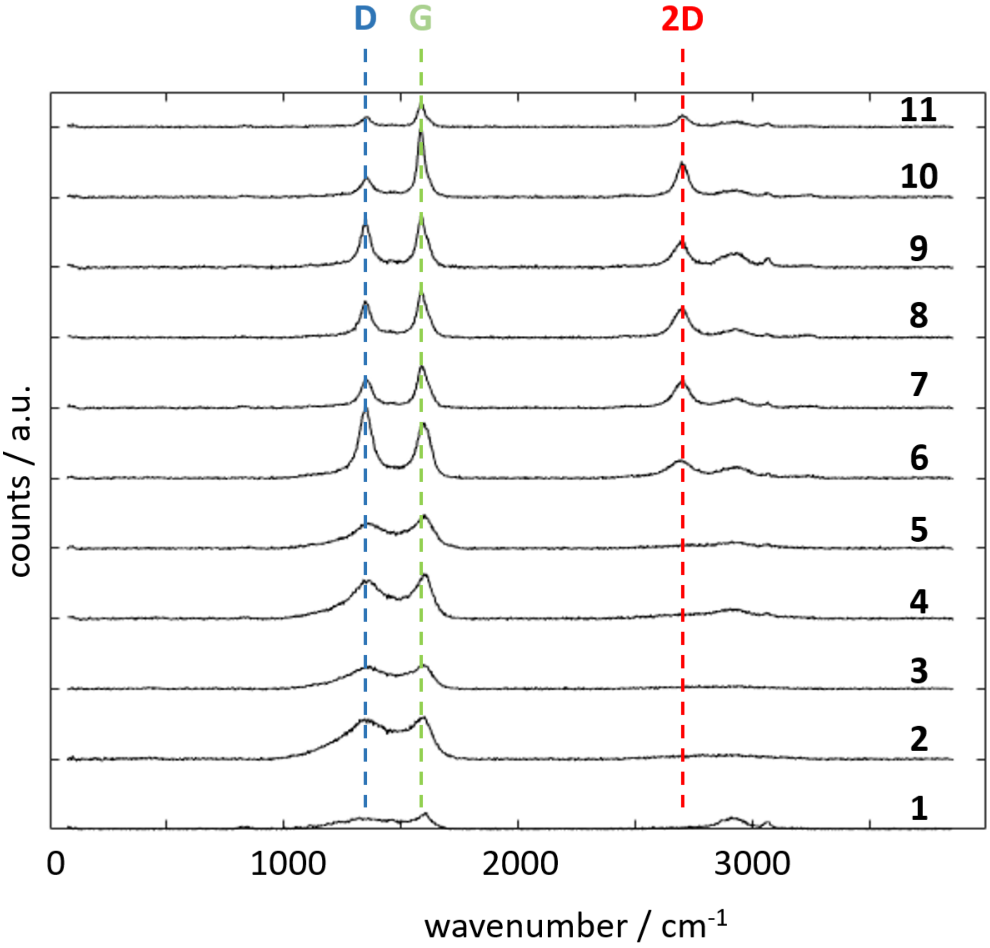

Figure 4.33.: Raman spectra of an LIGF-ID5 sample

Results for the G-band position (ν_G), the intensity ratios between the bands (I_{2D}/I_G and I_D/I_G), the grain size (L_a) and the fwhm (full width at half-maximum) from G ($fwhm_G$)- and D-band ($fwhm_D$) can be found in table 4.8.

Table 4.8.: Results for a correlative Raman-SEM-measurement performed on a LIGF-ID5 sample

	LIGF-ID5					
	ν_G / cm^{-1}	I_{2D}/I_G	I_D/I_G	L_a / nm	fwhm$_G$ / cm^{-1}	fwhm$_D$ / cm^{-1}
1	1598	0	0.97	5.4	74	346
2	1591	0	1.19	6.0	104	309
3	1593	0	1.09	5.7	100	276
4	1595	0	0.96	5.4	97	230
5	1596	0	0.87	5.1	106	238
6	1596	0.33	1.29	6.3	71	67
7	1593	0.65	0.70	7.1	58	59
8	1590	0.66	0.81	6.1	55	55
9	1589	0.52	0.95	5.2	53	52
10	1586	0.52	0.27	18.4	35	67
11	1588	0.49	0.42	11.8	38	52

Plots for the results displayed in table 4.8 can be found in figure 4.34.

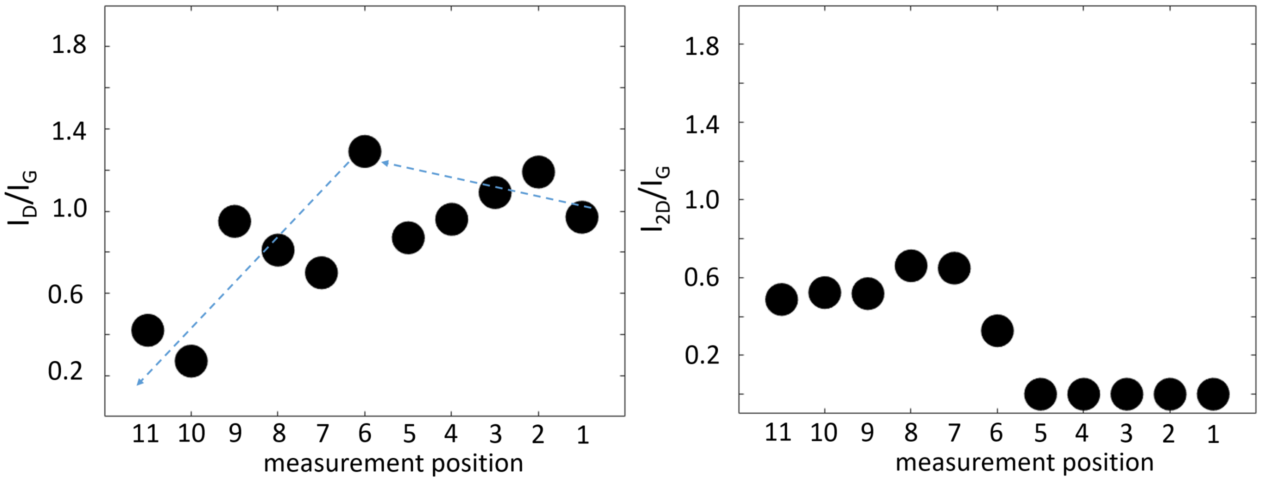

(a) I_D/I_G-ratio (b) I_{2D}/I_G-ratio

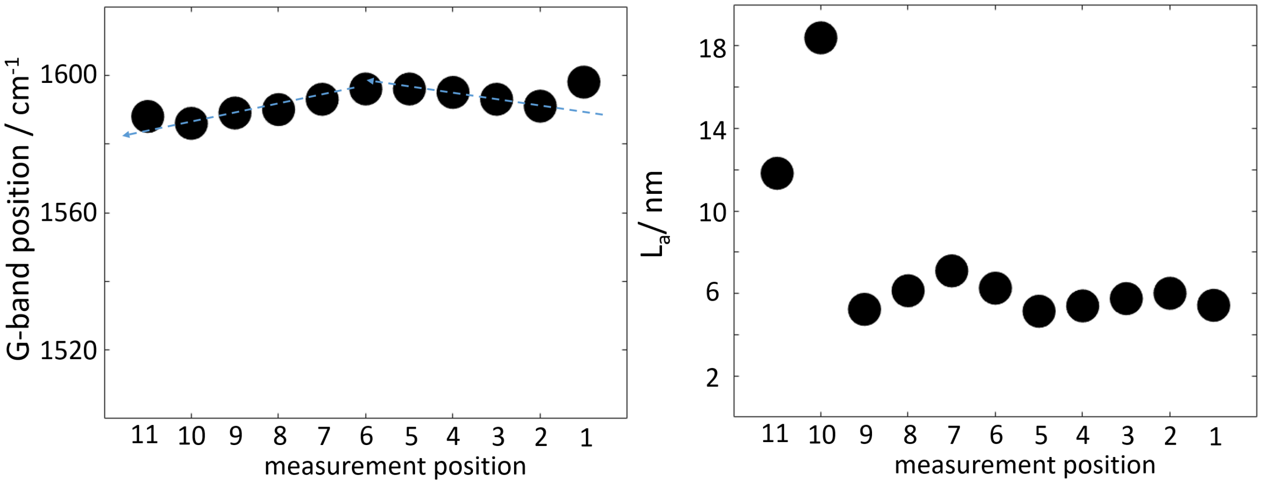

(c) G-band position (d) grain size

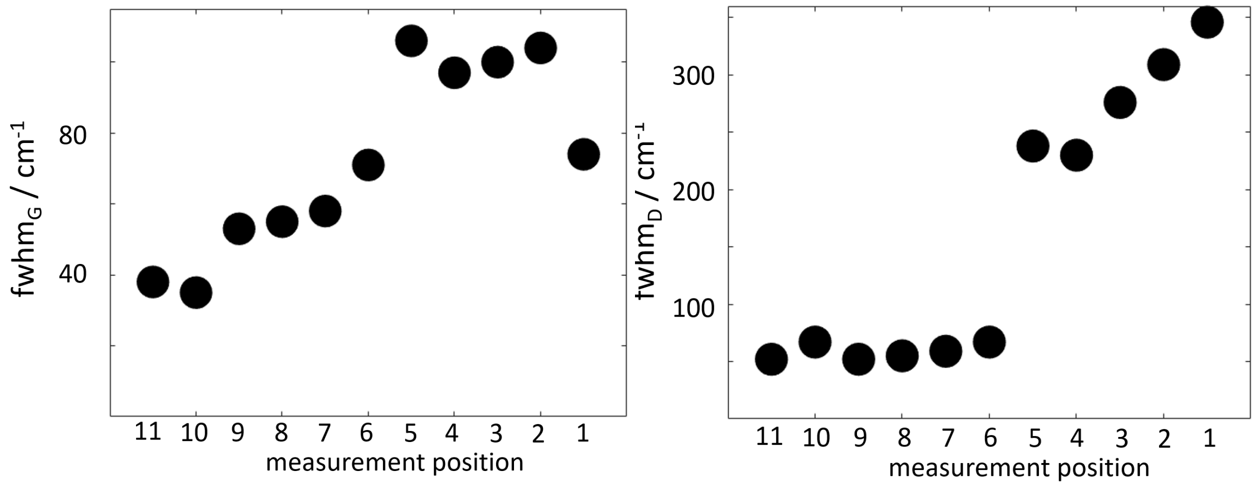

(e) G-band width (f) D-band width

Figure 4.34.: Results of intensity ratios, G-band position, grain size and fwhm of G- and D-band for a LIGF-ID5 sample

The observed bands were marked with a blue (D-band: at $\sim 1580\,\mathrm{cm}^{-1}$), green (G-band: at $\sim 1350\,\mathrm{cm}^{-1}$) and red (2D-band: at $\sim 2700\,\mathrm{cm}^{-1}$) dashed line in figure 4.33. The bands above the 2D band at around $2950\,\mathrm{ucm}^{-1}$ emerged from the embedding resin.

The blue D-band was present in all spectra, which stood for defects leading to a disorder and disturbed symmetry (defects in honeycomb carbon lattice). Therefore, it would not be visible in Raman spectra for perfect graphene. Although the D-band always had a similar intensity compared to the G-band, it started to decrease, starting from spectra 10. This suggested that near the tip of the fibre the structure became more alike the one of perfect graphite. This assumption also got supported by the decrease in band width of D- and G-bands, found in table 4.8 as fwhm_G and fwhm_D. fwhm_G decreased from $\sim 100\,\mathrm{cm}^{-1}$ at the substrate surface to $\sim 40\,\mathrm{cm}^{-1}$ at a distance of 60 µm from the PI sheet and fwhm_D decreased accordingly from $\sim 350\,\mathrm{cm}^{-1}$ to $\sim 50\,\mathrm{cm}^{-1}$.
Next, there was a visible change from a more amorphous to a more crystalline structure from spectrum 5 to 6, indicated by the arising of the 2D band.

In order to compare the trend of ν_G and the intensity ratio $\mathrm{I}_D/\mathrm{I}_G$ with the schematic trend found in literature (see figure 2.1), the measured data were plotted in figure 4.34 and can be found in table 4.8. Further an investigation was made in the intensity ratio $\mathrm{I}_{2D}/\mathrm{I}_G$ as well as in L_a. The latter was calculated after equation (2.11), for the measurement points 1 to 5 and after equation (2.13) for the remaining ones. The wavelength dependent factor $\mathrm{C}(\lambda)$, described in section 2.5 (see equation (2.12)), needed for this purpose was calculated with $\lambda = 532.26\,\mathrm{nm}$ and turned out to be $\mathrm{C}(\lambda) = 4.96\,\mathrm{nm}$.

All in all the intensity ratio $\mathrm{I}_D/\mathrm{I}_G$ as well as ν_G, seen in figure 4.34 (a) and (c), followed the schematic trend (figure 2.6), illustrated as the blue dashed lines. In combination with the observation of 2D-band, arising at the sixth measurement point (i.e. obtained at a distance of around 30 µm from bottom) and present in all the following spectra, these results evidence a transition from an amorphous carbon to a noncrystalline graphite structure.

The observed trend of $\mathrm{I}_{2D}/\mathrm{I}_G$ (figure 4.34 (b)), can be explained by an increase of order with increasing distance from the bottom of the LIG. Moreover, the observed value for $\mathrm{I}_{2D}/\mathrm{I}_G = \sim 0.7$ evidences the presence of multiple layers of graphitic carbon; a single layer graphene has $\mathrm{I}_{2D}/\mathrm{I}_G \geq 2$. [26].
After [27] the wavenumber of the 2D-band from a single layer graphene (around $2679\,\mathrm{cm}^{-1}$) shifts to higher values for an increase in layer number (graphite). Further, the fwhm of the 2D-band width increases for graphite, starting from around $30\,\mathrm{cm}^{-1}$.
It turned out that the approximate wavenumber for the 2D-bands were around $2700\,\mathrm{cm}^{-1}$ and the fwhm at (80 - 100) cm^{-1}, which suggested a multiple layered graphene (graphite).

The related grain size L_a increased along the fibre growth direction (figure 4.34 (d)). For the amorphous carbon structure the grain size was around 6 nm and increased to a maximum of 18 nm in the nanocrystalline graphite regime.

Similar results were obtained for the LIGF-ID2 sample, and they can be found in appendix A.5.1. This observation suggested that, despite the ID setting changed slightly the LIG morphology, it did not affect the composition and how this changes along the fiber growth direction.

Passive Voltage Contrast

By just looking at the SEM images (figure 4.31) it was conspicuous that the LIG directly emerging from the precursor appeared to be darker compared to the fibres around 30 µm apart from the polymer surface. This effect is known as *Passive Voltage Contrast* (PVC) and typically used for semiconductor failure localization with a SEM. It is based on a brightness difference between conducting structures, where in case of positive charging, areas with a lower conductivity appear darker compared to better conducting regions. [28]
Hence, it was assumed that the conductivity of the produced LIG increased with distance to the polymer precursor.

A comparison between Raman spectra taken in the darker area (blue marked region) in figure 4.31 (a), referred to the bottom of the LIG sample, and the brighter area (green marked region), referred to a position closer to the tip of a fibre, can be seen in figure 4.35.

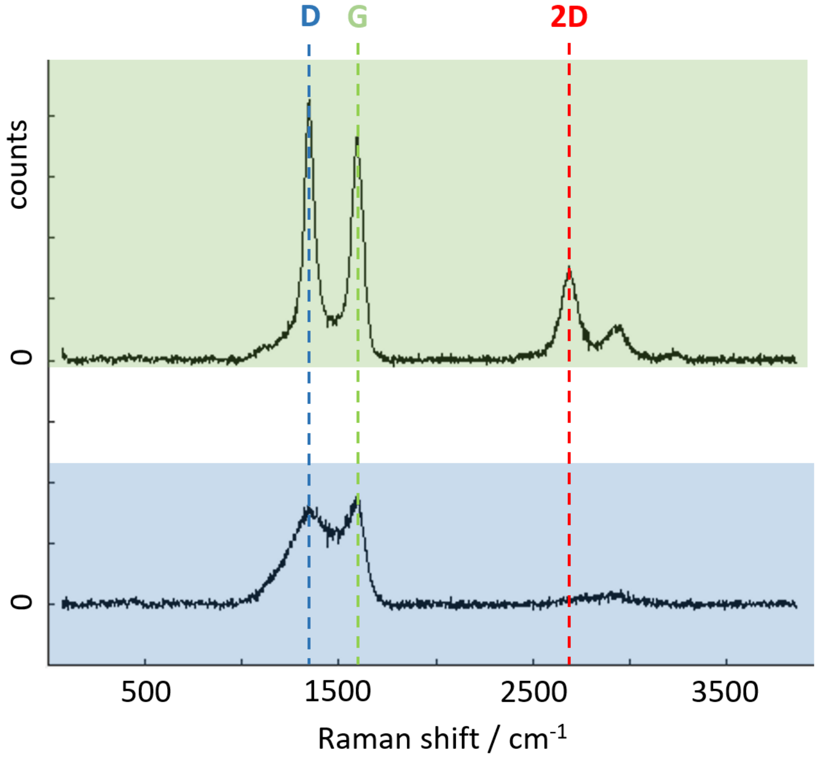

Figure 4.35.: Passive Voltage Contrast at an LIGF-ID2 sample

In both regions the characteristic G-band (green dotted line) at around 1580 cm^{-1} and D-band (blue dotted line) at 1350 cm^{-1} can be seen.
Clearly, those two bands were overlapping and broad in the Raman spectrum taken at the bottom of the scribed LIG (blue area). The 2D-band (red dotted line), at 2700 cm^{-1}, was missing, indicating an amorphous graphene structure. Further, an existence of the D-band suggested the presence of defects.
The $fwhm_G$ decreased from $\sim$100 cm^{-1} to $\sim$40 cm^{-1} and $fwhm_D$ from $\sim$350 cm^{-1} to $\sim$50 cm^{-1} going in the direction of the fibre growth, seen in the green Raman spectrum in figure 4.35. Together with the appearance of the 2D-band these features evidenced a more ordered and crystalline structure. Nevertheless, the D-band indicated a still present disturbed symmetry (defects in the honeycomb carbon lattice).

4.4.2. Raman Mapping

To be sure that the observation of a structural change along the fibre growth took place at the whole sample and not only along a single fibre, a Raman mapping was made. Here, Raman spectra were collected at every pixel (Mapping resolution of 1 µm) of a selected microscope field of view, see figure 4.36 (a). Area of measurment is evidenced in the microscope image (figure 4.36 (a), left). The sample orientation as well as the evaluable measurement points (pixels), marked as red squares, can be seen on the right side. The black area referred to points were the Raman signal was too low or only the embedding resin was measured.
A mapping of G-band position (ν_G), $\mathrm{I}_D/\mathrm{I}_G$ and fwhm$_{2D}$ is displayed in figure 4.36 (b), (c) and (d) respectively. In figure A.4 and figure A.5 the results for the fwhm$_G$ and fwhm$_D$ can be seen.

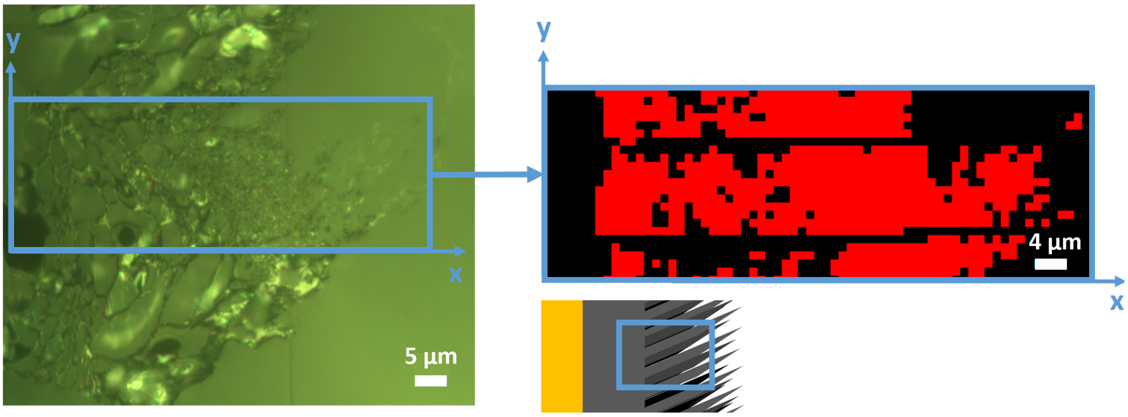

(a) Optical microscope image and measurement points of the Raman mapping

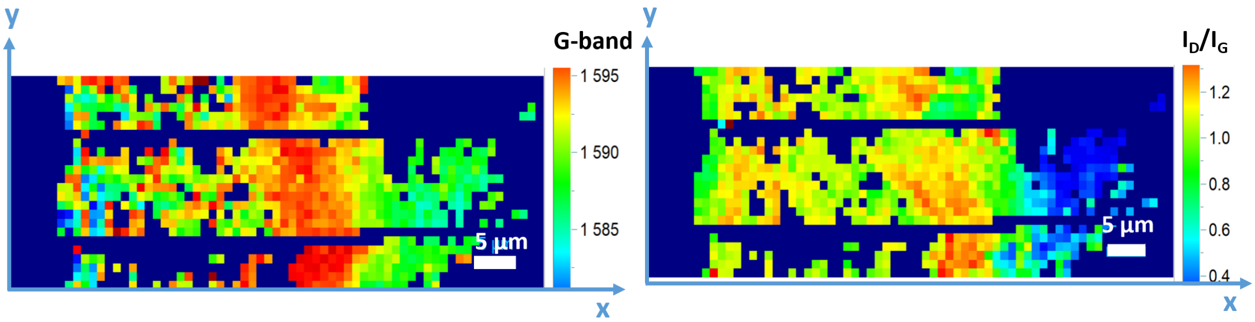

(b) G-band position

(c) Intensity ratio between D- and G-band

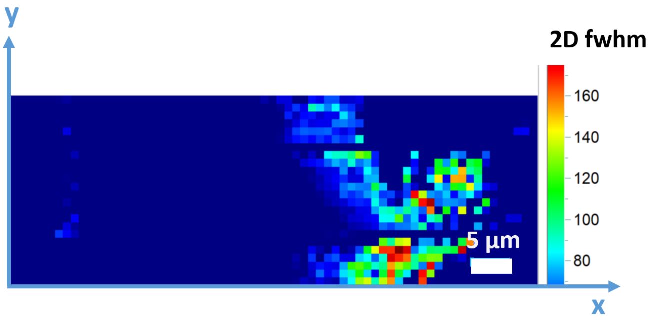

(d) Raman mapping of 2D-band width

Figure 4.36.: Raman mapping of a LIGF-ID5 sample

Overall the results of Raman mapping showed again a transition from a more amorphous structure at the bottom of LIG to a more ordered crystalline structure approaching the tip of the fibre at around 30 µm distance from the bottom. This is in good agreement with the outcome of the correlative Raman SEM measurements. The evidences for this structural change already were discussed in the section about Raman spectra of single fibres.

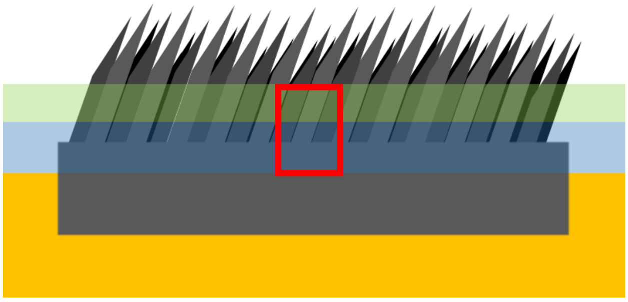

Figure 4.37.: Sketch of the measured part of the sample

The actual LIG fibre length was estimated with the help of a taken SEM cross section, seen in figure 4.24, to around 100 µm. Due to difficulties concerning the probe preparation, only a part of the actual fibre growth was experimentally accessible. Since the fibres were emerging from the PI in a tilted way, seen in figure 4.24, the manageable cross section was made at the bottom half of the sample, see figure 4.37. The measured area was marked with the red rectangle and and the observed structural change was highlighted by the blue area referring to the amorphous carbon and the green area representing the nanocrystalline graphite. Due to the lack of knowledge concerning the tip of the sample, the composition regarding the remaining part of the fibres stays unexplored.

4.4.3. Comparison of LIGF composition with other groups

Tour group

Raman spectroscopy was mainly used to confirm the graphitic nature of the produced LIG by the Tour group. Although an effort was made in finding the carbonization threshold of the laser fluence ($\sim 5.5\,\mathrm{J \cdot cm^{-2}}$, [1]) and to observe Raman spectra of LIG produced with different laser powers (change of laser fluence), no in-depth study of structural/compositional change along the LIG growth was made. [9], [17].

In general, Raman Spectra performed by the Tour group showed a small I_D compared to I_G and also a strong I_{2D}. Hence, a more ordered structure of the produced LIG is assumed compared to the LIG scribed by LAMPSe. Here, similar overview Raman spectra (from the top, no cross section) like taken by the Tour group were made (see [2]). I_D and I_G were almost the same and the 2D band, although present, was clearly weaker in intensity than the other observed bands. This is surprising due to the fact that for LIG production a CO_2-laser with similar wavelength, purchased by the same provider (ULS), was used. [17], [9]
Nevertheless, the study of Raman spectra for LIG scribed with an increasing laser power P = (2.4 - 5.4) W showed, that the quality of the LIG changed: First, the quality of LIG increased with increasing laser power (I_D decreased, I_G and I_{2D} increased) and at a laser power of P = 5.4 W the spectra changed drastically, showing broad D- and G-bands with similar intensities as well as a broadening and decrease of I_{2D}. Moreover, the Raman spec-

trum taken at P = 5.4 W looked more comparable to the spectra obtained by LAMPSe, where typically laser powers of P = 3 W for LIGP and P = 6 W for LIGF were used - but no such difference in the Raman spectra were observed here.

Cross sectional Raman study

In [6] a SEM image and Raman spectra along a ßLIG cross section were introduced. Again, Kapton® and a 10.6 µm CO_2 laser system from ULS were used. A very similar trend of amorphous carbon at the bottom of LIG to nanocrystalline graphite with increasing distance to the precursor was observed as in this study. Here, the appearance of the 2D band was observed at around 10 µm. Unfortunately, no in depth discussion concerning this behaviour or the reason for this transition was made. [6]

4.4.4. Interpretation of structural change along LIGF growth: possible causes

The presence of a structural and compositional change across a cross section of a LIGF sample in Z-direction was evidenced and discussed in the previous section.

Such structure is formed during the photothermal laser induced process which is yet not fully understood ([1], [2], [9]). Indeed, a direct in situ and localized investigation of the scribing process and formation of LIG is very challenging, if not hardly doable. Nevertheless, a trial to investigate a possible cause for explaining this phenomenon in the available literature about carbonaceous materials was made.

In geology Raman spectra of carbonaceous material are made in order to find the metamorphic peak temperature, that is the maximum temperature at which pre-existing rocks were exposed during a structural change in solid state (metamorphism). [29]
For this purpose the structural order gets investigated. Raman spectra showing a well crystallized graphite structure are referred to a high peak temperature ($T > 650\,°C$), spectra of amorphous structures to lower peak temperatures ($T < 280\,°C$) and a transition between those two regions (i.e. with a coexistence of amorphous and crystalline regions) - to moderate peak temperatures ($280\,°C \leq T \leq 650\,°C$), [29]. Hence, given the gradient in composition observed in LIGF samples, a temperature gradient along the Z-axis during the photothermal process was assumed.
The generated heat during the engraving process depends on the spots size, and therefore on the distance of the surface from the focal position, the absorption coefficient (δ) and the specific heat capacity (c) of the material, see section 2.3.

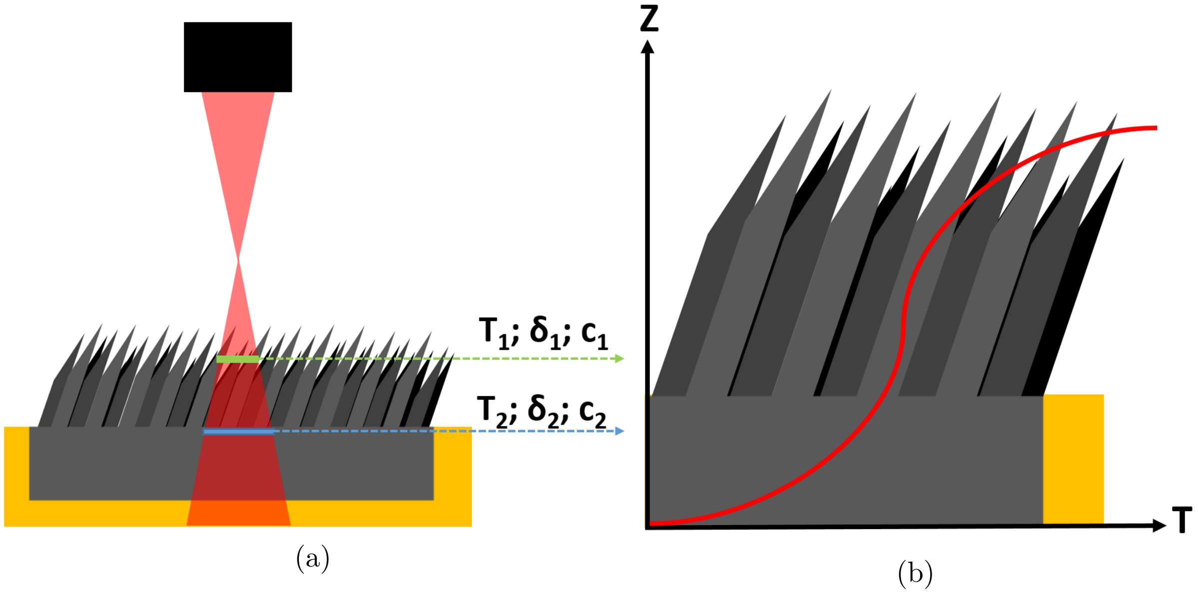

(a) (b)

Figure 4.38.: Sketch of LIGF production in defocused positions and temperature trend

Usually, LIG-fibre samples were produced at Z = 0.3 mm and therefore out of the focal position, causing that the tip of the fibres (length of 200 - 300µm) are much closer to the focal point compared to the surface of polymer precursors. As a result they get exposed to higher fluence during the photothermal process. A schematic illustration can be found in figure 4.38 (a). Taking into account that the lasering process itself led to an overlapping of single laser pulses during the engraving process, δ and c were changing constantly. Hence, a exact calculation for the generated heat was not possible. Nevertheless, it was assumed that this pulse overlapping in combination with the difference in laser spot size, occurring in vertical direction of the lasering process, led to the observed structural change. According to the findings in [29] the generated temperature at the amorphous part of the LIG sample should be around (2 - 3) times lower compared to the one at the nanocrystalline structure. A schematic trend of the temperature along the fibre growth can be seen in figure 4.38 (b). It was assumed that the temperature increases with decreasing distance to the focal point (Gaussian like) and has two plateaus, one for the specific heat capacity and absorption coefficient of the precursor and one for the LIG.

4.5. Influence of ID-setting in raster mode on LIGF resistance

4.5.1. LIGF resistance on PI

In table 4.9 the dependence of LIGF sheet resistance on PI ($R_{0,PI}$) to the ID setting can be found.

Table 4.9.: LIGF resistance on PI ($R_{0,PI}$) scribed at H = (42 ± 4) $J \cdot cm^{-2}$

	ID1	**ID2**	**ID3**	**ID4**
$\mathbf{R_{0,PI}}$ / Ω	(560 ± 110)	(240 ± 60)	(133 ± 5)	(113 ± 5)

The resistance $R_{0,PI}$ was decreasing with increasing ID value, which is reasonable due to the fact that the number of laser lines per cm increases with increasing ID setting, see table 4.3 and figure 4.39 (a). Therefore more of the polymer precursor was transformed into conductive material.

4.5.2. LIGF resistance on MA

In table 4.10 the dependence of LIGF sheet resistance on MA ($R_{0,MA}$) to the ID setting can be found.

Table 4.10.: LIGF resistance on MA ($R_{0,MA}$) scribed at H = (42 ± 4) $J \cdot cm^{-2}$

	ID1	**ID2**	**ID3**	**ID4**
$\mathbf{R}_{0,MA}$ / kΩ	(130 ± 40)	(30 ± 10)	(110 ± 40)	(75 ± 35)

It is notable that the decreasing trend observed in table 4.9 for samples on PI was true again for ID1, ID3 and ID4, but the sample prepared with ID2 clearly showed the lowest resistance on MA. This may be caused due to the fact that laser lines made with ID2 were almost touching each other (see figure 4.18) and the LIG-fibres emerging from the substrate were really in contact and therefore provided a conductive sheet. At higher ID values, the laser impact areas of neighbouring lines were already overlapping which probably led to a partial destruction of the LIG-fibres. Nevertheless, more fibres were created with higher ID settings which led to a corresponding decrease in sheet resistance, see figure 4.39 (b).

The trend for the $R_{0,PI}$ and $R_{0,MA}$ against the number of scribed lines (see table 4.3) for ID1 to ID4 can be seen in figure 4.39.

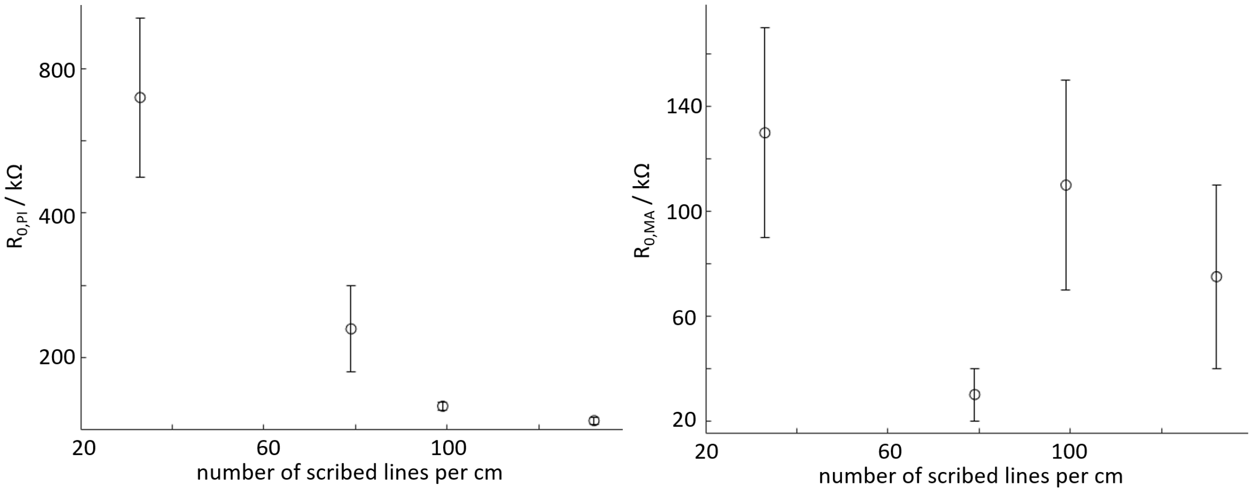

(a) $R_{0,PI}$ (b) $R_{0,MA}$

Figure 4.39.: Relationship between the LIGF-resistance on PI ($R_{0,PI}$) and MA ($R_{0,MA}$) for different ID settings (varying number of scribed lines per cm)

4.5.3. Influence of ID-setting in raster mode on LIGF resistance on MA and applied strain

Since the foreseen application of LIG transferred on MA is to act as stretchable conductors/sensors, their electromechanical behaviour was assessed under different conditions of stretching in a dedicated tensile testing experiment.

Only the LIGF transferred to the MA were tested with the Stretcher. Hence, $R_{0,MA}$ is renamed in R_0 for an easier notation.

For ID1 to ID4 the resistance without applied strain (R_0) (see table 4.10) and the relation between R_0 and the resistance in relaxed state (R_r) as well as in stretched condition (R_s) were measured with the tesile testing device called Stretcher (see section 3.5.2). The settings found in table 3.7 were used and the results can be found in table 4.11. Exemplary, the results for an ID2-LIGF sample with an applied strain of $\epsilon = 30\,\%$ and $\epsilon = 100\,\%$ were plotted in figure 4.40. The yellow trend was referred to the first stretcher cycle and the red line to the last one. On the left side of each plot the relation R_s/R_0 was found and on the right side R_r/R_0.

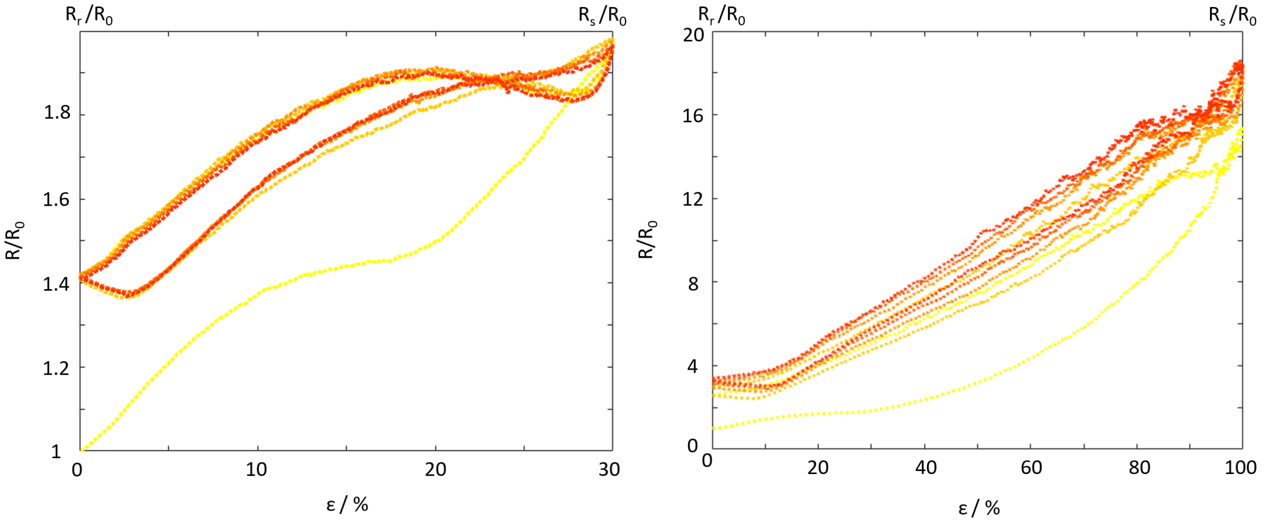

(a) $\epsilon = 30\,\%$ (b) $\epsilon = 100\,\%$

Figure 4.40.: Normalized resistance for tensile testings of an ID2-LIGF sample with different maximal applied strain ϵ

.

Table 4.11.: Resistance of MA/LIGF-composites with different ID-settings in stretched (R_s) and relaxed (R_r) condition

ID1				**ID2**			
ϵ / %	$\mathbf{R}_0$ / kΩ	$\mathbf{R}_r/\mathbf{R}_0$	$\mathbf{R}_s/\mathbf{R}_0$	ϵ / %	$\mathbf{R}_0$ / kΩ	$\mathbf{R}_r/\mathbf{R}_0$	$\mathbf{R}_s/\mathbf{R}_0$
5	130 ± 40	1.1 ± 0.1	1.7 ± 0.2	5	30 ± 10	1.3 ± 0.1	1.4 ± 0.2
10	120 ± 30	1.6 ± 0.2	2.6 ± 0.4	10	36 ± 12	1.3 ± 0.1	1.5 ± 0.1
20	130 ± 20	1.9 ± 0.4	5.1 ± 1.1	20	38 ± 12	1.5 ± 0.1	2.0 ± 0.3
30	150 ± 30	1.8 ± 0.4	12.0 ± 7.0	30	45 ± 16	1.5 ± 0.1	2.6 ± 0.4
100	200 ± 30	14.0 ± 7.0	-	100	50 ± 18	4.0 ± 0.9	-
ID3				**ID4**			
ϵ / %	$\mathbf{R}_0$ / kΩ	$\mathbf{R}_r/\mathbf{R}_0$	$\mathbf{R}_s/\mathbf{R}_0$	ϵ / %	$\mathbf{R}_0$ / kΩ	$\mathbf{R}_r/\mathbf{R}_0$	$\mathbf{R}_s/\mathbf{R}_0$
5	110 ± 40	1.6 ± 0.2	1.8 ± 0.2	5	75 ± 35	1.7 ± 0.3	2.0 ± 0.4
10	130 ± 50	1.6 ± 0.2	1.8 ± 0.3	10	90 ± 30	1.8 ± 0.1	2.3 ± 0.3
20	150 ± 60	1.9 ± 0.3	2.7 ± 0.7	20	100 ± 35	2.1 ± 0.1	4.2 ± 0.9
30	180 ± 80	2.0 ± 0.4	4.0 ± 1.6	30	130 ± 40	2.3 ± 0.1	-
100	230 ± 110	8.3 ± 4.0	-	100	150 ± 70	14.0 ± 6.0	-

In general the resistance on MA was decreasing with increasing ID setting. Only the ID2 sample showed a much lower R_0 compared to the other ones. A suitable explanation for this behavior could be that the LIG-fibres, which were relevant to produce conductive sheets on top of MA, were not destroyed on the sides of scribed lines, since an ID2-setting produces touching but not yet overlapping lines.

In table 4.12 the maximum applied strain (ϵ_{max}), before the sample lost its conductivity, can be found. Moreover, it was obtained that the loss of conductivity was a reversible process (despite a small decrease of R_0 with every cycle), as the sample became again conductive after the applied strain felt below ϵ_{max}.

Table 4.12.: Influence of the ID-setting to maximum conducting strain

	ID1	**ID2**	**ID3**	**ID4**
ϵ_{max} / %	43 ± 7	67 ± 2	45 ± 6	46 ± 7

Again, the samples with an ID2 setting were striking. While ID1, ID3 and ID5 showed a conductivity loss at around ϵ_{max} = (45 ± 7) %, ID2 samples were conductive up to ϵ_{max} = (67 ± 2) %. Here again, the probably longer and intact LIG-fibres located at the laser line sides resulted into a more stretchable conducting sheet, taking into account the effect of lateral striction: The sample experiences a reduction in width while stretched. Hence, intact fibers interconnecting neighbouring lines are pushed further close.

Therefore, a production of LIG-fibres samples with non-overlapping laser impact areas would be desirable. In raster mode the vertical distance between the scribed lines can be controlled by the ID-setting. But unfortunately, the PPI-setting in raster mode, specifying inter alia the horizontal distance between single laser spots, is fixed to at least 500 PPI (see section 3.3), which inhibits a production of LIG sheets without an overlapping of laser impact areas.

Influence of the ID- setting to plastic deformation and energy losses of the MA/LIGF-composites

For every tensile testing cycle with different strain (ϵ) the resistance of the MA/LIGF-composite in relaxed state (R_0) increased due to plastic deformation (see section 2.5.2), seen in table 4.11. In order to figure out if a dependence of the plastic deformation on the ID-setting exists, the stress-strain curves (exemplary for ID2-LIGF sample in figure 4.41) were analyzed and the energy losses per Stretcher cycle were calculated and summarized in table 4.13, after equation (2.14). [3], [2]

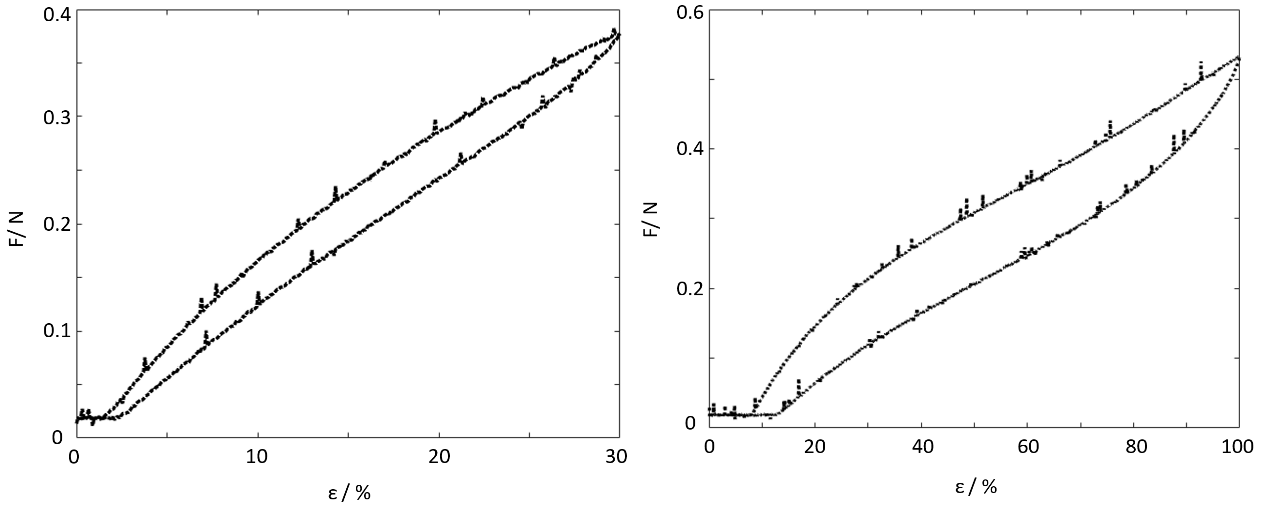

(a) $\epsilon = 30\,\%$

(b) $\epsilon = 100\,\%$

Figure 4.41.: Stress-strain curves for ID2-LIGF samples, with different maximal appleid strain ϵ

Since no major differences between the results received from samples made with different ID-setting were found, it was assumed that neither the plastic deformation nor the energy loss per cycle (C_X: X gives number of cycle) depends on the conductive layer on top of the MA. The results can be found in table 4.13.

Table 4.13.: Mechanical properties of the MA/LIGF-composites

ϵ / %	**plastic deformation / %**	$\mathbf{C_1}$	$\mathbf{C_{2-5}}$
5	0.11 ± 0.05	0.09	0.07
10	0.18 ± 0.07	0.13	0.09
20	0.90 ± 0.20	0.19	0.13
30	2.30 ± 0.30	0.21	0.15
100	14.20 ± 1.20	0.45	0.25

As it can be seen in table 4.13 the energy loss of the first tensile testing cycle (C_1) was always higher compared to the other ones (C_{2-5}) with $\Delta\text{loss}_{Ci} = 0.01$. This behaviour is typical for MA and called cyclic softening,[3]. Moreover, the MA showed a plastic and viscoelastic behavior, since the stress strain curve (figure 4.41) showed a hysteresis and the material does not return into its original shape (unequal origin and end of stress-strain curve).

4.6. Biological precursors

Numerous experiments to produce LIG on top of biological precursors like wood, cloth, paper or food were performed, [30], [1]. Even metal salts were used to enhance the quality of the produced LIG, [7]. Nevertheless, all successful experiments were made either in an inert atmosphere or using a more time-consuming multiple lasing process.
In this research an investigation of two different approaches for obtainingLIG from biological precursor was made. In the first one, a starch-derived polymer matrix calles Star-0 was crosslinked and mixed with different weight fractions of salts (NaCl and $Fe(NO_3)_3$), see table 3.1. In the second a keratin/PLA-baser biopolymer, provided by ISOF , produced in two different ways (electrospun and cast film) were observed.

4.6.1. Starch

Starch matrix: Star-0

Initially, the production of LIG was attempted on the produced bio-plastic - the so called starch matrix: Star-0. Unfortunately, the material tended to melt/degenerate before turning into a conductive sheet regardless of the laser fluence. This behaviour was foreseeable since the starch matrix had no flame-retardant properties. In figure 4.42 the produced bio-plastic, which turned out to be blurred, containing air inclusions, flexible and had a thickness of about 1 mm, can be seen. The upper half of the right image shows a laser treated area without a transformation into a conductive sheet (tested with a *Fluke*-Multimetre).

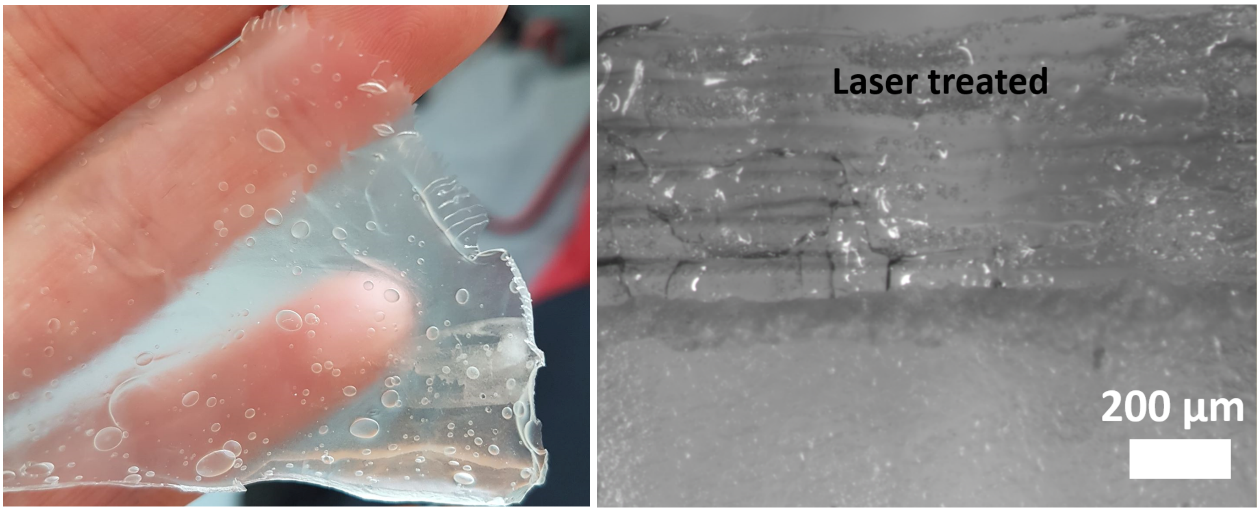

Figure 4.42.: Morphology and laser induced pyrolysis of Star-0

Star-0/NaCl

A first attempt to make the starch matrix more suitable for LIG synthesis was by adding 5 wt% of NaCl to Star-0 (see table 3.1) before the heating and stirring process. The NaCl was added to act as a flame retardant in the composite blend. The obtained material had less air inclusions but was not homogeneous with relatively large salt crystal agglomerates. In figure 4.43 the NaCl-bio-plastic after the laser pyrolysis can be seen. General laser settings as used for LIGP and LIGF, as well as one between them with P% = 15 % (table 3.4) were tried but no formation of a conductive layer was found.

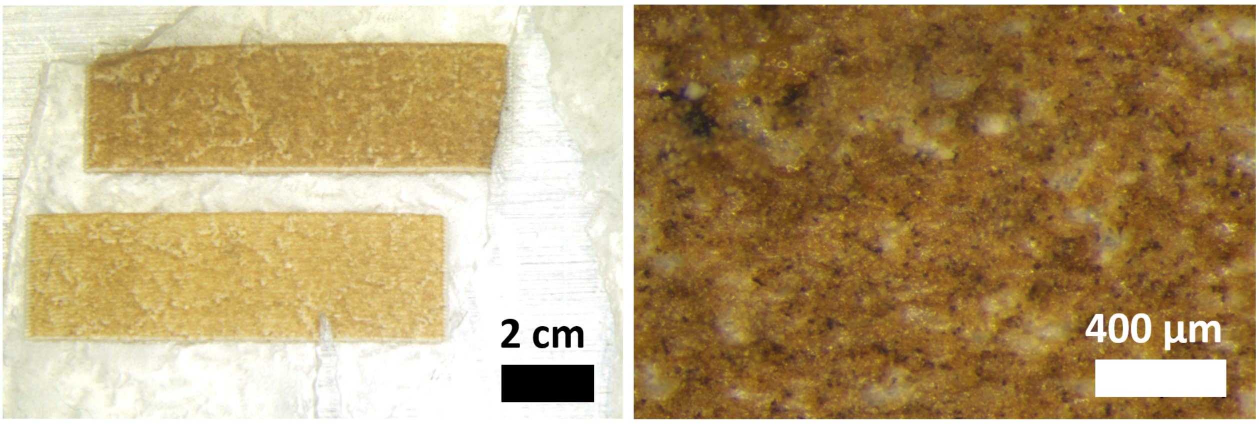

(a) top:P% = 15 %; bottom: P% = 10 %

(b) P% = 20 %

Figure 4.43.: Laser induced pyrolysis on Star-0/NaCl with different laser power settings P%

Starch matrix/Fe(NO_3)$_3$: Star-X

In a second attempt 5 wt% of Fe(NO_3)$_3$ was added to Star-0 (=Star-5) before heating, [7]. This attempt was based on previous findings that metal salts are effective in enhancing LIG formation in wood, given its capability to act as a flame-retardant, [7]. The obtained plastic sheet had an orange colour, was homogeneous and showed smaller and less trapped air bubbles compared to the original Star-0. The first trial to produce some LIG on top of it, by using the typical LIGP-settings (found in table 3.4), was successful and can be seen in figure 4.44. The material transferred into a black and conductive sheet.
Based on this preliminary success an investigation regarding how the content of flame-retardant Fe(NO_3)$_3$ affected LIG formation was made.Different Star-X composites at increasing amounts of the filler were prepared and tested, as summarized in table 4.14 and figure 4.45.

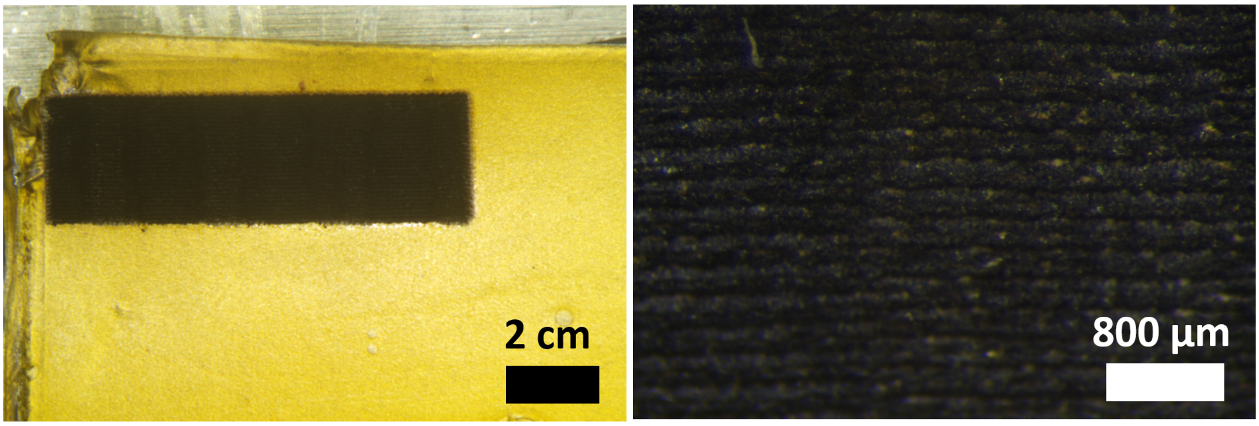

Figure 4.44.: Laser induced pyrolysis on Star-5

Table 4.14.: Resistance measurements of Star-X

Star-X	**Resistance** / kΩ
Star-1	non conductive
Star-2	non conductive
Star-3	~90
Star-4	~17
Star-5	~13

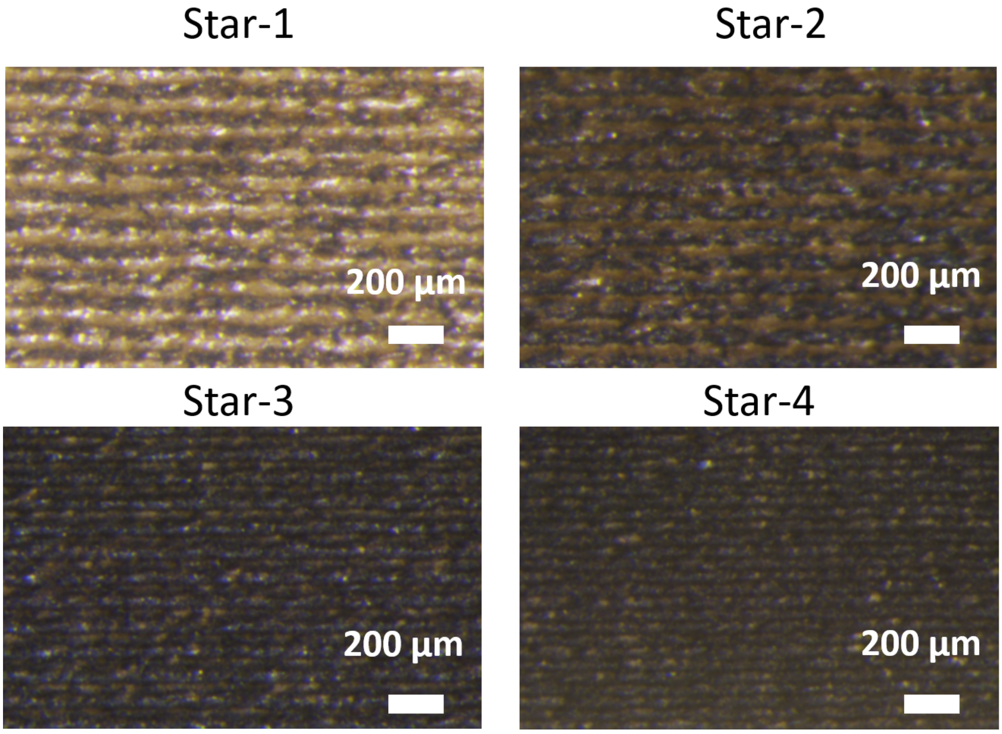

Figure 4.45.: Optical microscope images of Star-X

The resistance decreased with increasing concentration of $Fe(NO_3)_3$, which is consequential since the iron-salt adds flame-retardant properties to the bio-plastic. This effect is also recognizable in the images made with the optical microscope, seen in figure 4.45, where the decreasing resistance of the produced sheet was connected to the "blacking" of the material. The resistance compared to the one obtained with LIG produced on a PI sheet, was very high. LIG made with the same settings on PI typically had a sheet resistance around 100 Ω. Nevertheless, the production of a conductive material, starting with a self-designed biological precursor and without the usage of an inert atmosphere, one of the main goals for this project, was successfully accomplished. Further studies could enable to find optimised conditions and modification to the composition of the precursors or to the laser process for tailoring the desired conductive properties.

4.6.2. Keratin

Two different keratin-based materials, provided by ISOF (see section 3.1.2), were tested:
1) an electrospun keratin/PLA composite
2) a film of (keratin/PLA) produced by casting from a solution

Electrospun film

The electrospun keratin/PLA based film had a white colour, was made of a fibrous structure, see figure 4.46 , and had a thickness of around 90 µm. The sheet-thickness was measured with an optical microscope by observation of a cross section under the optical microscope, see figure 4.47.

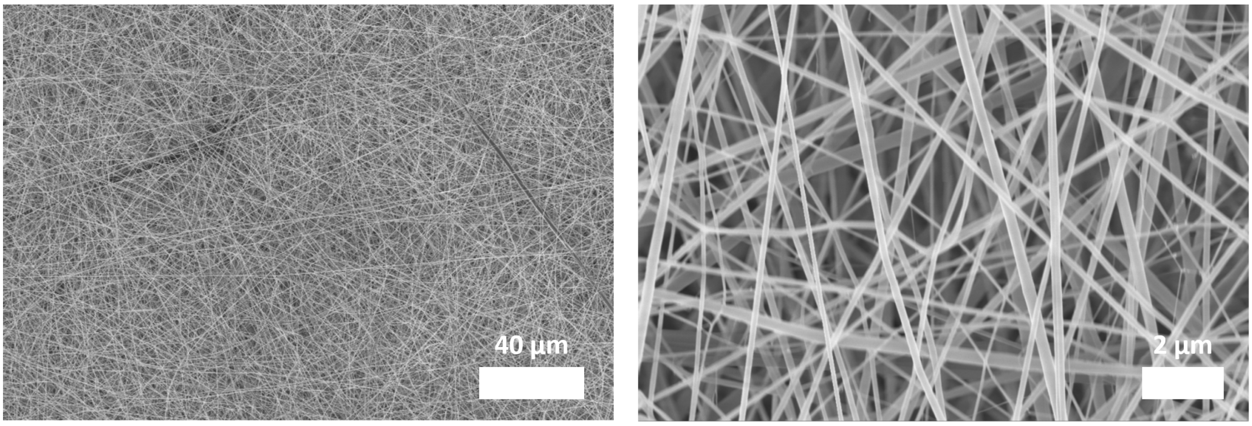

Figure 4.46.: SEM images of the electrospun keratin/PLA composite, provided by ISOF

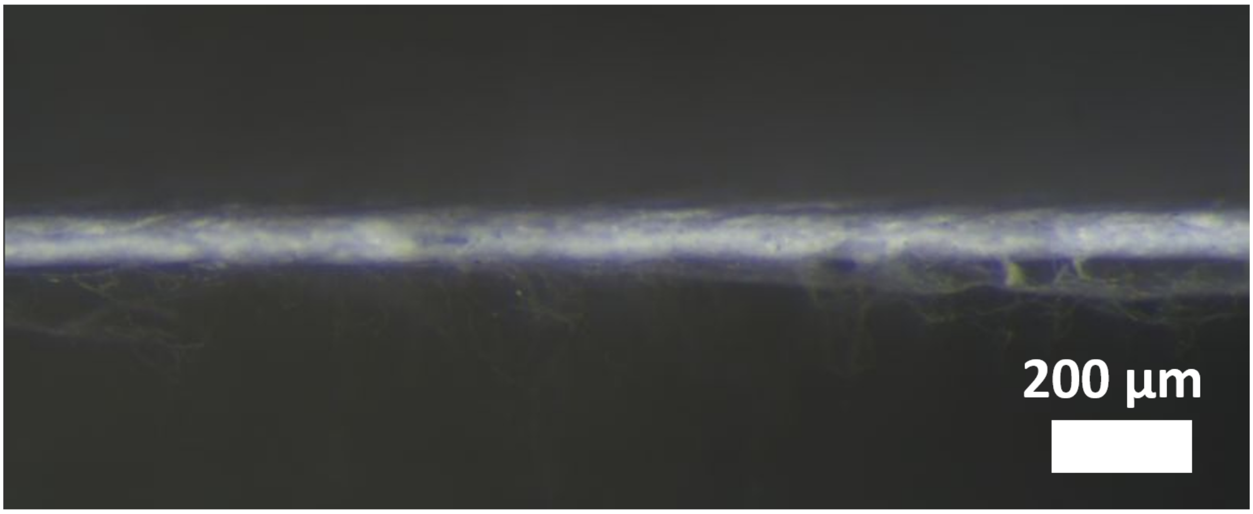

Figure 4.47.: Cross section of the electrospun keratin based film

Cast film

The cast film on the other hand was transparent. It was not possible to determine the thickness since it was too soft for a measurement with a profilometer and too thin to peel it off from the aluminium substrate. Even ISOF are not aware of any thickness determinations. The morphology of the cast film can be seen in figure 4.48.

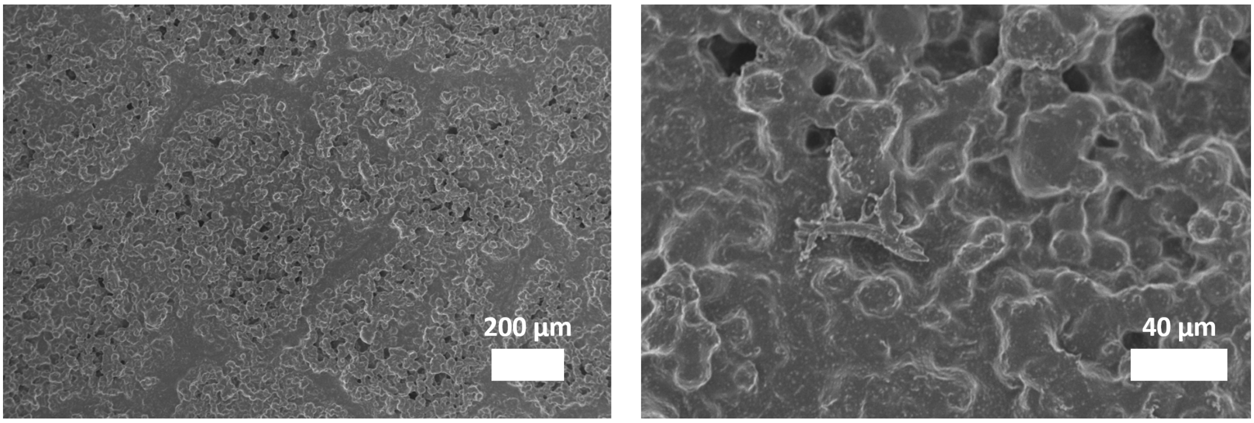

Figure 4.48.: acsuSEM images of the cast film (keratin/PLA composite), provided by ISOF

Formation of a conductive sheet

In figure 4.49 one can see the electrospun keratin/PLA samples on the left side and the cast film on the right side. For both material LIGP laser settings, once with $P\% = 5$ percent (top) and $P\% = 10$ percent (standard LIGP settings, bottom) were tested. After ineffectively trying to produce a conductive layer on top of it, 200 µL of an in water solved 5 wt% $Fe(NO_3)_3$ mixture was added by drop casting (seen as the orange or circular area in figure 4.49).

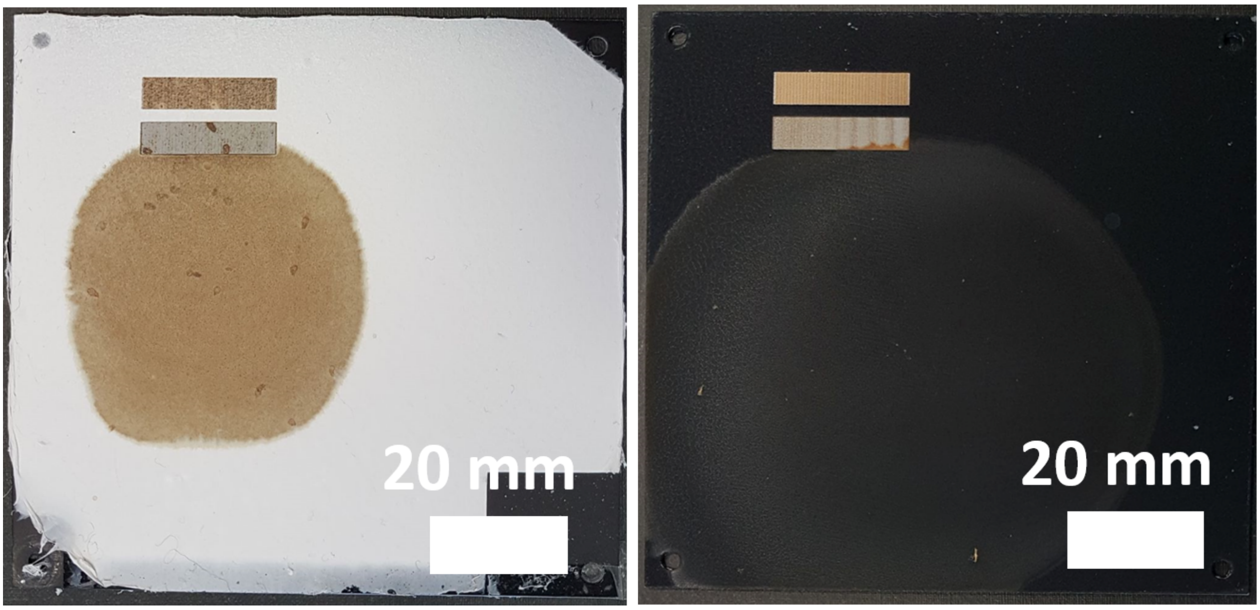

(a) electrospun film

(b) cast film

Figure 4.49.: Laser induced pyrolysis on keratin/PLA samples

After the deposition of the flame-retardant mixture another attempt was made to create a conductive material by laser induced pyrolysis, this time with LIGP, were $P\% = 5$ wt%, as processing parameters. The results can be seen in figure 4.50.

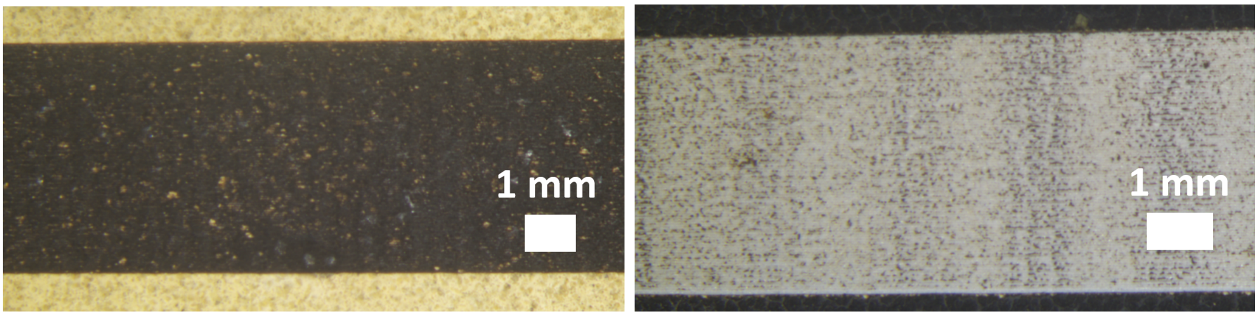

(a) electrospun film (b) cast film

Figure 4.50.: Laser induced pyrolysis on keratin/PLA samples with added $Fe(NO_3)_3$ layer by drop casting

Although the electrospun film turned black no conductivity was found, tested with a multimeter (*Fluke*). The same experiment was repeated on the cast film which turned out to be too thin since the white area was identified as the supporting aluminium plate. Hence, the received samples were not suitable for a LIG production.

Further possibilities for a trial to create a conductive layer on top of a keratin derived precursor, are to use films with a higher sheet thickness and to try a different flame-retardant or to use a higher concentration of it.

5. Conclusion

The results regarding the influence of process parameters on LIG morphology showed that a tuning of LIG was possible by changing the laser fluence. This can be controlled by changing the laser power P%, the speed setting S%, the defocus Z, the length of the sample l and the PPI setting. All influences were investigated and summarized in a Matlab script called Fluence Calculator to predict the LIG morphology on the basis of a chosen set of laser scribing parameters.
A precise investigation of processing speed distinguished the Fluence calculator from other research groups, where a linear increase of processing speed with the speed setting S% was assumed, independent from pattern size.
The investigation of the effect of defocusing permitted to highlight two important points which are deemed very relevant for future investigation of LIG materials. The theoretical laser scribing spot size differed from the observed spot, called impact area. In literature the impact area has been used for the fluence calculation,resulting an improper relation between impact area and laser fluence. Hence, it is recommended to use the theoretical spot size for a clear reflection between laser fluence and defocus.
The Fluence Calculator permitted to assess that for a PI precursor:

- no homogeneous formation of LIG is found for $\mathrm{H} < 20\,\mathrm{J \cdot cm^{-2}}$
- flat-LIG is obtained for $20 < \mathrm{H} < 45\,\mathrm{J \cdot cm^{-2}}$
- LIG-fibres are obtained for $45 < \mathrm{H} < 80\,\mathrm{J \cdot cm^{-2}}$
- the precursor gets destroyed for $\mathrm{H} > 80\,\mathrm{J \cdot cm^{-2}}$

In raster mode the *Image Density* (ID)-setting specifies the distance between scribed laser lines. Observing LIGF-IDX samples with an optical- a scanning electron-(SEM) and a transmission electron microscope (TEM) showed, that long fibres were always emerging from the sides of a scribed laser line. A qualitative assassment for the fibre lenghts is $\sim$ (100 - 200) µm and for the fibre diameter a few tens of nm. At low ID settings smaller LIG fibres growing in a radial way became visible. Further, it was found that on one side of a laser line slightly longer fibres were emerging in an alternating way, depending on the laser carriage driving direction, leading to the characteristic profile seen in the SEM images.
In general, an increase of ID led to an overlapping of those scribed lines, which can have an impact on the LIG-fibre growth since a multiple passing of the laser can destroy or affect the fibres. Nevertheless, an increasing number of scribed lines per cm reduces the resistance and therefore enhances the conductivity of the LIG on PI. LIG on MA on the other hand, showed a remarkable good conductive behaviour of LIGF-ID2 samples, compared to the other used ID setting, because in this case the scribed lines do not overlap, resulting in long and connected conductive fibres.

Besides the two already well known LIG morphologies (flat and fibres) a possible third one, called LIG-branching was found. It was observed with a SEM for samples prepared in vector mode and laser fluence values $\mathrm{H} \sim 80\,\mathrm{J \cdot cm^{-2}}$. Although the high laser fluence led to a destruction of the precursor in the middle of the scribed laser spot, the tips of fibres emerging on the sides had a branched morphology. Unfortunately, the origin of this behaviour remained unexplained but on the other hand it pointed out the possibility for interesting applications because of an assumed high specific surface area.

Individual correlative Raman-SEM spectra combined with a Raman mapping of LIGF samples showed, regardless of the ID setting, the typical Raman D-, G- and 2D-bands for graphite and a transition from an amorphous structure at the bottom to a more ordered and nanocrystalline regime closer to the tip of a fibre, starting at distance of around 30 µm from the precursor. This observed structural change was referred to a combination of temperature, laser spot overlapping, absorption coefficient and specific heat capacity changes along the fibre growth.

A design and production of a biological precursor, based on corn starch, able to transform into a conductive sheet, after a laser induced pyrolysis process in ambient environment, succeeded. An essential key was to use a flame-retardant component, as $Fe(NO_3)_3$, to prevent the biological material from degrading or burning induced by the laser. A similar formation of a conductive layer on top of a keratin based sample was not observed.

6. Improvements

In this section the occurred measurement problems and shortcomings were listed as well as unsolved subjects and how an improvement can be made in the future.

Neither a suitable detector for measuring the laser power nor the spot size was available. Hence one had to trust the manufacturer and his accessible specifications. Thus shortcomings on accuracy of the Fluence Calculator were traced back to this issue.

An origin for the appearance of a third LIG-morphology, namely LIG-branching, was not found. Further experiments are planned, including a reproduction of the experiment with the same settings but without an Ag-layer on top of it to verify its independent incidence.

The compositional research regarding the LIG-fibre morphology was not made for flat-LIG samples, where also a structural transition is expected to assure the theory of a temperature difference along the LIG-growth. Hence, a similar measurement was recommended.

Regarding the corn starch based bio-plastic lot of different experiments for detailed electrical and compositional properties should be made. Further different flame-retardant material could be tried to enhance the quality of the LIG. Nevertheless it seems to be a good starting point for the production of biological derived LIG in order to reduce the CO_2 footprint.

Bibliography

1. Ye, R., James, D. K. & Tour, J. M. Laser-Induced Graphene: From Discovery to Translation. *Advanced Materials* **31,** 1803621. eprint: `https://onlinelibrary.wiley.com/doi/pdf/10.1002/adma.201803621`. `https://onlinelibrary.wiley.com/doi/abs/10.1002/adma.201803621` (2019).
2. Dallinger, A., Keller, K., Fitzek, H. & Greco, F. Stretchable and Skin-Conformable Conductors Based on Polyurethane/Laser-Induced Graphene. *ACS Applied Materials & Interfaces* **0.** PMID: 32249561, null. eprint: `https://doi.org/10.1021/acsami.0c03148`. `https://doi.org/10.1021/acsami.0c03148` (0).
3. Dallinger, A. *Ultrathin, adhesive skin-contact electrodes* Master's thesis (TU Graz, 2018).
4. Ye, R., James, D. K. & Tour, J. M. Laser-Induced Graphene. *Accounts of Chemical Research* **51.** PMID: 29924584, 1609–1620. eprint: `https://doi.org/10.1021/acs.accounts.8b00084`. `https://doi.org/10.1021/acs.accounts.8b00084` (2018).
5. Katsnelson, M. I. *Graphene: Carbon in Two Dimensions* (Cambridge University Press, 2012).
6. Mamleyev, E. *et al.* Laser-induced hierarchical carbon patterns on polyimide substrates for flexible urea sensors. *npj Flexible Electronics* **3** (Dec. 2019).
7. Han, X. *et al.* Laser-Induced Graphene from Wood Impregnated with Metal Salts and Use in Electrocatalysis. *ACS Applied Nano Materials* **1** (Aug. 2018).
8. Dong, Y., Rismiller, S. C. & Lin, J. Molecular dynamic simulation of layered graphene clusters formation from polyimides under extreme conditions. *Carbon* **104,** 47–55. ISSN: 0008-6223. `http://www.sciencedirect.com/science/article/pii/S0008622316302391` (2016).
9. Duy, L. X. *et al.* Laser-induced graphene fibers. *Carbon* **126,** 472–479. ISSN: 0008-6223. `http://www.sciencedirect.com/science/article/pii/S0008622317310370` (2018).
10. Eichler, H. & Eichler, J. *Laser: Bauformen, Strahlführung, Anwendung* 3rd ed. ISBN: 3540639160 (The name of the publisher, 1998).
11. Yilbas, B. *Laser Heating Applications* (Jan. 2012).
12. Duy, L. X. *et al.* Laser-induced graphene fibers - supporting information. *Carbon* **126,** 472–479. ISSN: 0008-6223. `http://www.sciencedirect.com/science/article/pii/S0008622317310370` (2018).
13. Nielsen, S. *Food Analysis* 5th ed. ISBN: 978-3-319-45774-1 (Springer International Publishing, 2017).
14. Ferrari, A. Interpretation of Raman Spectra of Disordered and Amorphous Carbon. *Phys. Rev. B* **61** (May 2000).
15. Escribano, R., Sloan, J., Siddique, N., Sze, N. & Dudev, T. Raman spectroscopy of carbon-containing particles. *Vibrational Spectroscopy* **26,** 179–186 (Nov. 2001).

16. Matthews, M., Pimenta, M., Dresselhaus, G., Dresselhaus, M. & Endo, M. Origin of Dispersive Effects of the Raman D Band in Carbon Materials. *Physical Review B - PHYS REV B* **59** (Mar. 1999).

17. Lin, P. Laser-induced porous graphene films from commercial polymers. *Nature Communications* (2014).

18. Hrabovsky, J. *et al.* Surface structuring of Kapton polyimide with femtosecond and picosecond IR laser pulses. **7,** 113–121 (Oct. 2019).

19. Mendes, J. *et al.* Biodegradable polymer blends based on corn starch and thermoplastic chitosan processed by extrusion. *Carbohydrate Polymers* **137,** 452–458. ISSN: 0144-8617. `http://www.sciencedirect.com/science/article/pii/S0144861715010735` (2016).

20. *VLS Dektop User Guide VLS 2.30, VLS 3.50* `www.ulsinec.com` (2020).

21. *Universal Laser System Inc ULR30 Datasheet* `https://www.acalbfi.com/de/Photonik/Laser-und-Zubehor/Laser/p/CO2-Laser-10600nm-30W/0000001W45` (2020).

22. *Universal Laser System Availabe Lenses* `https://www.ulsinc.com/available-lenses` (2020).

23. *Air-Cooled Thermopile Sensors to 150W (RoHS)* `https://www.coherent.com/measurement-control/measurement/air-cooled-thermopile-sensors-to-150w-rohs` (2020).

24. *PDA36A-EC - March 14, 2018* `https://www.thorlabs.com/catalogpages/obsolete/2018/PDA36AEC.pdf` (2020).

25. Serebrennikova, A. *Masterthesis in Advanced Materials Science* Master's thesis (NAWI Graz, 2020).

26. Wall, M. Raman Spectroscopy Optimizes Graphene Characterization. *Advanced Materials and Processes* **170,** 35–38 (Apr. 2012).

27. Graf, D. *et al.* Spatially Resolved Raman Spectroscopy of Single- and Few-Layer Graphene. *Nano Letters* **7.** PMID: 17297984, 238–242. eprint: `https://doi.org/10.1021/nl061702a`. `https://doi.org/10.1021/nl061702a` (2007).

28. Rosenkranz, R. Failure localization with active and passive voltage contrast in FIB and SEM. *Journal of Materials Science-materials in Electronics - J MATER SCI-MATER ELECTRON* **22** (Nov. 2011).

29. Kouketsu, Y. *et al.* A new approach to develop the Raman carbonaceous material geothermometer for low-grade metamorphism using peak width. *Island Arc* **23** (Dec. 2013).

30. Chyan, Y. *et al.* Laser-Induced Graphene by Multiple Lasing: Toward Electronics on Cloth, Paper, and Food. *ACS Nano* **12.** PMID: 29436816, 2176–2183. eprint: `https://doi.org/10.1021/acsnano.7b08539`. `https://doi.org/10.1021/acsnano.7b08539` (2018).

A. Appendix

A.1. Processing speed measurements

A.1.1. Vector mode

Upper left corner of engraving table

In table A.1 the processing speed of one laser lane in vector mode, located in the upper left corner of the engraving table, can be seen. The measurement uncertainty for the processing time was $\Delta t_p = 0.15$ s.

Table A.1.: Processing time in vector mode - upper left corner

	t_p / s				
l / mm	**S% = 10**	**S% = 30**	**S% = 50**	**S% = 80**	**S% = 100**
10	0.22	0.25	0.26	0.30	0.29
30	1.16	0.72	0.73	0.64	0.71
50	2.06	0.78	0.77	0.80	0.80
100	3.90	1.34	0.84	0.59	0.32
200	7.70	2.73	1.63	0.97	0.67

Centre of engraving table

In table A.2 the processing speed of one laser line in vector mode, located in the centre of the engraving table, can be seen. The measurement uncertainty for the processing time was $\Delta t_p = 0.25$ s.

Table A.2.: Processing time in vector mode - centre

	t_p / s				
l / mm	**S% = 10**	**S% = 30**	**S% = 50**	**S% = 80**	**S% = 100**
10	0.53	0.45	0.46	0.40	0.40
30	1.12	0.73	0.68	0.60	0.53
50	2.06	0.93	0.72	0.67	0.61
100	4.01	1.38	0.8	0.61	0.41
200	7.99	2.70	1.42	1.13	0.86

Laser carriage movement

Due to the fact, that the processing time t_p was measured for only one laser line, the carriage movement corresponds to the pattern length l, found in table A.1 or table A.2.

A.1.2. Raster mode

Upper left corner of engraving table

In table A.3 the processing speed for a sample of 10 mm width in raster mode, located in the upper left corner of the engraving table, can be seen. The measurement uncertainty for the processing time was $\Delta t_p = 1$ s.

Table A.3.: Processing speed in raster mode - upper left corner

	t_p / s				
l / mm	**S% = 10**	**S% = 30**	**S% = 50**	**S% = 80**	**S% = 100**
10	49	27	24	28	31
30	94	43	34	35	37
50	111	48	37	36	38
100	189	74	52	46	46
200	358	131	87	71	68

Centre of engraving table

In table A.4 the processing speed for a sample of 10 mm width in raster mode, located in the centre of the engraving table, can be seen. The measurement uncertainty for the processing time was $\Delta t_p = 1$ s.

Table A.4.: Processing speed in raster mode - centre

	t_p / s				
l / mm	**S% = 10**	**S% = 30**	**S% = 50**	**S% = 80**	**S% = 100**
10	63	33	29	34	39
30	94	43	35	38	42
50	125	54	41	42	45
100	203	79	57	52	53
200	358	131	88	71	68

Laser carriage movement

In raster mode the laser carriage movement x did not correspond to the pattern length l. Therefore one can find the measured x in table A.5 with a measurement uncertainty $\Delta x = 2$ mm.

Table A.5.: Laser carriage movement x

	x / mm				
l / mm	**S% = 10**	**S% = 30**	**S% = 50**	**S% = 80**	**S% = 100**
10	32	34	42	71	98
30	51	54	61	92	116
50	71	74	81	111	137
100	121	124	131	161	177
200	221	223	231	260	287

A.2. Calculation of processing speed

A.2.1. Middle of engraving table

Vector mode

A quadratic fit was used for fitting the results for the processing speed measurements:

$$v(S\%) \; = \; p_1 \cdot S\%^2 \; + \; p_2 \cdot S\% \; + \; p_3$$

In table A.6 one can find the related fit parameter p_1, p_2, and p_3.

Table A.6.: Fit parameters for processing speed in vector mode

l/mm	**$\mathbf{p}_1 \cdot \mathbf{10}^{-3}$**	**$\mathbf{p}_2$**	**$\mathbf{p}_3$**
10	23	-0.5	64
30	15	0.2	47
50	4	1.6	22
100	29	1.0	25
200	7	2.5	4

Raster mode

A quadratic fit was used for fitting the results for the processing speed measurements:

$$v(S\%) \; = \; p_1 \cdot S\%^2 \; + \; p_2 \cdot S\% \; + \; p_3$$

In table A.7 one can find the related fit parameter p_1, p_2, and p_3.

Table A.7.: Fit parameters for processing speed in raster mode

l/mm	**$\mathbf{p}_1 \cdot \mathbf{10}^{-3}$**	**$\mathbf{p}_2$**	**$\mathbf{p}_3$**
10	-6	5	54
30	-23	7	40
50	-30	9	34
100	-50	12	7
200	-40	12	5

A.3. Spot diameter measurements

Following fit was used for the measured spot diameter seen in figure 4.10 (b):

$$d_{SEM}(Z) \;=\; p_1 \;\cdot\; Z^2 \;+\; p_2 \;\cdot\; Z \;+\; p_3$$

p_1 = -51.2 ± 4.5; p_2 = -2.4 ± 2.5; p_2 = 74 ± 2

A.3.1. Fluence calculator

In table A.8 the theoretical laser spot size s_{theo}, calculated with equation (2.2), equation (2.3) and equation (2.4), as well as the observed laser impact area s_{SEM}, calculated by using the measured diameters found in table 4.6 and equation (2.4), can be found. Further the related laser fluence value calculated by the fluence calculator with following settings:
P% = 0.2 %; S% = 8 %; PPI = 40; l = 4 mm; mode: vetor mode
are listed.

Table A.8.: Fluence and spot size

Z / mm	$\mathbf{s}_{theo}$ / µm^2	$\Delta\mathbf{s}_{theo}$ / µm^2	$\mathbf{s}_{SEM}$ / µm^2	$\Delta\mathbf{s}_{SEM}$ / µm^2	**H** / $\frac{\text{J}}{\text{cm}^2}$	Δ**H** / $\frac{\text{J}}{\text{cm}^2}$
-1.1	4200	380	700	300	12	1
-1	3500	350	2400	300	14	2
-0.9	2800	310	4900	200	18	2
-0.8	2200	280	5700	300	22	2
-0.7	1700	240	7700	600	29	3
-0.6	1300	210	10100	500	40	4
-0.5	1300	210	9300	200	58	5
-0.4	900	170	10000	700	70	7
-0.3	700	80	12500	500	80	9
-0.2	600	50	15000	900	90	10
-0.1	600	30	18500	2000	97	11
0	500	10	16400	500	99	12
0.1	500	0	15600	1900	97	11
0.2	500	10	18500	3300	90	10
0.3	600	30	18300	1300	80	9
0.4	600	50	16500	800	70	7
0.5	700	70	14600	1400	58	5
0.6	900	170	10700	400	40	4
0.7	1300	210	9100	1200	29	3
0.8	1700	240	6300	200	22	2
0.9	2200	280	5000	300	18	2

The relation between laser fluence H and diameter of the impact area can be seen in figure A.1.

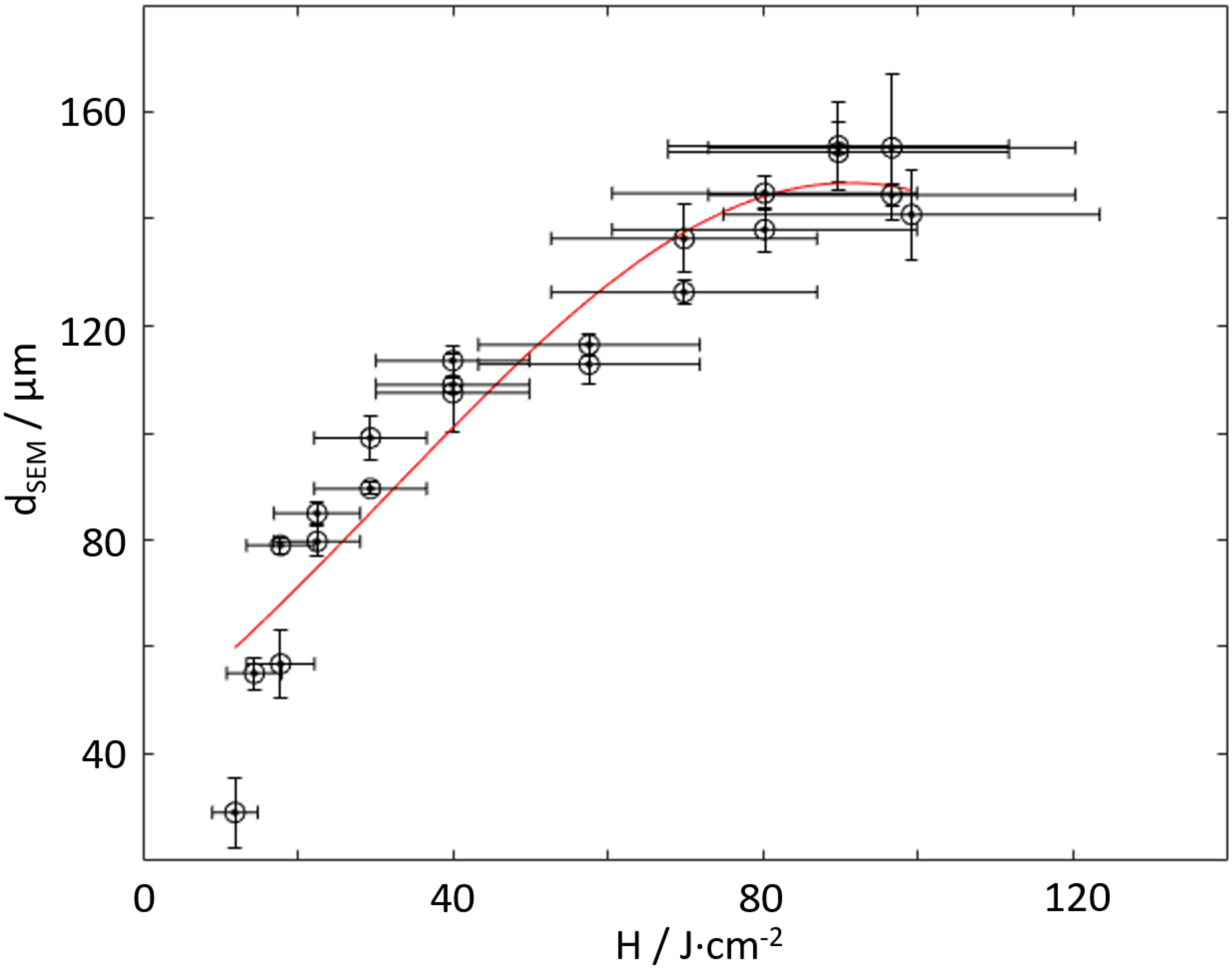

Figure A.1.: Gaussian fit for the relation between laser fluence and impact area

The used fit and parameters are:

$$d(H) = a \cdot exp\left(-\frac{(H - b)}{c^2}\right)$$

a = 147 ± 9; b = 90 ± 20; c = 80 ± 20;

A.4. Fluence mapping

Results for the calculated fluence values according to the LIG-morphology mapping seen in figure 4.13.

Table A.9.: Calculated fluence values for different P% and S% configurations

		H / $\mathrm{J}\cdot\mathrm{cm}^{-2}$									
P%	**S%**	**10**	**20**	**30**	**40**	**50**	**60**	**70**	**80**	**90**	**100**
38		100 ± 10	68 ± 7	52 ± 5	42 ± 4	36 ± 4	31 ± 3	28 ± 3	25 ± 3	23 ± 3	21 ± 2
36		95 ± 10	65 ± 7	50 ± 5	40 ± 4	34 ± 3	30 ± 3	26 ± 3	24 ± 2	22 ± 2	20 ± 2
34		90 ± 9	61 ± 6	47 ± 5	38 ± 4	32 ± 3	28 ± 3	25 ± 3	22 ± 2	20 ± 2	19 ± 2
32		84 ± 9	58 ± 6	44 ± 4	36 ± 4	30 ± 3	26 ± 3	23 ± 3	21 ± 2	19 ± 2	18 ± 2
30		80 ± 8	54 ± 6	41 ± 4	34 ± 3	28 ± 3	25 ± 3	22 ± 2	20 ± 2	18 ± 2	17 ± 2
28		74 ± 8	50 ± 5	39 ± 4	31 ± 3	26 ± 3	23 ± 2	20 ± 2	18 ± 2	17 ± 2	15 ± 2
26		69 ± 7	47 ± 5	36 ± 4	29 ± 3	25 ± 3	21 ± 2	19 ± 2			
24		63 ± 7	43 ± 4	33 ± 3	27 ± 3	23 ± 2	20 ± 2	17 ± 2			
22		58 ± 6	40 ± 4	30 ± 3	25 ± 3	21 ± 2	18 ± 2	16 ± 2			
20		53 ± 5	36 ± 4	28 ± 3	22 ± 2	19 ± 2	16 ± 2	15 ± 1			

A.5. Raman spectra

A.5.1. ID2 sample

Raman spectra made of a single fibre,from a LIGF-ID2 sample, along the trend in figure 4.31 can be seen in figure A.2.

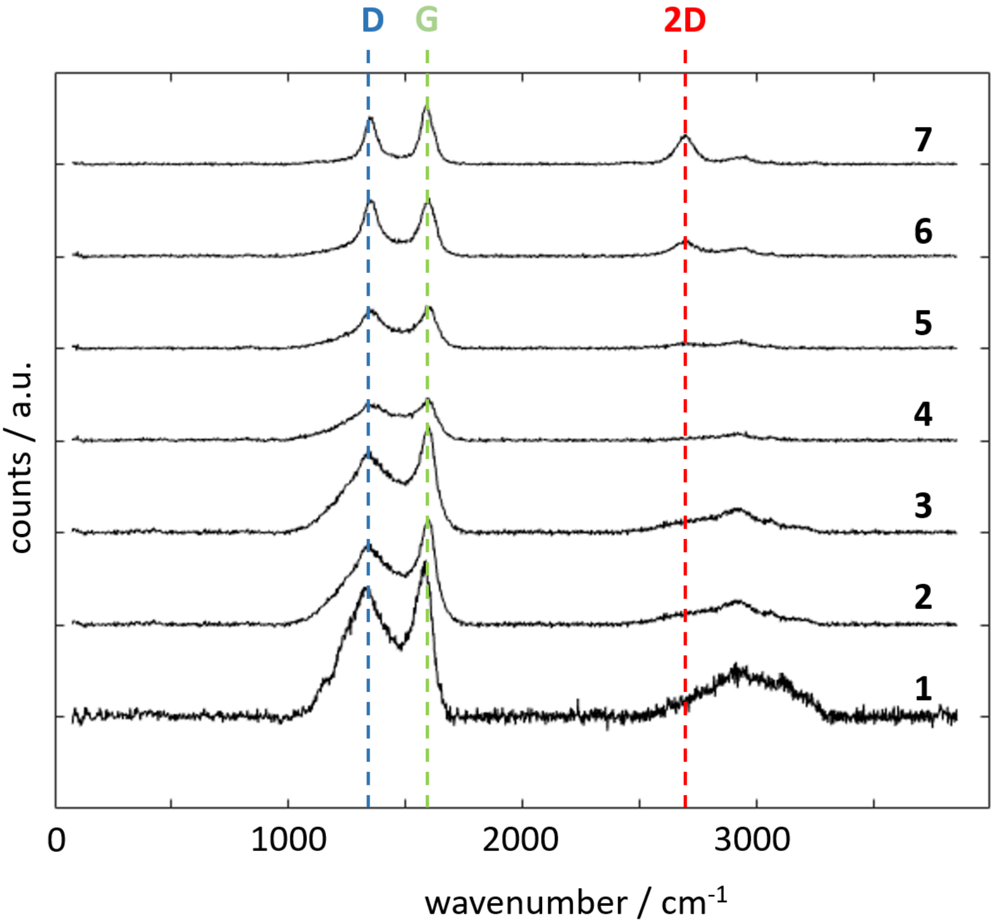

Figure A.2.: Raman spectra of a LIGF-ID2 sample

In table A.10 one can see the results for a correlative Raman-SEM technique performed on the LIGF-ID2 sample. The corresponding plots can be found in figure A.3. The measurement points refer to the one seen in figure 4.31 (a).

Table A.10.: Results for a correlative Raman-SEM-measurement performed on a LIGF-ID2 sample

	ID2					
	G$_{pos}$ / cm^{-1}	**I$_{2D}$/I$_G$**	**I$_D$/I$_G$**	**L$_a$ / nm**	**fwhm$_G$ / cm^{-1}**	**fwhm$_D$ / cm^{-1}**
1	1577	0.0	0.93	5.3	95	263
2	1594	0.0	0.80	4.9	87	291
3	1596	0.0	1.09	5.8	91	333
4	1593	0.0	1.12	5.8	103	295
5	1595	0.0	1.00	5.5	95	177
6	1594	0.3	1.06	4.7	81	86
7	1591	0.5	0.82	6.1	64	64

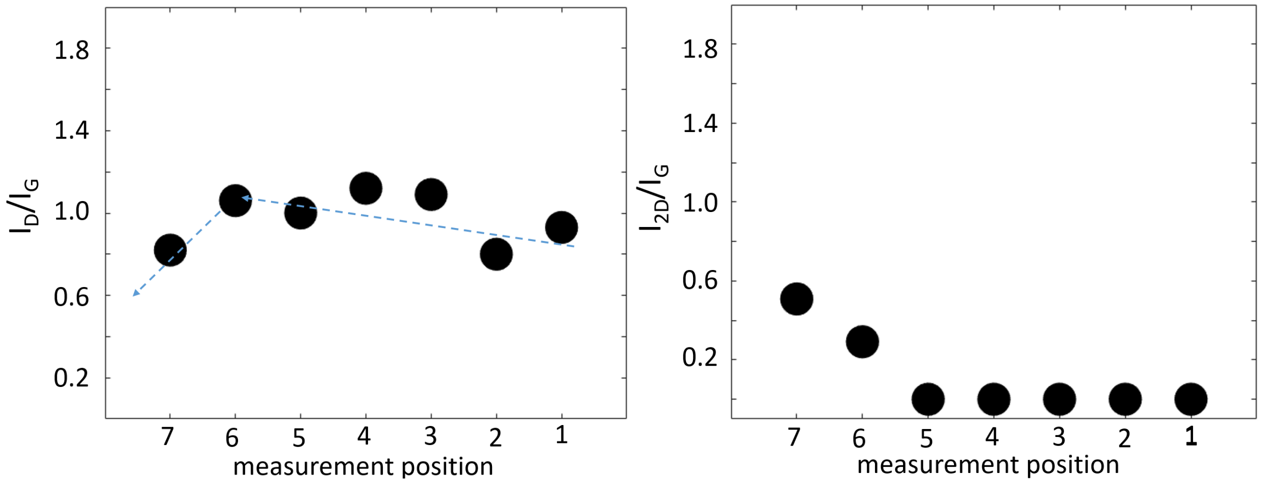

(a) I_D/I_G-ratio (b) I_{2D}/I_G-ratio

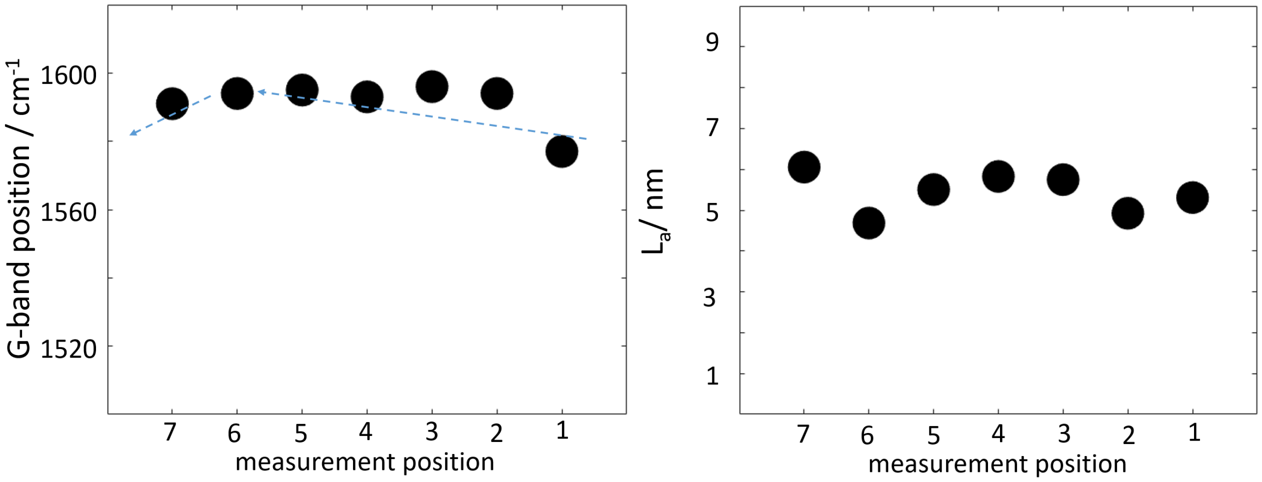

(c) G-band position (d) grain size

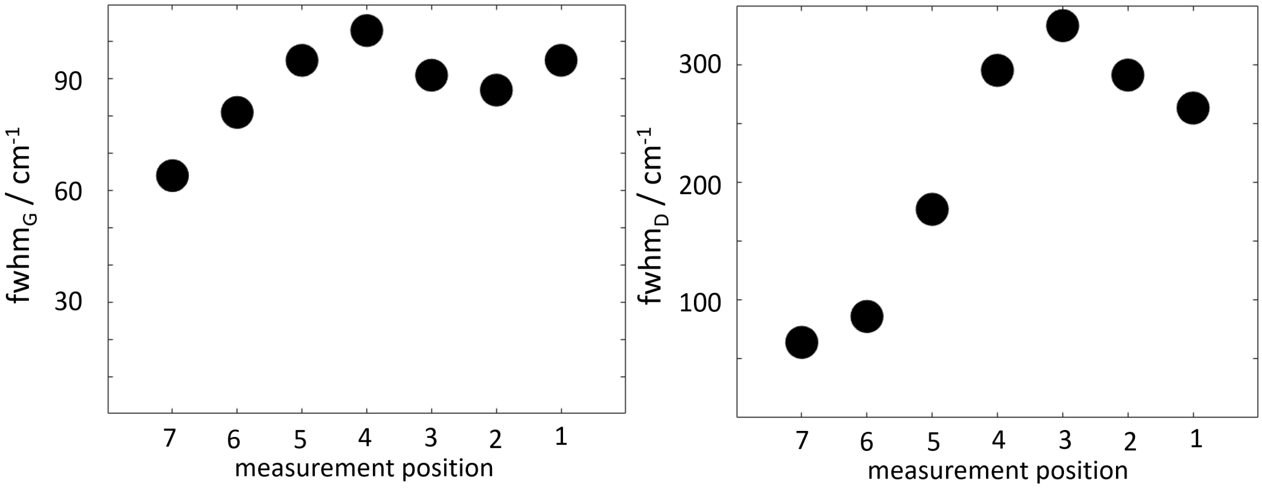

(e) G-band width (f) D-band width

Figure A.3.: Results of intensity ratios, G-band position, grain size and band widths for a LIGF-ID2 sample

A.5.2. Raman mapping

In figure figure A.4 and figure A.5 the results for fwhm$_G$ and fwhm$_D$ obtained by Raman mapping of a LIGF-ID5 sample can be seen.

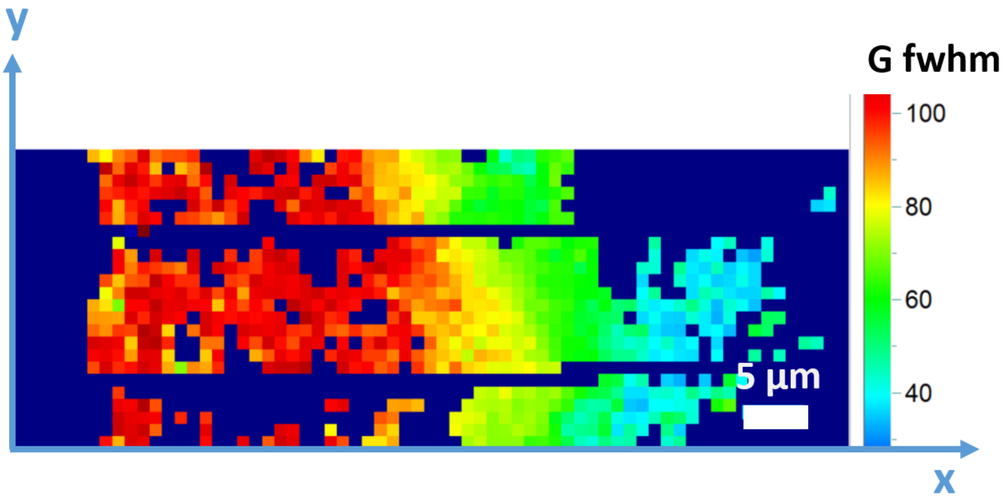

Figure A.4.: Raman mapping of G-band width (LIGF-ID5 sample)

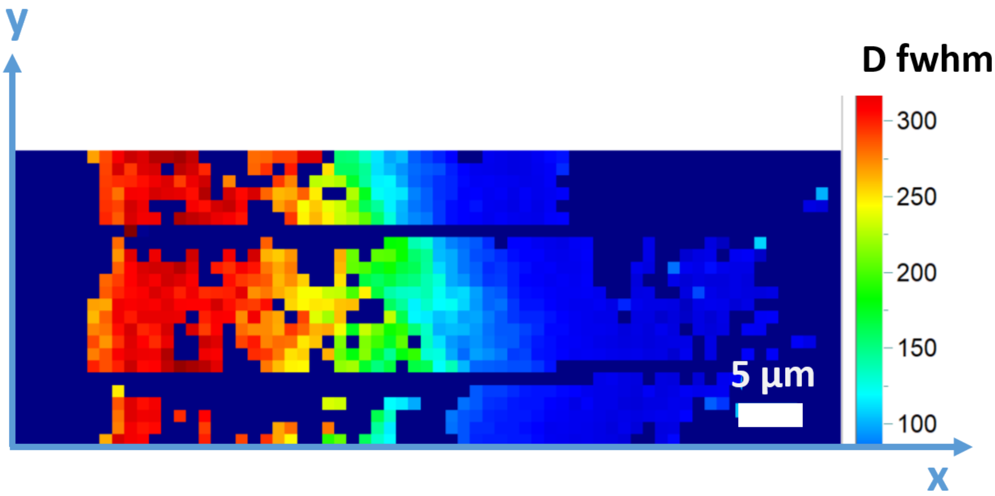

Figure A.5.: Raman mapping of D-band width (LIGF-ID5 sample)